Supermassive Black Holes and Relativistic Jets

Jets, acrecimiento y campos magnéticos en el entorno de agujeros negros supermasivos en los centros de galaxias

Juan Escudero Pedrosa
Tesis Doctoral
Programa de Doctorado en Física y Matemáticas
Universidad de Granada

Supermassive Black Holes and Relativistic Jets

Jets, acrecimiento y campos magnéticos en el entorno de agujeros negros supermasivos en los centros de galaxias

Juan Escudero Pedrosa

Year 2024

Submitted for the degree of Doctor

Under the supervision of
Dr. Juan Iván Agudo Rodríguez

Tesis Doctoral
Programa de Doctorado en Física y Matemáticas
Universidad de Granada

UNIVERSIDAD DE GRANADA

INSTITUTO DE ASTROFÍSICA DE ANDALUCÍA

EXCELENCIA SEVERO OCHOA

Contents

List of Figures

List of Tables

List of Acronyms

ADU Analog-to-Digital Unit i, 23

AGN Active galactic nucleus i, xi, 2, 3, 5, 6, 10, 15, 60, 71

ALP Axion-like particle i, 19

API Application public interface i, 75, 79, 80

a.s.l. Above sea lavel i, 28

BC Bulk-Compton i, 51, 53, 54

BH Black hole i, 2, 16, 37, 50, 51, 60, 67, 69

BLR Broad line region i, 51, 67, 69

BLRG Broad Line Radio Galaxy i, 3, 5

CAFOS Calar Alto Faint Object Spectrograph i, 23, 74, 81

CAHA Centro Astronómico Hispano-Alemán i, 23

CCD Charge-coupled device i, 23, 26, 80, 81

ΛCDM Lambda cold dark matter i, 37, 61

CI/CD Continuous Integration and Continuous Deployment i, 82

CMB Cosmic microwave background i, 15

COSI Compton Spectrometer and Imager i, 85

CTAO Cherenkov Telescope Array Observatory i, 28, 31, 85

DB database i, 75–77

DCF Discrete Correlation Function i, 31, 41, 44, 46, 52, 53

DSA Diffusive shock acceleration i, 50, 51

DT Disk torus i, 51, 60, 67, 69

EAS Extensive air shower i, 28

EBL Extragalactic background light i, 14

EC External Compton i, xi, 13, 37, 50, 53, 54, 67, 69

EM Electromagnetic i, 28

EVPA Electric vector position angle i, 38

***Fermi*-LAT** *Fermi* - Large Area Telescope i, 28, 37, 61

FoV Field of view i, 28

FSRQ Flat-spectrum radio quasar i, 4

FWHM Full width half maximum i, 44

GR General Relativity i, 16

GRB Gamma-ray burst i, 27

GRMHD General-relativisitic magnetohydrodynamics i, 18

GZK limit Greisen–Zatsepin–Kuzmin limit i, 15

HAWC High Altitude Water Cherenkov i, 28

HE High energy i, 37

HESS High Energy Stereoscopic System i, 28

HSP High synchtoron peaked i, 37

IAA-CSIC Instituto de Astrofísica de Andalucía i

IAC Instituto de Astrofísica de Canarias i, 31

IACT Imaging Atmospheric Cherenkov Telescope i, 14, 28

IC Inverse Compton i, 50

IGMF Intergalactic magnetic field i, 19

IR Infrared i, 38

IRAM Institut de Radioastronomie Millimetrique i, 23

ISM Ionized interstellar medium i, 21

IXPE Imaging X-ray Polarimetry Explorer i, 85

LIV Lorentz invariance violation i, 19

LST Large-Sized Telescope i, 29, 31

MAGIC Major Atmospheric Gamma Imaging Cherenkov Telescopes i, 28

MJD Modified Julian day i, 49, 52, 53, 67, 69

ML Machine learning i, 28

MLE Maximum-likelihood estimation i, 34

MWL Multi-wavelength i, 37, 60, 61, 67, 70, 84

NLRG Narrow Line Radio Galaxy i, 3, 5

ORM Object-relational mapping i, 31, 74–76

OSN Observatorio de Sierra Nevada i, 23

PLC Power law with a cutoff i, 67

POLAMI Polarimetric Monitoring of AGN at Millimetre Wavelengths i, 23

PSD Power Spectral Density i, 33, 34, 66, 69

QSO Quasi-stellar object i, 4

QSR Quasi-stellar radio source i, 4

RF Random Forest i, 28

RXTE Rossi X-ray Timing Explorer i, 27

SDE Stochastic differential equation i, 34

SDSS Sloan Digital Sky Survey i, 79

SED Spectral energy distribution i, xi, 36, 37, 43, 49, 54, 84

SM Standard Model i, 18

SMBH Supermassive black hole i, xi, 16, 36

SPA Single-page application i, 79, 80

SQL Structured Query Language i, 74, 76

SR Special Relativity i, 4

SSC Synchrotron self-Compton i, xi, 13, 37, 50, 54, 67, 69

***Swift*-UVOT** *Swift* - Ultraviolet Optical Telescope i, 37, 61, 67

***Swift*-XRT** *Swift* - X-ray Telescope i, 27, 37, 50, 61, 67

UHECR Ultra-high energy cosmic ray i, 15

ULIRG Ultraluminous infrared galaxy i, 4

UV Ultraviolet i, 28, 38, 49

VERITAS Very Energetic Radiation Imaging Telescope Array System i, 28

VHE Very high energy i, 14, 29, 84

VLBA Very Long Baseline Array i, 23, 37, 38, 49, 61–65, 69, 70

VLBI Very-long-baseline interferometry i, 23, 36–38, 40, 41, 43, 44, 47, 49, 51, 54, 60, 61, 63, 67, 69, 70

Abstract

Blazars, a type of active galactic nuclei (AGNs), are among the most energetic objects in the universe. They are generally accepted to consist of a super massive black hole (SMBH) at the center of a galaxy that is surrounded by an accretion disk and usually a dusty torus, with symmetrical jets of matter emanating from the vicinity of the black hole and the accretion disk. Particles in the jet are accelerated and collimated to speeds close to the speed of light. These relativistic jets many times extend far beyond the size of their host galaxy, and can have dramatic effects in their life and evolution. Moreover, emission from blazars typically outshines the emission of their host galaxy. The exact mechanisms of this emission are not well understood, and questions remain about the processes of acceleration and collimation of particles in the jet as well as about the particle composition of the jet and the location and cause of the observed variability and γ-ray emission. While the first, low energy bump of blazar spectral energy distributions (SEDs) is widely accepted to be explained by synchrotron radiation, the origin and exact nature of the second, high energy bump is still uncertain. In leptonic scenarios, this bump is accepted to be the result of inverse Compton scattering off relativistic electrons, but there is no agreement on the origin of the scattered photon field. Two mean competing scenarios are proposed: photons originating in the same region, in which case the process is termed synchrotron self-Compton (SSC), or photons (mostly of thermal origin) external to the emitting region itself (external Compton, EC), with distinction made according to the possible origin of these photons (the cosmic microwave background, the accretion disk, etc). In this thesis we introduce the blazar phenomenon and present some of the work of research that has been conducted to answer these questions.

In Chapter 1 we succinctly outline the observational history of blazars and introduce some of the fundamental physics and concepts behind them. Chapter 2 introduces the observational techniques that are required for the multi-wavelength study of these objects, and gives an account of the significant observational effort that has been performed; among others: photo-polarimetric mm-wavelength observations at the IRAM 30m telescope within the POLAMI program, observations and

data reduction of optical photo-polarimetric data at the Sierra Nevada and Calar Alto observatories, and on-site data-taking and analysis of very-high energy γ-ray observations with the MAGIC and LST-1 telescopes at the Roque de los Muchachos Observatory, in La Palma.

Chapters 3, 4 and 5 present novel research conducted in the framework of this thesis, and correspond to three articles accepted in high-impact peer-reviewed journals. Chapters 3 and 4 are detailed multi-wavelength studies of the blazar source AO 0235+164, a source that displays particularly interesting characteristics such as repeating flaring activity, strongly correlated multi-wavelength emission, unusual behavior in the X-ray spectrum, and variations in the angle of propagation of identified features in high-resolution VLBI images, among others. Multiple approaches are attempted to tackle the problem of explaining the behavior of this source, such as cross-correlation analysis, geometric and kinematic analysis of VLBI features, multi-epoch modeling of the spectral energy distribution, and other analyses, in a compatible and sensible way. Chapter 5 presents IOP4, a pipeline developed as part of this thesis to address the challenges of optical photo-polarimetric monitoring programs of these sources, which are an essential tool for any comprehensive study of blazars. The paper describes the basic design and implementation of the pipeline, as well as some of its novel features.

Finally, we summarize the work done and highlight our conclusions in Chapter 6.

Resumen

Los blázares, un subtipo entre los núcleos activos de galaxias (AGNs), se encuentran entre los objetos más energéticos del universo. Se acepta generalmente que consisten en un agujero negro supermasivo (SMBH) en el centro de una galaxia rodeado por un disco de acrecimiento y, usualmente, un toro de polvo, con chorros simétricos de materia que emanan de las proximidades del agujero negro y el disco de acrecimiento.

Las partículas en el chorro son aceleradas y colimadas a velocidades cercanas a la de la luz. Estos chorros relativistas muchas veces se extienden mucho más allá del tamaño de su galaxia anfitriona y pueden tener efectos dramáticos en su vida y evolución. Además, la emisión de los blázares típicamente supera a la emisión de su galaxia anfitriona. Los mecanismos exactos de esta emisión no se comprenden bien, y quedan preguntas sobre los procesos de aceleración y colimación de partículas en el chorro, así como sobre la composición de partículas del chorro y la ubicación y causa de la variabilidad observada y la emisión de rayos γ. Mientras que se acepta ampliamente que el primer pico de baja energía de las distribuciones espectrales de energía (SEDs) de los blázares se debe a radiación sincrotrón, el origen y la naturaleza exacta del segundo pico de alta energía es aún incierto. En los escenarios leptónicos, se acepta que este pico es el resultado de una dispersión Compton inversa por electrones relativistas, pero no hay acuerdo sobre el origen del campo de fotones dispersados. Se proponen dos escenarios principales competidores: fotones que se originan en la misma región, en cuyo caso el proceso se denomina sincrotrón auto-Compton (SSC), o fotones (mayormente de origen térmico) externos a la propia región emisora (Compton externo), con distinción según el posible origen de estos fotones (el fondo cósmico de microondas, el disco de acrecimiento, etc).

En esta tesis introducimos el fenómeno de los blázares y presentamos algunos de los trabajos de investigación que se han realizado para responder a estas preguntas.

En el Capítulo 1 revisamos sucintamente la historia observacional de los blázares e introducimos algunos de los conceptos y física fundamental tras ellos. El Capítulo 2 presenta las técnicas observacionales requeridas para el estudio multi-longitud de onda de estos objetos y da cuenta del significativo esfuerzo observacional realizado;

entre otros: observaciones foto-polarimétricas en longitudes de onda milimétricas en el telescopio IRAM de 30m dentro del programa POLAMI, observaciones y reducción de datos foto-polarimétricos en óptico en los observatorios de Sierra Nevada y Calar Alto, y toma y análisis de datos in situ de observaciones de rayos γ de muy alta energía con los telescopios MAGIC y LST-1 en el Observatorio del Roque de los Muchachos, en La Palma.

Los Capítulos 3, 4 y 5 presentan investigaciones novedosas realizadas en el marco de esta tesis, y corresponden a tres artículos aceptados en revistas de alto impacto revisadas por pares.

Los Capítulos 3 y 4 son estudios detallados en múltiples longitudes de onda de la fuente blázar AO 0235+164, una fuente que muestra características particularmente interesantes como actividad de erupciones repetidas, emisión en múltiples longitudes de onda fuertemente correlacionada, comportamiento inusual en el espectro de rayos X y variaciones en el ángulo de propagación de componentes identificadas en imágenes VLBI de alta resolución, entre otras. Se combinan múltiples enfoques para abordar el problema de explicar el comportamiento de esta fuente, como análisis de correlaciones cruzadas, análisis geométrico y cinemático de componentes en VLBI, modelado de la distribución de energía espectral en múltiples épocas y otros análisis, de manera compatible y coherente.

El Capítulo 5 presenta IOP4, una pipeline desarrollada como parte de esta tesis para abordar los desafíos de los programas de monitoreo foto-polarimétrico en óptico de estas fuentes, que son una herramienta esencial para cualquier estudio integral sobre los blázares. El artículo describe el diseño básico y la implementación de la pipeline, así como algunas de sus características novedosas.

Finalmente, resumimos el trabajo realizado y destacamos nuestras conclusiones en el Capítulo 6.

Chapter 1

Introduction

The Guide is definitive. Reality is often inaccurate.
— Douglas Adams, *The Hitchhiker's Guide to the Galaxy.*

1.1 Historical Background

Observational history of quasars commences with the first reports of enhanced nuclear activity in some galaxies by Carl K. Seyfert in 1943, twenty three years after the Great Debate that settled the nature of galaxies as "island universes". Heber Curtis himself, who would go on to prove the ideas of Inmanuel Kant correct, had already noted down the first observation of an astrophysical jet, that of M87. It remained a curiosity, however, and it was not until the explosion of radio astronomy in the aftermath of World War II that the strong radio emission from some galaxies was discovered. In the 60s, Thomas Matthews and Allan Sandage found the optical counterpart of the radio source 3C 48 to be a star-like object, whose emission lines could not be identified; and the term quasar appeared for the first time to describe these quasi-stellar radio sources.

The list of quasars, at the moment still called radio stars, grew rapidly. A major breakthrough was the realization that the unfamiliar emission lines of these objects were actually the redshifted and broadened Balmer lines of hydrogen. The high redshift automatically placed these as the most-distant objects in the known Universe.

The nature of the emission was however, still a mystery. Alfvén and Herlofson suggested in 1950 that the radio emission of Cygnus A, one of the first radio sources to be discovered, was Synchrotron radiation, an idea that was extended to the optical

emission of the Crab Nebula by Shklovsky, and finally accepted with the discovery of optical linear polarization from it and from the jet of M87.

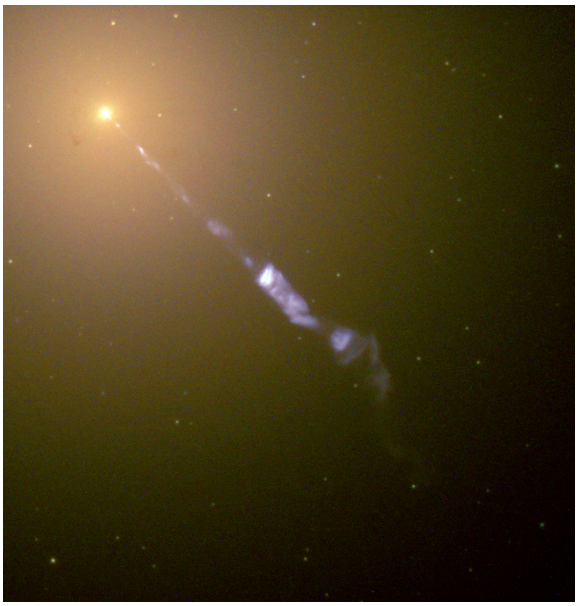

Figure 1.1: Jet emerging from the core of M87, extending 20 arc seconds. "A curious straight ray lies in a gap in the nebulosity in p.a. 20 deg, apparently connected with the nucleus by a thin line of matter", wrote Curtis ([1]). Image: NASA and the Hubble Heritage Team (STScI/AURA).

A curiosity at first, jets became more ubiquitous with the improvements in interferometry; and their presence was extended even to other types of objects such as microquasars (radio emitting X-ray binaries). For AGNs, it was observed that most bright jets were on a single side of the nucleus, in contrast to the radio sources whose jets were dimmer, but visible on both sides, and Doppler boosting was invoked to explain the asymmetry. Relativistic effects were further necessary once the resolution and sensitivity of VLBI observations allowed to track individual jet features, which displayed apparent speeds several times larger than the speed of light.

The amount of power transmitted by relativistic jets posed the important question about the source of such amounts of energy, and it was understood that a supermassive black hole was needed to provide efficient ways of transforming potential and rotational energy. This was in agreement with the fact that radio-galaxies seemed to favor massive elliptical.

With the development of X-ray astronomy, models of Synchrotron emission were severely constrained. The presence of a high-frequency cutoff in the optical for many sources meant that it was hard to explain the whole of emission as synchrotron radiation. In addition, it was difficult to explain the propagation (to large distances) of relativistic electrons, if they were energetic enough to explain the X-ray measurements. Only in few cases Synchrotron self-Compton (SSC) emission could explain the X-ray spectrum from some of the radio hostpots in jets. Inverse-Compton (IC) of thermal electrons was invoked to provide additional sources of high energy photons.

The advent of gamma-ray astronomy enabled the discovery of high-energy ($>$ 100 MeV) γ-ray emission from blazars during the first satellite missions. Ground-based experiments also discovered very-high-energy ($>$ 1 TeV) γ-ray emission from some blazars, sometimes with variability in timescales of only a few minutes. It was seen that blazars typically emitted more energy in the gamma-ray band than at all other wavelengths combined. In addition, the fact that TeV γ-rays were not absorbed in pair-production further strengthened the hypothesis of highly boosted emission by relativistic effects.

The convoluted history of observation and understanding of AGNs has led to a complex classification, summarized in Table 1.1 and illustrated in Fig. 1.2. Nowadays it is understood that all these objects can be related to an unified model of AGNs. In this model, the differences between these objects correspond to particular observational circumstances (e.g. the view angle), or a particular point in their evolution or lifetime (e.g. accretion).

Galaxies with bright nuclei and broad emission lines are now called Seyfert galaxies. They are sub-classified in Seyfert I and Seyfert II galaxies, primarily dependent on line emission; with Seyfert I galaxies having both narrow and broad emission lines, and Seyfert II galaxies presenting only narrow lines. The continuum of Seyfert I galaxies often outshines the emission of the whole galaxy. Seyfert I galaxies are more frequently X-ray emitters than Seyfert II, and the spectrum of those few Seyfert II X-ray emitters hint at absorption by large hydrogen column densities.

A similar classification scheme is applied to radio galaxies, extremely bright in radio wavelengths, and they are consequentially divided in broad-line radio galaxies (BLRG) or narrow-line radio galaxies (NLRG). Radio-galaxies sometimes present jets, halos or radio-lobes.

Quasars (from quasi-stellar radio source) appear in the optical as point or star-like sources, whose host galaxy is hard to resolve in most cases. They are characteristically blue, compared to normal stars. Although the brightest quasars are strong radio emitters, many AGN candidates that appear as quasi-stellar sources are weak

in radio, and so they are termed quasi-stellar objects instead (QSO) to differentiate them from radio-loud quasars (QSR). The exact notation depends on the context. Quasar spectra tends to resemble those of Seyfert I galaxies, while Seyfert II galaxies find no quasar counter-part. However, some argue that ultraluminous infrared galaxies (ULIRGs) correspond to the "quasars II" group.

In the case of blazars, the low viewing angles and the high bulk Lorentz factors make relativistic effects particularly important. These sources appear as highly beamed by relativistic effects, and usually display apparent superluminal motions, strong variability, and polarization. Among them, distinction is traditionally made on whether they display emission lines (flat-spectrum radio quasars, FSRQ) or not (BL Lacs), although other classifications exist.

1.2 Special Relativistic Effects on Jet Emission

As it was emphasized during the previous discussion, relativistic effects are at the heart of the observed characteristics of blazar emission, and therefore the introduction of some concepts is a prerequisite for its understanding. Special relativity (SR, [4]) is a theory of spacetime, and its postulates can be stated as

- The laws of physics are the same in all inertial frames of reference.
- The speed of light is the same in all inertial frames of reference.

These simple postulates are enough to derive transformations relating physical quantities in different reference frames. Although there are many ways to derive the transformations, with different degrees of formality, we will content ourselves with stating that the proper length, ds (or equivalently, the proper time, $d\tau$), defined as

$$ds^2 = -(d\tau)^2 = -(cdt)^2 + dx^2 + dy^2 + dz^2 \tag{1.1}$$

along a path, is invariant. This automatically leads to the introduction of the position four vector x^μ, related to the usual Newtonian coordinates according to

$$x^\mu = \begin{pmatrix} x^0 \\ x^1 \\ x^2 \\ x^3 \end{pmatrix} = \begin{pmatrix} ct \\ x \\ y \\ z \end{pmatrix} \ , \tag{1.2}$$

which allows writing the proper length as

$$ds^2 = -\eta_{\mu\nu} dx^\mu dx^\nu \ , \tag{1.3}$$

Class	Sub-class	Description
Seyfert	Type 1	Broad and narrow emission lines, weak radio, X-ray emission, spiral galaxies, variable
	Type 2	Only narrow emission lines, weak radio, weak X-ray, spiral galaxies, not variable
Quasars	Radio-loud (QSR)	Broad and narrow e.l, strong radio, some polarization, FR II, variable
	Radio-quiet (QSO)	Broad and narrow e.l, weak radio, weak polarization, variable
Radio Galaxies	BLRG	Broad and narrow e.l, strong radio, FRII, weak polarization, elliptical galaxies, variable
	NLRG	Only narrow e.l, strong radio, FRI and FRII, no polarization, elliptical galaxies, not variable
Blazars	BL Lacs	Almost no e.l, strong radio, strong polarization, rapid variability, 90 % in ellipticals
	OVV quasars	Broad and narrow e.l, strong radio, strong polarization, rapid variability, much more luminous than BL Lacs
ULIRGs		Possibly dust-enshrouded quasars, alternatively may be starbust phenomena
LINERs		Similar to low-luminosity Seyfert 2, low-ionization emission lines, mostly spiral galaxies, alternatively starbust phenomena or HII regions

Table 1.1: AGN classification ([2]). Nowadays it is accepted that all these different objects correspond to different views of the same phenomenon, in a unified model of AGNs (see Figure 1.2).

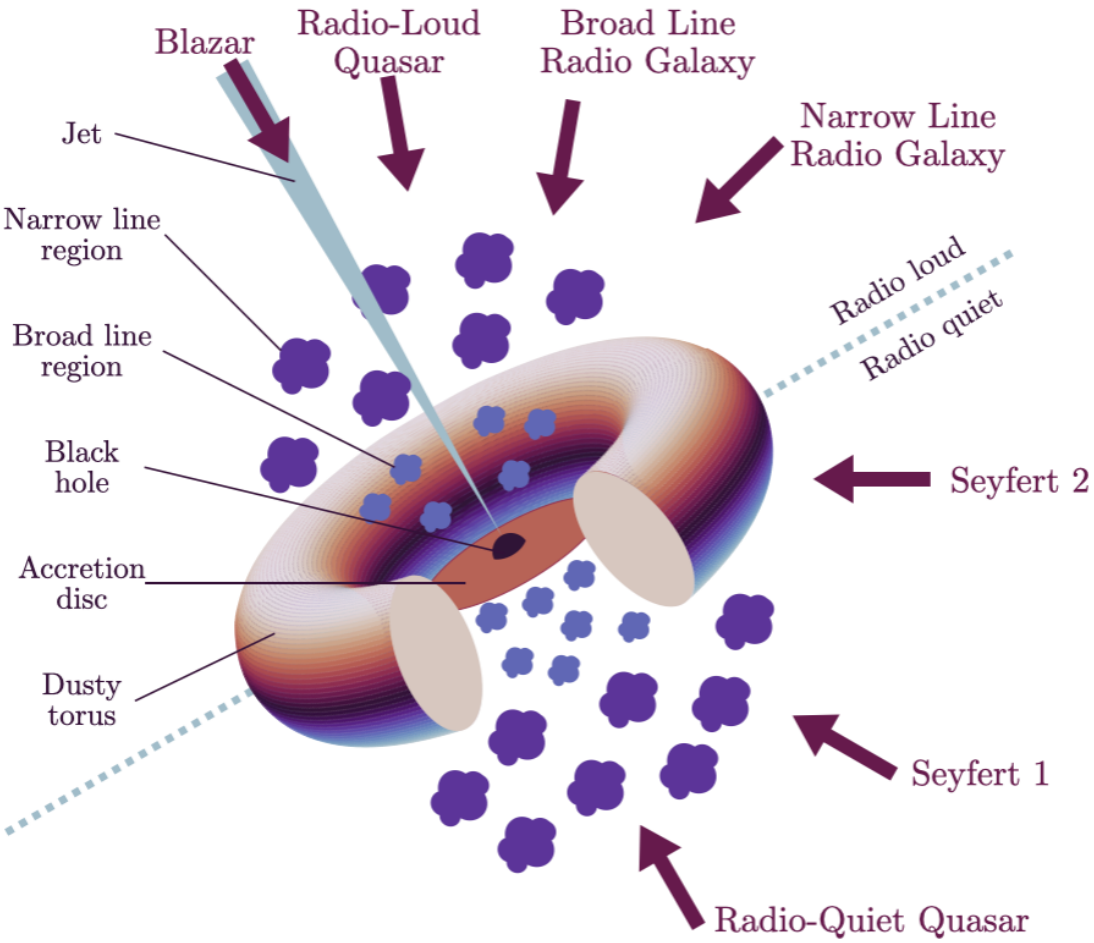

Figure 1.2: Unified model of AGNs. Different views or phases of the same phenomenon give raise to the rich spectrum of observational characteristics (see Table 1.1). Illustration adapted from [3] by Emma Alexander for Wikipedia, CC-BY.

with $\eta_{\mu\nu}$ the Minkowski metric defined by

$$\eta_{\mu\nu} = \begin{pmatrix} -1 & 0 & 0 & 0 \\ 0 & +1 & 0 & 0 \\ 0 & 0 & +1 & 0 \\ 0 & 0 & 0 & +1 \end{pmatrix} . \tag{1.4}$$

The basic object of manipulation in special relativity are four vectors. The set of transformations that preserve that invariant (or equivalently, the Minkowski metric) are called Lorentz transformations. Considering a particle traveling at speed v in any direction, we can see that the time in its own reference frame (where it is at rest) will be related to our time coordinate as

$$dt = \gamma d\tau \ , \tag{1.5}$$

where

$$\gamma = \frac{1}{\sqrt{1-\beta^2}} \tag{1.6}$$

is called the Lorentz factor and $\beta = v/c$ is its speed in units of the speed of light. Analogously, we can introduce the four velocity

$$u^\mu = \frac{\mathrm{d}x^\mu}{\mathrm{d}\tau} \ , \tag{1.7}$$

and the four-momentum as

$$p^\mu = mu^\mu = \begin{pmatrix} E/c \\ \boldsymbol{p} \end{pmatrix} . \tag{1.8}$$

Since $p_\mu p^\mu = -m^2$, we see that

$$E^2 = mc^2 + \boldsymbol{p}^2 \ . \tag{1.9}$$

For a macroscopic system, we usually work instead with the energy-momentum tensor. The energy-momentum tensor of the individual particles which make up the solid is $T_{\mu\nu}(x,t) = \gamma m v_\mu v_\nu$ at the position of each particle and zero elsewhere. The average of the diagonal terms is the kinetic energy and therefore the pressure. In the rest frame of the fluid, we can therefore write

$$T_{\mu\nu} = \begin{pmatrix} \rho & 0 & 0 & 0 \\ 0 & p & 0 & 0 \\ 0 & 0 & p & 0 \\ 0 & 0 & 0 & p \end{pmatrix} \tag{1.10}$$

With some reasoning, we can write a covariant version as

$$T_{\mu\nu} = (\rho + p)U_\mu U_\nu + p g_{\mu\nu} \ , \tag{1.11}$$

for a perfect fluid. Conservation of energy and momentum is written as

$$\partial_\mu T^{\mu\nu} = 0 \tag{1.12}$$

which in the non-relativistic regime will reduce to the Euler equations of fluid mechanics,

$$\partial_t \rho + \nabla \cdot (\rho \boldsymbol{v}) = 0 \tag{1.13}$$

$$\partial_t \boldsymbol{v} + (\boldsymbol{v} \cdot \nabla)\boldsymbol{v} = -\nabla p/\rho \ . \tag{1.14}$$

As we have already mentioned, the emission that we receive from blazars is affected by relativistic effects. Suppose a macroscopic region moving at us with an angle θ (in our frame) and speed β_Γ. We will need to distinguish between the individual movement of particles, and the bulk motion of the region. We will use Γ to refer to the bulk Lorentz factor of the region traveling at speed β_Γ. If we consider a photon emitted from this region and the scalar quantity $u^{em}_{em} \cdot p^{em}_{ph} = u^{obs}_{em} \cdot p^{obs}_{ph}$ in both the emission region and the observer frame, it can be seen that the energy in the rest frame of the emission and the observed energy will be related by

$$E = E_0 \delta \ , \tag{1.15}$$

where δ is called the Doppler factor

$$\delta = \frac{1}{\Gamma\left(1 - \beta_\Gamma \cos\theta^{obs}\right)} \ . \tag{1.16}$$

From this, we can already explain the reason why some jets appear to be one-sided only. In the extreme case where $\theta = 0$, as it is for a jet pointing towards us, emission seems boosted by $\delta = 2\Gamma$, while for $\theta = 180°$, it is decreased by a factor $\delta = 1/2\Gamma$. If we alternatively consider the quantity $u^{em}_{obs} \cdot p^{em}_{ph} = u^{obs}_{obs} \cdot p^{obs}_{ph}$, we obtain an equivalent expression with the emission angle,

$$E^{obs} = E^{em}\Gamma(1 + \beta_\Gamma \cos\theta^{em}) \ . \tag{1.17}$$

Comparing both expressions, one can see that at highly relativistic speeds ($\Gamma \gg 1$), photons emitted at a right angle $\theta^{em} = \pi/2$ will appear emitted at an angle $\theta^{obs} = 1/\Gamma$, and radiation is said to be beamed due to relativistic aberration.

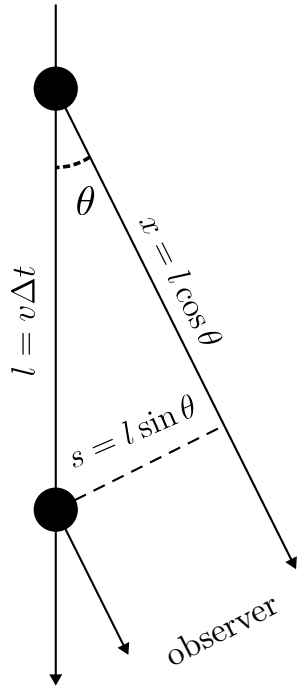

Figure 1.3: Illustration of apparent superluminal motion.

When we observe any of these objects, the quantity measured will usually be the radiant flux, $F_\nu = \mathrm{d}^2E \,/\, \mathrm{d}t\,\mathrm{d}A\,\mathrm{d}\nu$, or energy per unit time, area and frequency. Be composing the transformations of each of these quantities, we can see

$$F^{obs}_{\nu^{obs}} = F^{em}_{\nu^{em}}\delta^3 \ . \tag{1.18}$$

Another important and puzzling effect is apparent superluminal motion. Consider a photon emitted at time t from a region moving at speed β_Γ, and a photon emitted at a later time $t + \Delta t$, as illustrated in Figure 1.3. It can be seen that for the observer, the difference in arrival times will be $\Delta t^{obs} = \Delta t - \Delta t\beta_\Gamma \cos\theta$, and therefore the region will appear to move at a speed

$$v_{\perp,app} = \frac{v\sin\theta}{1-\beta_\Gamma\cos\theta} \ . \tag{1.19}$$

From this expression, one can see that there is a critical angle at which the apparent transverse speed is greatest, at $\cos\theta_{crit} = \beta_\Gamma$ or $\sin\theta_{crit} = 1/\Gamma$. We can use this information to put a lower limit on the bulk Lorentz factor. For any observed β_{app},

we can substitute the expression for the critical angle in (1.19) to obtain

$$\Gamma \geq \sqrt{\beta_{\perp,app}^2 + 1} \ . \tag{1.20}$$

We can also constraint the viewing angle by noting that at any viewing angle, the maximum apparent speed will be attained in the limit $\Gamma \to \infty$. Then,

$$\cos\theta_{max} = \frac{\beta_{\perp,app}^2 - 1}{\beta_{\perp,app}^2 + 1} \ . \tag{1.21}$$

1.3 Emission

A detailed derivation of the precise expressions that govern emission from AGNs is out of the scope of this thesis. However, we will review the fundamental principles behind the emission processes in AGNs and the most important results. Densities in AGNs jets are too low for binary particle collisions to be relevant, and therefore we will restrict ourselves to photon-particle interactions. Very rarely we will be interested in the radiation from a single particle. In general, we will focus on the spectrum from a population of particles. The energy distribution of the electron population is usually assumed to be a power law on the Lorentz factor in-between the low energy and high energy cut-offs, and zero otherwise, that is,

$$n(\gamma) = \begin{cases} n_0\gamma^{-p} & , \ \gamma_1 < \gamma < \gamma_2 \\ 0 & , \ \text{otherwise} \end{cases} \ . \tag{1.22}$$

There are many arguments for this approximation, among them, that first order and stochastic second-order Fermi acceleration naturally results in power-law spectrum of relativistic particles ([5]).

Synchrotron emission

It is known that the acceleration of a charged particle produces electromagnetic radiation. An electron moving in magnetic field will tend to rotate, and the radiation it will emit is known as Cyclotron radiation, if the electron is non-relativistic, or Synchrotron radiation in the relativistic limit. The power emitted by a single particle of mass m and charge q, moving with a Lorentz factor γ in a constant magnetic field B at pitch angle ϕ (angle of its velocity relative to the magnetic field) is

$$\left(\frac{\mathrm{d}E}{\mathrm{d}t}\right)_{\text{synch}}(\psi) = -\frac{16\pi c}{3}\left(\frac{q^2}{mc^2}\right)^2 u_B\beta^2\gamma^2\sin^2\phi \ , \tag{1.23}$$

where $u_B = B^2/8\pi$. From this formula it can be seen that electrons are much more efficient radiators than protons, while protons are more easily accelerated. The exact formula for the radiative output and its derivation can be found in several sources ([5]), and it is not of use here. We will just say that Synchrotron emission, averaged isotropic ally over all pitch angle, from a single particle peaks at a frequency

$$\nu_c = \frac{3qB}{4\pi mc}\gamma^2 \ . \tag{1.24}$$

When considering the spectrum of a particle distribution, a common approximation (known as the delta approximation), is to assume that all power is emitted at this frequency. The emission coefficient can then be written as

$$j_\nu^{\mathrm{synch},\delta} = \frac{4}{9}\left(\frac{q^2}{mc^2}\right)^2 u_B \nu_0^{-3/2}\nu^{1/2} n(\sqrt{\nu/\nu_0}) \ , \tag{1.25}$$

where $\nu_0 = \nu_c/\gamma^2$ is not dependent on γ (Eq. 1.24). This approximation is valid for most use-cases. It can be seen that the Synchrotron emission from a population of electrons following a power-law with index p follows also a power law with spectral index

$$\alpha = \frac{p-1}{2} \ . \tag{1.26}$$

An identifying characteristic of synchrotron radiation is its polarization. The maximum linear polarization degree expected from a power law electron distribution depends on the spectral index as ([6])

$$\Pi = \frac{p+1}{p+7/3} \ . \tag{1.27}$$

For typical electron indices ($p \simeq 2$), this is around 70 %. No other emission mechanism is expected to produce significant polarization, therefore observation of high degrees of polarization is a observational confirmation of synchrotron radiation.

Synchrotron self-absorption

Any emission process must be accompanied by a corresponding absorption process. The absorption of photons by relativistic electrons in a magnetic field is called synchrotron self-absorption. We omit the tedious procedure to derive the exact form of the absorption coefficient and motivate instead its spectral shape through thermodynamic arguments. In the low temperature regime, the Planck law for the black-body

spectrum can be approximated by the Rayleigh-Jeans formula, which is used as the definition for the brightness temperature through

$$S_\nu = \frac{2\nu^2 k_B T_b}{c^2} \ . \tag{1.28}$$

On the other hand, although the distribution of electrons for a power-law does not follow a relativistic thermal (Maxwellian) distribution, at each frequency, they can be associated with a an effective temperature through the (relativistic) kinetic energy term and the (relativistic) degrees of freedom as $\gamma m_e c^2 = 3kT_e$. Since $\gamma \sim (v/v_g)^{1/2}$, at low frequencies, the brightness temperature of the relativistic electrons can not be higher than the kinetic temperature, and the spectrum has to be absorbed with a spectral shape

$$S_\nu \propto \nu^{5/2} \ . \tag{1.29}$$

It might happen that the frequency at which this absorption process takes hold is below the range in which synchrotron emission from the electron population can be well approximated by a power-law, and the energy distribution is thermal, i.e. $\nu_{SSA} < \nu_c(\gamma_1)$, in which case the emission will follow the typical $S_\nu \propto \nu^2$. Since real astrophysical sources are not homogeneous and contain some thermal population of electrons, the real slope will always be smaller than 5/2. The simple observation of the low frequency tail of the spectrum can throw information about whether we are looking at a thermal distribution of electrons or not. In the same way, we can use the observed brightness temperature at sufficiently low frequencies (in the self-absorbed part of the spectrum, where $T_e \sim T_b$) to estimate the magnetic field strength as

$$B \sim \left(\frac{2\pi m_e c\nu}{qB}\right)\left(\frac{m_e c^2}{3kT_b}\right)^2 \ . \tag{1.30}$$

Inverse Compton

The Compton effect is the scattering of a photon off a charged particle. When the energy of the incident photon is much less than the energy of the particle ($h\nu \ll mc^2$), that is, in the classical limit, the photon scatters elastically, and the effect is called Thomson scattering. When the energy of incoming photon is comparable to the energy of the particle, the effect is called Compton scattering, and is described by the Klein-Nishina cross-section ([7]).

In the emitting region of a relativistic jet, photons with energy ranges from radio to X-rays scatter off relativistic electrons. In the rest frame of any of these electrons, we might restrict ourselves to the Thomson limit, and consider that the incident

and scattered photon have similar energies ($\epsilon'_{out} \sim \epsilon'_{in}$). Therefore, in the laboratory frame, i.e. the co-moving frame of the emitting region, the out-going photon will be Lorentz boosted to an energy $\epsilon_{out} \sim \epsilon'_{in}\gamma$, while the incident photon energy will be $\epsilon'_{in} \sim \epsilon_{in}\gamma$. Therefore,

$$\epsilon_{out} \sim \gamma^2 \epsilon_{in} \ , \tag{1.31}$$

and photons scattered off relativistic electrons in the jet gain energy in what is known as the inverse Compton effect.

There was some severe hand-waving in this reasoning. For one, the effect of the angle between the electron and the photon was ignored. But detailed analysis such as that found in [8, 5] shows that the spectrum of scattered mono-chromatic photons off the power-law abiding electrons follows also an approximate power-law spectrum with the same spectral index.

A consequence of this up-scattering is that electrons in the jet loose energy. The ratio between the luminosity by inverse Compton in the Thomson regime, and the luminosity by synchrotron emission will be given by the ratio between energy density of the scattered photon-field and the magnetic field density,

$$\frac{L_{\rm IC,Thomson}}{L_{\rm synch}} = \frac{\dot{\gamma}_{\rm Thomson}}{\dot{\gamma}_{\rm synch}} = \frac{u_{ph}}{u_B} \ . \tag{1.32}$$

In the jet, the photons up-scattering through inverse Compton might have different origins and energy distribution, e.g thermal photons from the accretion disk or the torus (termed external Compton, EC), or even the synchrotron photons generated by the same electron population (termed synchrotron self-Compton, SSC).

1.4 Other Particle Interactions

As we already mentioned, binary particle interactions are not thought to be significant contributors to the emission of blazars because of the low density in these environments. However they are important to explain the observed spectrum, due to their effect on the propagation of light from these objects, and their relevant role in our observational techniques, therefore we will summarily describe them here.

Bremsstrahlung

Bremsstrahlung refers to the electromagnetic radiation produced by the deceleration of a charged particle by another charged particle, typically an electron or positron by an atomic nucleus. Although bremsstrahlung is not thought to be an important

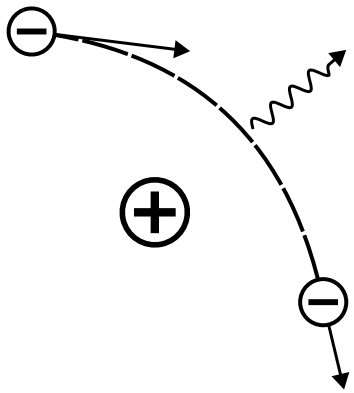

Figure 1.4: Schematic representation of the bremsstrahlung radiation process.

process in explaining the observed spectrum of blazars for the reason outlined in the introduction of this section, it plays a significant role in γ-ray astronomy with IACTs, as an essential step in the development of electromagnetic cascades (Section 2.4), and therefore we include it here. The process is represented in Figure 1.4. It is sometimes referred as free-free radiation, in reference to the unboundness of the incoming and outgoing electrons.

Pair Production

Energetic γ-ray photons can disintegrate into electron and positron pairs, in what is known as pair production. A single, energetic γ-ray photon requires the presence of a nearby nucleus to disintegrate into e^-/e^+ pairs. To see why a single photon can not disintegrate by itself, it is enough to consider momentum conservation. Momentum of the e^-/e^+ pair in their center of mass frame is zero, but there is no reference frame in which the momentum of a single photon is zero. The threshold energy for this process is twice the mass of the electron, $m_e \simeq 0.51\,\mathrm{MeV/c^2}$.

Alternatively, two photons can interact to produce pairs. VHE γ-ray photons from blazars and other distant sources are absorbed through interaction with the extra-galactic background light (EBL), the diffuse background infrared light from dust in star-forming galaxies and infrared and optical light from stars. The EBL is difficult to measure directly due to the light coming from the solar system (Zodiacal light) and the Milky Way. However, EBL absorption significantly affects blazar emission at high energies. The $\gamma\gamma$ cross-section shows that photons of energy ϵ will interact primarily with photons of energy $2/\epsilon$ (in units of $m_e c^2$). Therefore, 100 GeV-1 TeV photons will probe the near and far infrared parts of the EBL, respectively.

The process of $\gamma\gamma$ absorption can also be significant at the site of emission due to high photon densities, if the region is said to be compact to γ-rays. The effect is to produce a break at very-high energies that can be used to constraint the Doppler factor.

Photon-pion Production, the GZK Limit

It is also though that AGNs might be the source of some of the highly energetic ($\geq$ PeV) cosmic rays (mainly protons) that we observe at Earth. At these energies, protons interact with CMB photons through meson resonance to produce pions:

$$p \ + \ \gamma_{\mathrm{CMB}} \ \rightarrow \ \Delta^{+} \ \rightarrow \ p \ + \ \pi^{0} \ , \tag{1.33}$$

$$p \ + \ \gamma_{\mathrm{CMB}} \ \rightarrow \ \Delta^{+} \ \rightarrow \ n \ + \ \pi^{+} \ . \tag{1.34}$$

The process depletes protons of energy, hindering their propagation through the intergalactic medium. The energy of the Cosmic Microwave Background (CMB) photons ($T \simeq 2.7\,\mathrm{K}$, or $6.6 \times 10^{-4}\,\mathrm{eV}$) sets a threshold energy for protons at $\sim 5 \times 10^{19}\,\mathrm{eV}$. Protons with a higher energy will be decelerated, and the processes effectively places a limit on the maximum energy for extra-galactic cosmic rays known as the Greisen–Zatsepin–Kuzmin (GZK) limit. The existence of the GZK limit has been verified experimentally, and the break in the cosmic ray spectrum has been measured by cosmic ray experiments such as the one at the Pierre Auger Observatory.

Ultra-high energy cosmic rays (UHECR) have been observed at energies much higher than the GZK limit for protons, including the famously cited Oh-My-God-Particle, that measured an energy of $\sim 3 \times 10^{20}\,\mathrm{eV}$ ([9]). Their origin however is not well understood, and neither is their nature; they might consist of heavier nuclei.

Hadronic Interactions

There is increasing evidence of hadronic processes taking place in blazars, and AGNs have been cited as a possible source of cosmic neutrinos ([10]). FSRQS are the most likely candidate among blazars, due to their denser photon densities compared to BL Lacs. Although in this thesis we concentrate on leptonic models for emission, hadronic models exist that can explain the high energy mission of blazars. While in leptonic models protons are assumed to have low enough energies not to be significant, ultrarelativistic protons, if present, might also emit synchrotron radiation. If the energy of the ultrarelativistic protons is high enough, they might also generate particle cascades that ultimately dominate the high energy range of the emission. Photo-hadronic or photo-meson processes result in the emission of neutrinos. The

interaction of photons with protons results in the emission of pions through the processes described above. Neutral pions disintegrate into photons ($\pi^0 \to \gamma + \gamma$), while charged pions decay emitting neutrinos, e.g.

$$\pi^+ \to \mu^+ + \nu_\mu \to e^+ + \nu_e + \bar{\nu}_\mu + \nu_\mu \ . \tag{1.35}$$

At high energies, multi-meson production production (π^0, π^+, π^-) dominates. For UHE protons, these processes dominate over pair production.

1.5 General Relativity: Black Holes

It has been long known that supermassive black holes (SMBH) are at the heart of many galaxies, and that they are the central engine powering the activity of AGNs and relativistic jets and blazars.

Black holes are a prediction of General Relativity (GR, [11]). In GR, spacetime itself is considered a field, in a similar way as electromagnetism in classic field theory. As we saw in our introduction of special relativity, the metric (the Minkowski metric, in SR) is the tensor describing the local characteristics of spacetime. As a field in classical theory, its dynamical equations must be derived from the Lagrangian of the field. The simplest non-trivial scalar that we can derive from the field, omitting those in zero and first derivatives (since they can be made locally zero with a change of coordinates), is the Ricci scalar, R. On the other hand, the dynamics of particles must arise from a Lagrangian term that involves an invariant related to the particle, such as ds, as we mentioned in Sec. 1.2. The dynamics of matter, as a field, must involve the energy-momentum density, $T_{\mu\nu}$. Therefore, we choose as our starting point in this discussion the Lagrangian density

$$\mathcal{L} = \sqrt{-g}R \ . \tag{1.36}$$

The action $S_H = \int \mathrm{d}^4x \sqrt{-g}R$ is known as the Hilbert action. To the gravitational field Lagrangian, one must add any other fields present in our theory, such as the electromagnetic. If only gravity and matter are considered, applying the principle of least action against variations of the gravity field $g_{\mu\nu}$ leads directly to the dynamical equations of gravity in GR, known as the Einstein equation,

$$G_{\mu\nu} = R_{\mu\nu} - \frac{1}{2}Rg_{\mu\nu} = T_{\mu\nu} \ . \tag{1.37}$$

The solution to Einstein equation with spherical symmetry and asymptotically flat spacetime is known as the Schwarzschild metric ([12]),

$$ds^2 = -\left(1 - \frac{2GM}{r}\right)dt^2 + \left(1 - \frac{2GM}{r}\right)dr^2 + r^2 d\Omega^2 \tag{1.38}$$

From this, little can be said apart from realizing that something weird happens at $r = 0$ and $r = 2GM$. This second radius is known as the Schwarzschild radius, $R_S \equiv 2GM$. To analyze the trajectory of particles, we need to turn back to the action, $S = m \int ds$, now with $ds = \sqrt{-g_{\mu\nu} dx^\mu dx^\nu}$. The principle of minimum action, $\delta S = 0$, leads to the equation of motion of a particle in curved spacetime, known as the geodesic equation

$$\frac{\mathrm{d}^2 x^\mu}{\mathrm{d}\lambda^2} + \Gamma^\mu_{\rho\nu} \frac{\mathrm{d}x^\rho}{\mathrm{d}\lambda} \frac{\mathrm{d}x^\nu}{\mathrm{d}\lambda} = 0 \ , \tag{1.39}$$

where $\Gamma^\mu_{\rho\nu}$ are known as Christoffel symbols and are derived from the metric. Careful analysis of this equation leads to the conclusion that far from the center $r \gg GM$, trajectories of particles are similar to those predicted by Newtonian gravity. This is the case for ordinary astrophysical objects such as planets and stars, where any trajectory outside the matter distribution will be far from the Schwarzschild radius, although even then the deviation from Newtonian might be detected (e.g. the precession of the perihelion of Mercury). Much closer to the origin, however, geodesics inside the Schwarzschild radius will inevitably lead to the singularity at $r = 0$, even null geodesic, i.e. light particles, which gives name to black holes. There are several other special radii in this solution. At $r = 3GM$, a photon might orbit in a unstable circular orbit. For massive particles, at $r = 6GM$ lies the innermost stable circular orbit.

Unfortunately, the Schwarzschild metric is only an idealization, and real black holes will also have charge and angular momentum. The Kerr-Newman metric ([13, 14]) describes such black holes. They are much richer, have two event horizons, and an outer region of space known as the ergosphere, where you can not help but rotate with the black hole. As esoteric as black hole physics might be for astrophysics, they are likely to play a fundamental role in jet formation, e.g. through the Blandford-Znajek mechanism ([15]), providing energy and angular momentum.

1.6 Accretion and Jet Formation

As we hinted already in the last section, the process of accretion and jet formation in a supermassive black hole is an inherently general-relativistic magnetohydrodynamical process, and therefore it is hard to analyze with precision. But the first important realization is that accretion plays the fundamental role of powering the emission from blazars, an unexpected result if we look at more familiar objects and astrophysical sources such as stars, where emission is mainly driven by nuclear reactions. In fact, accretion is the most efficient rest mass-energy conversion mechanism known. For a

non-rotating (Schwarzschild) black hole, the binding of a particle at the inner-most stable circular orbit at $r = 3R_S$ is $\sim 5\,\%$ of the rest energy. For a maximally rotation Kerr black hole, this percent goes up to $\sim 40\,\%$ at the last stable prograde orbit (at $r = 0.5R_S$). The accretion luminosity is given then by

$$L_{\text{Disk}} = \mu \dot{M} c^2 \ , \tag{1.40}$$

with $0.0572 < \mu < 0.423$ and $\dot{M}$ the rate of accretion, normally measured in $\mathrm{M}_\odot$/yr. This can be compared to the efficiency in rest mass-energy to radiation conversion in the proton-chain reaction to ^{4}He, of only $0.7\,\%$.

Another source of energy for rotating black holes might be the Blandford-Znajek mechanism ([15]), mentioned in Sect. 1.5. The power generated from this mechanism depends on the magnetic field, and the mass an geometry of the black hole, but can be comparable to the one obtain from Disk accretion, and a black hole might radiate up to a significant percent ($\sim 9\,\%$) of his rest mass in this way.

A constraint on the accretion is given by the Eddington luminosity, which is the limit at which the outwards radiation pressure balances gravity. Combining Eq. (1.40) with the expression for Eddington Luminosity assuming Compton scattering on electrons,

$$L_{Edd} = \frac{4\pi G m_p c}{\sigma_T} M \ , \tag{1.41}$$

we find a limit Eddington accretion rate, $\dot{M}_{Edd}(M, \mu)$. It is seen that the brightest quasars emit at luminosities near the Eddington limit. Central black hole masses can be inferred from the width of emission lines from the the BLR. Typical masses of SMBHs are found in the range $10^8 - 10^9\,\mathrm{M}_\odot$, with radio-loud quasars being generally more massive than low luminosity ones. The ratio $\dot{M}/M$ also suggests a lifetime for the quasar phase of AGNs, of around 10^8 yr.

1.7 Motivation

The preceding introduction to the concepts behind the blazar phenomenon makes it apparent how it implicates almost every branch of physics. Close to their central engine lies a supermassive black hole, and the interaction between black hole, space-time, magnetic fields and surrounding matter can only be explained in the framework of general-relativistic magneto-hydrodynamics (GRMHD). Farther down the jet, the particle energies, orders of magnitude higher than what any accelerator in Earth can achieve, makes the use of the Standard Model (SM) necessary to explain particle interactions, composition of the jet and emission. The scales involved, ranging from

the electron gyro-radius to hundreds of kiloparsecs, hinder exhaustive simulations of the whole process, and the most common approach is to perform simulations at different scales that need to be sewn together.

These same difficulties makes blazars a laboratory and an instrument that can be used to test many theories at the frontier of physics. Tests of General Relativity can be performed through direct imaging of the central black hole and its event horizon ([16]); the standard model is put to test in the jet composition and interaction with the surrounding medium. Because of their high luminosity, part of the farthest observed objects in the universe are blazars, placing them as an important object of study in cosmology. The light that arrives to us from them has had to travel over vast distances, and its weak interaction with the intergalactic magnetic fields (IGMFs) and the possible interactions with particles beyond the Standard Model (such as axion-like particles, ALPs, [17]) also makes them relevant in the search of a unified theory of physics (or at least, in the replacement for the current Standard Model). Systematic delays between emission at different wavelengths could also be used to search for Lorentz invariance violation (LIV, [18]). These last examples show why a complete and accurate understanding of AGNs and blazars is needed; only with accurate knowledge of the environment and physics in these objects can they be used to constrain possible new physics.

However, many aspects of blazars remain uncertain. Although there are many proposed mechanisms, it is not clear yet how jets form and how they remain collimated over such long distances. In addition, while jets are a common occurrence, we do not know exactly why some AGNs present jets, while others do not. One of the main questions is the composition of the jet, and whether leptonic or hadronic processes, or both, are responsible for the high-energy bump in blazar spectra. In leptonic scenarios, the second bump is accepted to be the result of inverse Compton scattering off relativistic electrons, but there is no agreement on the origin the scattered photon field. Hadronic models might explain the mounting evidence of neutrino emission from blazars, but are even more degenerate than leptonic models and require higher particle energies. A comprehensive approach to the problem requires combining multiple methods and extensive evidence. Dense and wide spectral coverage in multi-wavelength observations is crucial to overcoming the degeneracy of emission models. Polarimetry can offer insights into the underlying processes, while VLBI images can constrain the geometry and kinematics of the emitting region. We will put these approaches to test in the next chapters.

Chapter 2

Multi-wavelength Observations of Blazars

Having introduced the characteristics of blazars and the physical processes involved, we turn ourselves to their observational aspect. In this section we will review the astronomical techniques that are employed in the study of blazars, with special emphasis on the observations and instruments used during the realization of this thesis.

Part of the effort involved in the production of this thesis was directed at carrying out single-dish mm-wavelength photo-polarimetric observations at the IRAM 30m telescope, optical photo-polarimetric observations at Sierra Nevada and Calar Alto observatories, and very-high-energy γ-ray observations at the MAGIC and LST-1 telescopes. These facilities, their instruments and the observations will be described in more detail in the following sections. In addition, data from many other instrument and facilities was included in the works presented in this thesis, obtained from public archives and as part of data-exchange agreements and collaborations with other research groups (e.g. VLBA, SMA, *Swift*, *Fermi*, Perkins, and many others).

2.1 Radio Observations

Electromagnetic radiation in the radio part of the spectrum provides a way to observe many sources that are invisible to us in other wavelengths. For one, radio wavelengths encompass the largest atmospheric window available, from $\sim 0.3\,\mathrm{mm}$ to $\sim 15 - 30\,\mathrm{m}$ (Fig. 2.1). Wavelengths longer than $\sim 30\,\mathrm{m}$ get reflected by Earth ionosphere, while photons with wavelengths of around $\sim 0.3\,\mathrm{mm}$ have energies comparable to the vibrational transitions of common molecules such as CO_2, O_2 and H_2O, and are therefore absorbed. However, the ionized interstellar medium (ISM) already absorbs

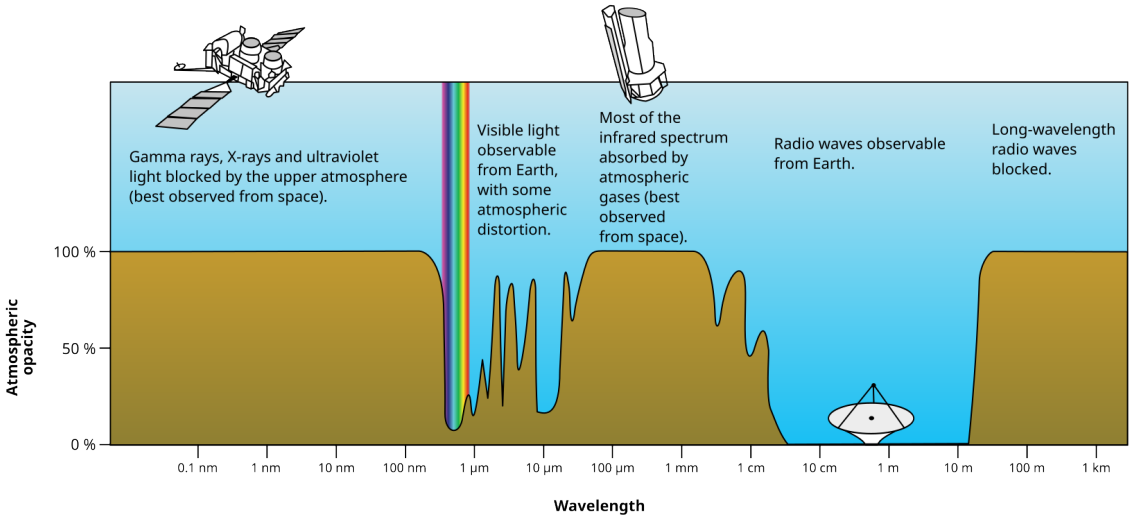

Figure 2.1: Earth atmospheric windows. Image: Wikipedia / NASA.

wavelengths $> 15\,\mathrm{m}$, and variable atmospheric refraction makes observations difficult at $\lambda > 1\,\mathrm{m}$.

Common thermal sources (e.g. stars) are too dim to be detected in the radio continuum spectrum, and therefore radio-astronomy allows probing different emission processes and environments than optical astronomy. It is no coincidence that radio-astronomy played a pivotal role in the understanding of quasars. In 1933, Carl Jansky, an American physicist and radio-engineer, detected a radio-signal from the direction of Sagittarius, towards the center of the Milky Way. The discovery constituted the first detection of a astronomical radio signal, and the source would later come to be known as Sagittarius A*.

The resolving power of a telescope is limited by diffraction at any wavelength through the relation

$$\theta \simeq \frac{\lambda}{D}\,, \tag{2.1}$$

where λ is the observation wavelength and D is the telescope aperture. Since radio wavelengths are orders of magnitude longer than optical ones, this relation severely limits the resolution of radio telescopes compared to optical ones. However, since radio telescopes are actually antennas, the signal from two telescopes can be correlated in a technique based on interferometry known as aperture synthesis, in which the limiting factor D is no longer the aperture of individual telescopes, but the physical separation between them. In practice, at least three antennas are required. In radio

interferometry, antennas at a given separation probe the Fourier space, also known as visibility plane, of the brightness -real- image. As such, multiple antennas with different separations are needed to accurately reconstruct the image of the source. In Very-long-baseline interferometry (VLBI), antennas are so far away that the signals are first recorded, preserving intensity and phase information, and then correlated. This technique allows for antennas to be distributed over different continents. The rotation of Earth can then be used to sample the visibility plane.

Single-dish photo-polarimetric mm-wavelength observations were carried out at the IRAM 30m telescope as part of the POLAMI monitoring program ([19, 20, 21]). Both linear and circular polarization are measured. In addition, Very Long Baseline Array (VLBA) data from the Boston University Blazar Group VLBA-BU-BLAZAR and BEAM-ME programs was reduced for intensity and polarization using `AIPS` ([22, 23]).

2.2 Optical Photo-polarimetric Observations

Optical photo-polarimetric observations were carried out at the Centro Astronómico Hispano-Alemán (CAHA) 2.2m telescope, in Almería, Spain (Fig. 2.3); and at Observatorio de Sierra Nevada (OSN) 0.9m and 1.5m telescopes, in Granada, Spain (Fig. 2.2). Most of the observations were carried out as part of the MAPCAT and TOP-MAPCAT monitoring programs ([24]). Observations at CAHA were done using the Calar Alto Faint Object Spectrograph (CAFOS), which has polarimetric capabilities. Photometric observations at OSN were mostly performed with the Andor CCD cameras, and polarimetric observations were performed with the same cameras and a polarized filter wheel until October 2023, when the DIPOL-I polarimeter was installed ([25]). The observational effort also included developing the necessary data analysis pipelines. This development culminated in the release of IOP4, an open-source pipeline described in Escudero Pedrosa et al. [26], included as part of this thesis in Chapter 5.

In an astronomical observation with an optical CCD (or similar) camera, the final pixel values (i.e. the images) will be given in Analog-to-Digital-Units (ADUs), which are related to photo-electrons through the gain factor. A well behaved optical detector is one for which this response is perfectly linear, and for our purposes we can assume it is always the case (as long as images are not saturated). The final pixel values can be symbolically written as

$$\text{pixel value} = \text{bias} + \text{dark current} + \text{noise} + \text{gain} \times \text{light} \tag{2.2}$$

Figure 2.2: Photograph of the Sierra Nevada Observatory. Image: OSN website.

The bias error corresponds to an offset voltage applied to ensure that there are not negative counts during the readout. The dark current corresponds to photo-electrons caused by the thermal noise in the detector. There is the additional complication that all these contributions, and also the gain, are pixel-dependent. To compensate them, a series of calibrating images (appropriately called bias, darks and flats) are taken every night and applied to our images before any other reduction takes place. Since the bias noise is time independent, bias images are taken as zero exposure time shots. Darks are normal images with the shutter closed. Flats images are taken with the camera looking at a uniform light source (usually, some part of the sky during sunset or sunrise). Flats also serve to compensate differences in transmission (e.g. because of dust) in the filters or other parts of the optics system.

After all these effects are corrected, the resulting pixel values are assumed to be proportional to the light received in each pixel, although there is remaining noise from the intrinsic readout error. In addition, the light received in each pixel still includes

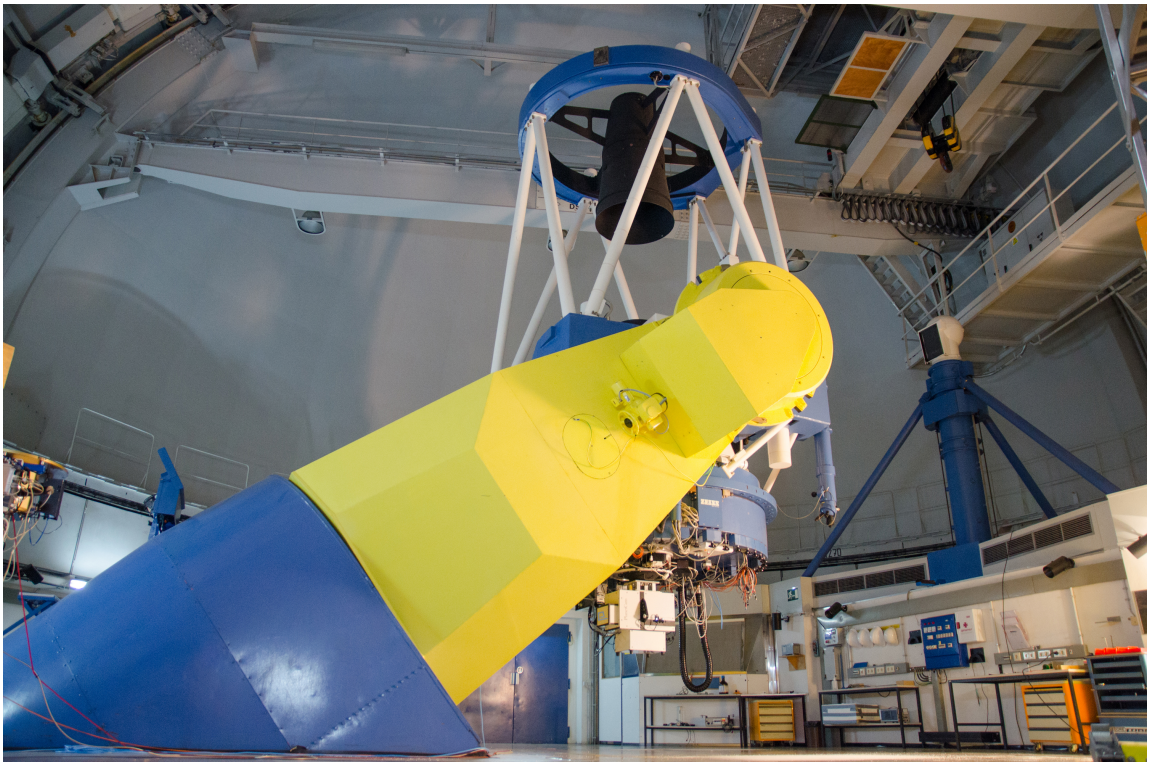

Figure 2.3: Calar Alto 2.2m telescope. Image: CAHA Outreach / Enrique de Juan.

contributions from other sources (e.g. from nearby stars and the sky brightness). For this reason, some form of background-subtraction is necessary. The easiest is perhaps defining an aperture radius around the position of our source in the image (which should include most of the flux) and an annulus around it. Since the light collected in the annulus will be mostly contributions from diffuse light noise, its average or median value is used to estimate the contribution of background light to the total light collected inside the aperture. The corrected value is taken as the instrumental flux of the source, F, and its logarithm is the instrumental magnitude, $m_{inst} = -2.5 \log_{10} F$.

Relative Photometry

The most common technique used for blazar optical photometric observations, and the one that we employed for our observations, is called *relative photometry*, which we now describe.

If the magnitude of a calibrator in the same field is known, the magnitude of the target source in the same system can be computed from the instrumental magnitudes of both the target and the calibrator by taking the logarithm in arbitrary units. Expanding the definition of magnitude for both target and calibrator,

$$m - m_0 = -2.5 \log_{10} F/F_0 = -2.5 \log_{10} F[\mathrm{u}] + 2.5 \log_{10} F_0[\mathrm{u}] \ , \tag{2.3}$$

$$m_{c,\mathrm{known}} - m_0 = -2.5 \log_{10} F_c/F_0 = -2.5 \log_{10} F_c[\mathrm{u}] + 2.5 \log_{10} F_0[\mathrm{u}] \ , \tag{2.4}$$

Then, the two equations can be subtracted to give

$$m = m_{inst} + m_{c,\mathrm{known}} - m_{c_i nst} = m_{inst} + m_{c,zp} \tag{2.5}$$

The zero-point $m_{c,zp}$ is often averaged over several calibrators in the same field.

The main advantage of this technique is that most atmospheric and instrumental effects such as extinction can be ignored (or, it is more correct to say, are automatically compensated).

Optical Polarimetry

The polarization state of light can be described through the Stokes parameters $S(I, Q, U, V)$. These are related to the expectation values of the squared components of the electric field vector. The degree of linear polarization and the polarization angle are related to the Stokes parameter through

$$P = \sqrt{Q^2 + U^2}/I \ , \tag{2.6}$$

$$\chi = \frac{1}{2} \arctan \frac{U}{Q} \ . \tag{2.7}$$

The relationship between the Stokes parameters and the instrumental flux depends on the instrumental setup. The exact formulas for polarized filter wheels and half-wave plate retarders can be found in [26] (Chapter 5).

2.3 X-ray Observations

X-rays can not penetrate the atmosphere, making ground-based observatories impossible. X-ray instruments onboard satellites usually make use of grazing optics to circumvent the high penetrative power of X-rays. Since the incidence angle has to be nearly 90°, several nested mirrors are used to increase the effective area, resulting in long instruments. At the end of the grazing optics there is usually a CCD camera.

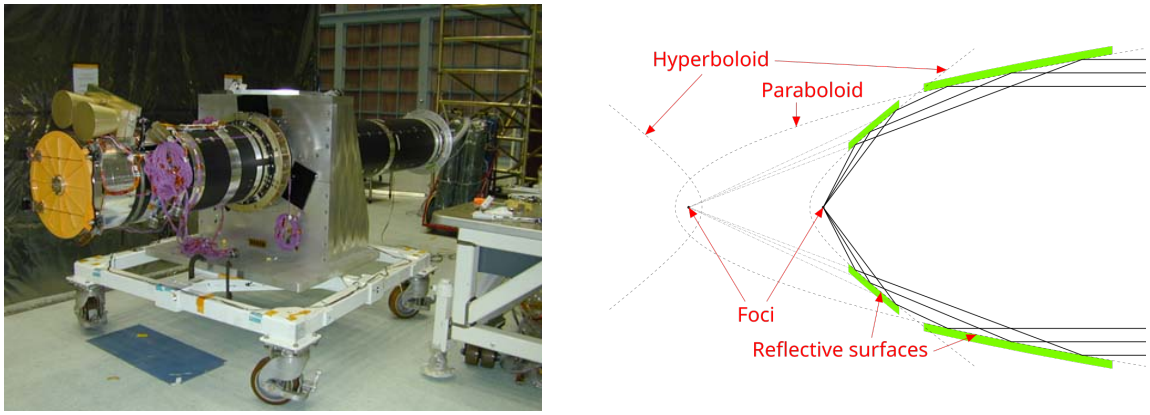

Figure 2.4: The XRT telescope subsystem. XRT is a Wolter I telescope. The use of grazing optic makes X-ray instrument relatively long. Credit: NASA / Wikipedia.

Thermal emission requires millions of Kelvins to emit significant X-ray radiation (e.g. stellar coronas). Quasars, X-ray binaries, and other objects emit X-rays of non-thermal origin through synchrotron and inverse Compton radiation.

The works presented in Chapters 3 and 4 include X-ray data from the *RXTE* (Rossi X-ray Timing Explorer) satellite in the $2.4 - 10\,\mathrm{keV}$ range, and from the XRT instrument (Fig. 2.4) onboard the *Swift* satellite in the $0.2 - 10\,\mathrm{keV}$, reduced to obtain light curves and spectra.

2.4 Gamma-ray Observations

Earth atmosphere is opaque to γ-rays (Fig. 2.1). Energetic γ-ray photons interact with atoms in the atmosphere, disintegrating into electron-positron pairs. For this reason, γ-ray astronomy started of as a satellite-based science, and in fact Gamma-Ray-Bursts (GRBs) were actually serendipitous discovered by the United States military with the γ-ray satellites that monitored the Earth in search of nuclear detonations. However, at very-high-energies ($> 100\,\mathrm{GeV}$), photon fluxes from astronomical objects are too low for satellites to collect enough statistics. The use of ground-based telescopes, with larger collection areas, is required.

If the γ-ray is energetic enough, the e^-/e^+ pairs produced by it can themselves interact with the atmospheric nuclei and in turn emit other γ-rays (bremsstrahlung radiation, Sect. 1.4). Other energetic particles arriving at the atmosphere (cosmic rays) can undergo a similar process, albeit the chain of disintegrations is much more complex (Figure 2.5). The result in both cases is a cascade of particles, known as

Extensive Air Shower (EAS). The particles that comprise the cascade travel at speeds higher than the speed of light in the medium, and therefore they emit Cherenkov radiation. EAS are initiated at $20 - 30$ km above sea level (a.s.l.). They develop, reach their maximum, and end, at around 10 km a.s.l. The Cherenkov light they emit is highly beamed in the direction of propagation of the particles, illuminating an area of some hundred meters wide at ground level (Figure 2.6).

Imaging Atmospheric Cherenkov Telescopes (IACTs) detect the Cherenkov light emitted by particle cascades. This Cherenkov light falls in the near ultraviolet (UV) range. Cherenkov telescopes are therefore optical telescopes. Their camera is usually made of detectors with ultra fast response and very low sensitivity detectors, to be able to capture the faint and extremely fast (in the order of tens of nanoseconds or less in duration) flashes of Cherenkov light. One of the most challenging aspects of IACTs is the need to discern γ-initiated showers, also known as electromagnetic (EM) showers, from EASs produced by other energetic particles such as cosmic rays. Figure 2.7 show the images produced by a γ-ray photon, an hadron, and a muon, respectively. Muons produce the most distinctive images in the camera, appearing as rings that can be used to calibrate the telescope. Gamma-hadron ($\gamma - h$) separation on the other hand is more challenging and is usually done using machine-learning (ML) techniques such as Random Forest (RF) classification. EM showers are more regular than hadronic ones, and produce ellipses on the camera that are parameterized through the Hillas parameters. These are used to reconstruct the direction of arrival and the energy of the photon. Several telescopes can be used in *stereo* mode to improve the reconstruction of the direction of arrival. IACT astronomy was pioneered by the Whipple telescope, in Southern Arizona. Whipple operated from 1968 to 2013, and detected the first TeV γ-ray source in 1989 (the Crab Nebula). The next generation of IACTs, e.g. VERITAS, HESS, and MAGIC, are still running to this day, and will soon give place to the next-generation Cherenkov Telescope Array Observatory (CTAO). CTAO which will be the first open γ-ray observatory in the world ([27]).

Other techniques such as Air Shower Arrays attempt the direct detection of the particle cascades as they reach the ground, such as is the case for γ-rays with energies > 100 GeV. Examples of this technique are HAWC or the Pierre Auger Observatory. They employ arrays of detectors, that can take the form of water tanks, laid out to cover an area as large as possible. Their advantage is a much larger field of view (FoV), a greater sensitivity at higher energies, and the ability to observe also during the day. Their main disadvantage is their poor angular resolution.

This thesis includes data from the Large Area Telescope onboard the *Fermi* satellite, reduced to obtain light curves and spectra. A significant effort was spent con-

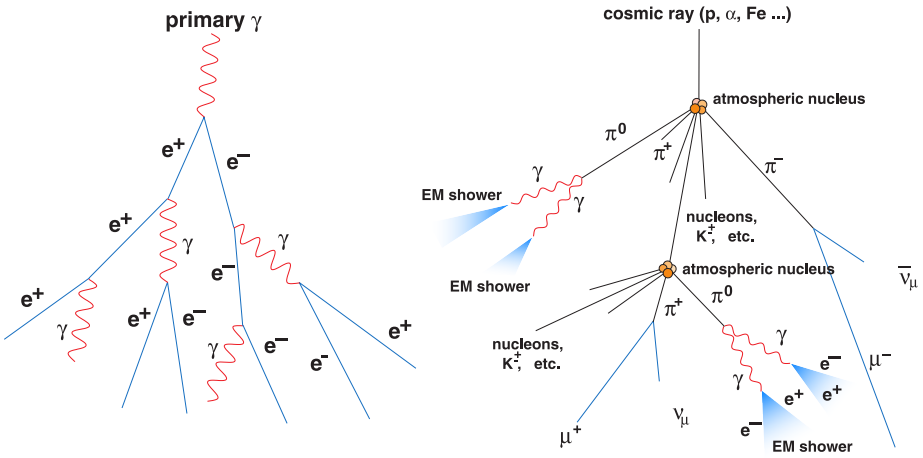

Figure 2.5: Particle cascades and by-products of γ-ray and hadron disintegration. Gamma-ray photons disintegrate in electron-positron pairs, which interact with atomic nuclei producing more γ-ray photons. On the other hand, collision of cosmic rays have a much more complex outcome. Image: [29].

ducting on-site observations with both the MAGIC telescopes and the LST-1 telescope in La Palma, Spain, serving first as Operator, then as Deputy Shift Leader and as Shift Leader, for a combined total of more than five months. The LST-1 observed BL Lacertae during its brightest recorded flare in August 2021 (observing shift P030, Shift Leader), detecting VHE γ-ray variability on the scale of minutes ([28]). The discovered variability constrains the possible regions sizes, and consequently the possible emission models. An example of such model is shown in Figure 2.9, where a multi-zone model of the MWL emission has been used to reconcile the observed VHE γ-ray emission and its variability with the constraints from optical and VLBI data. The data and corresponding analyses are part of several articles in preparation by the LST-1 collaboration, and have already been presented in several conferences.

2.5 Cross-Correlation Analysis of Light Curves

Cross-correlations analysis can shed important information about the temporal and spatial structure of emitting regions ([33]). Emission in many astrophysical scenarios can be modeled as the output of a system to an input function, convolved with a transfer or response function ([34]). Direct study of this convolution is rarely possible due to observational constraints, in which case correlation studies might still be able

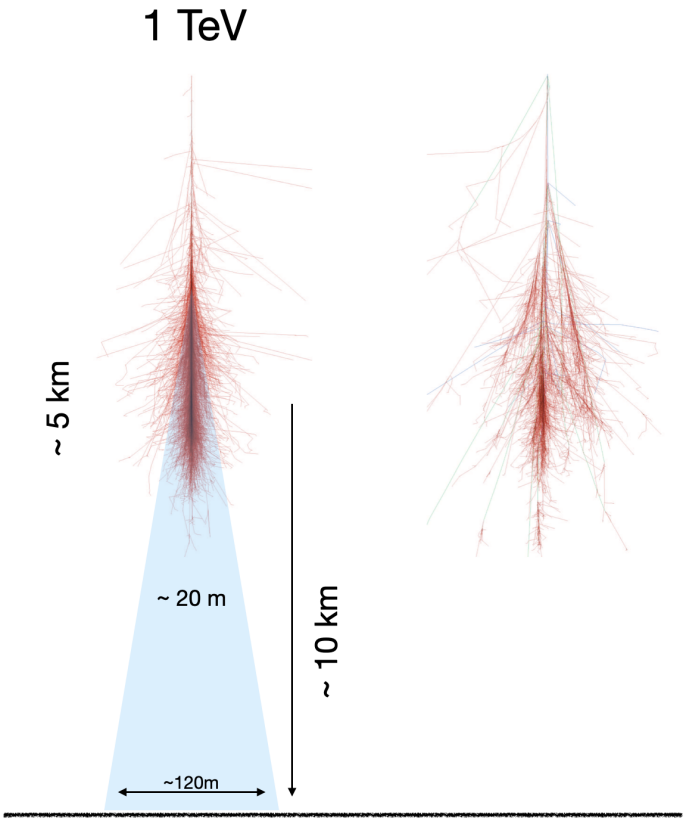

Figure 2.6: Comparison of a 1 TeV γ-initiated and a hadronic-initiated particle cascade, showing the approximated scales involved. Cascade plots: [29].

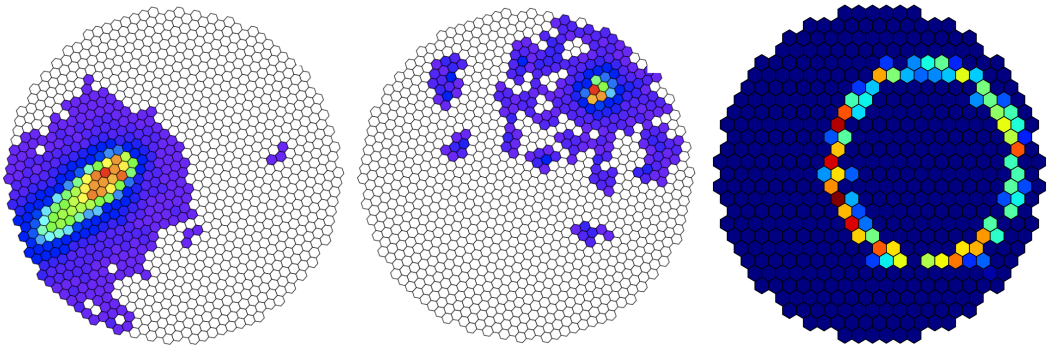

Figure 2.7: Comparison of the images produced in a IACT camera by showers initiated by a γ-ray (left), an hadron (middle), and a muon (right). Images: [30, 29, 31, 32].

Figure 2.8: The LST-1 prototype at the Roque de los Muchachos Observatory (ORM). The observatory is located in La Palma, Spain, and will be the home of the CTAO-North site. Image: CTAO website / Iván Jiménez (IAC).

to ascertain some information about the regions involved. Even when this "linear response interpretation" is not available, correlations still provide a statistical tool to study multi-wavelength emission. Here we summarily describe the definitions and methods used to compute the correlations.

For two deterministic continuous signals, $x(t)$ and $y(s)$, the two-point correlation is defined as

$$C_{x,y}(t,s) = \frac{(x(t)-\bar{x})(y(s)-\bar{y})}{\sigma_x \sigma_y} \ , \tag{2.8}$$

and the cross-correlation function as its trace

$$C_{x,y}(\tau) = \int dt C(t+\tau, t) \ . \tag{2.9}$$

The interpretation of this function is immediate from its definition. The obvious generalization for discrete signals is known as the Discrete Correlation Function (DCF),

$$C_{x,y_k} = \sum a_n b_{n+k} = \frac{(x_n-\bar{x})(y_{n+k}-\bar{y})}{\sigma_x \sigma_y \mathrm{len(x)}} \ . \tag{2.10}$$

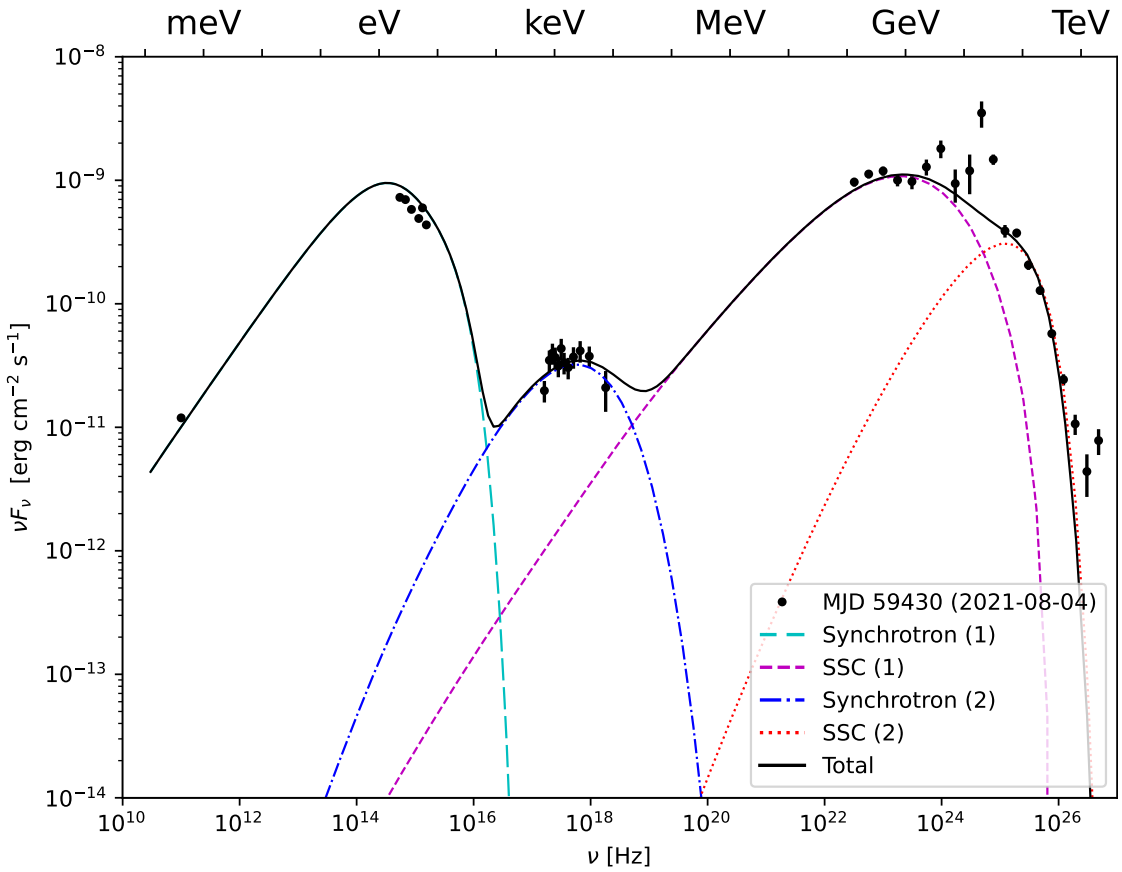

Figure 2.9: 2-zone SSC model for the LST observations of BL Lacertae. In this model, the detected very-high-energy γ-ray variability is explained by a secondary emission zone that also explains the spectral shape of the X-ray part of the spectrum during its high state. The model also explains the apparent correlation between v.h.e. γ-ray flares and the high X-ray emission.

If these x_n, y_m are a constant-rate sampling of the continuous signals $x(t)$, $y(s)$, these two functions are related up to a scaling in time, and the discrete correlation function tends to its continuous analog when the sampling rate is high. However in many cases, and specially in astronomy, observations are not made at constant intervals. Then we are left with only two options, interpolating the signals or interpolating the correlation function. Usually the second method is preferred as the first one is equivalent to inventing new data. For this reason, Edelson and Krolik [34] proposed computing the correlation function as

$$C(\tau) = \frac{1}{M} \sum_{i,j} \frac{(x_i - \bar{x})(y_j - \bar{y})}{\sigma_x \sigma_y} \ , \tag{2.11}$$

where the sum is over all pairs x_i, y_j such that

$$\tau - \Delta\tau/2 < t_i - t_j < \tau + \Delta\tau/2 \ , \tag{2.12}$$

and M is the number of pairs. This is equivalent to averaging within a certain resolution. The proper choice of this parameter $\Delta\tau$ depends on the characteristics of the data. Too low and there will be too little or no points to sum over, too high and all information will disappear. Usually we will choose a value such that the there are enough points in all bins for the correlation to be smooth without losing information, such a value is related to the scale of variability of the data. A problem of this definition of correlation function is that it is not normalized. A variation of it was proposed by Welsh [35], who argued that using the mean over all the light curves in (2.11) does not provide the best estimate of (2.9), and advocates using the mean and standard deviation over the M pairs used. Whether this correction is of any usefulness will depend on how good our Monte Carlo approach to generating synthetic light curves is.

The generation of synthetic light curves is necessary to estimate the significance of the correlation produced by either of these formulas. Several methods can be used depending on quantitative and qualitative characteristics of the original light curve. The simplest of them is *sampling*, which gives a light curve with identical mean and standard deviation, but whose shape will usually be very different from the original since all continuity is lost.

Methods based on the *randomization of the Fourier transform* give continuous light curves with identical mean and standard deviation, and a similar Power Spectral Density (PSD), whose qualitative shape is sometimes very similar to the original ones, specially at radio wavelengths, although it fails for optical and high energy light curves, where peaks are sparser and narrower. The Fourier transform can be

randomized by keeping the magnitude of the coefficients and introducing a random phase as

$$y(t) = \int \mathrm{d}f\, \hat{x}(f) e^{-2\pi i \phi(f)} \ , \tag{2.13}$$

where $\phi(f)$ is a random phase vector such that $\phi(-f) = \phi(f)$ and its values are uniformly distributed between -1 and +1. The only difficulty in this method is in the estimation of the Fourier transform since our light curves are never evenly sampled; estimation using the Non-Uniform Fast-Fourier Transform or the Lomb-Scargle Periodogram is necessary. Signals generated this way will have a similar variability since the power spectral density is defined -for a continuous signal- as the modulus of the Fourier transform $S_{xx}(f) = |\hat{x}(f)|^2$.

Lastly, we cite generation through an *stochastic process*, in particular through the *Orstein-Uhlenbeck* process, which can be physically motivated as a good approximation for blazar light curves, taking into account the state of magnetic fields and the magnetohydronynamics inside the accretion disk (see [36]), and is seen to behave very well with high energy data. It is described by a stochastic differential equation (SDE),

$$dX = \theta(\mu - X)dt + \sigma X dW dt \ , \tag{2.14}$$

where the first term is a deterministic term driving the system into its equilibrium state, and the second term is the stochastic part, a Gaussian noise term proportional to the intensity itself. The parameters θ, σ and μ need to be estimated looking at the statistical distribution of the original light curve. By finding the parameters that better fit our original light curve, we can integrate this SDE to generate many instances of random light curves with characteristics (mean, standard deviation, distribution and even PSD) similar to the original one. To obtain these parameters we use the Maximum Likelihood Estimation method, which finds the parameters that maximize the likelihood of obtaining some experimental data. For this, the probability density function for (2.14) is needed. The resulting expressions can be found again in [36]. In many cases, degeneracy of these parameters makes some trial and error necessary to find which values produce the most similar synthetic light curves.

All these methods for correlation and generation of synthetic light curves have been implemented in an open source package called `MUTIS` (MUltiwavelength TIme Series: a Python package for the analysis of correlations of light curves and their statistical significance), which is available at `https://github.com/IAA-CSIC/MUTIS`.

Chapter 3

Repeating Flaring Activity of the Blazar AO 0235+164

The article has been accepted and published in *Astronomy & Astrophysics* (`https://doi.org/10.1051/0004-6361/202346885`). The full reference can be found at [37].

A&A, 682, A100 (2024)
https://doi.org/10.1051/0004-6361/202346885

Astronomy & Astrophysics

Repeating flaring activity of the blazar AO 0235+164

J. Escudero Pedrosa[1], I. Agudo[1], A. Tramacere[2], A. P. Marscher[3], S. Jorstad[3,12], Z. R. Weaver[3], C. Casadio[5,4], C. Thum[6], I. Myserlis[6], A. Fuentes[1], E. Traianou[1], J.-Y. Kim[7,8], J. Kramer[7], R. López-Coto[1], F. D'Ammando[9], M. Bernardos[1], G. Bonnoli[10,1], D. A. Blinov[4,5], G. A. Borman[11], T. S. Grishina[12], V. A. Hagen-Thorn[12], E. N. Kopatskaya[12], E. G. Larionova[12], V. M. Larionov[12], L. V. Larionova[12], D. A. Morozova[12], S. S. Savchenko[12,13,14], I. S. Troitskiy[12], Y. V. Troitskaya[12], and A. A. Vasilyev[12]

[1] Instituto de Astrofísica de Andalucía, CSIC, Glorieta de la Astronomía s/n, 18080 Granada, Spain
e-mail: jescudero@iaa.es
[2] Department of Astronomy, University of Geneva, ch. d'Ecogia 16, 1290 Versoix, Switzerland
[3] Institute for Astrophysical Research, Boston University, 725 Commonwealth Avenue, Boston, MA 02215, USA
[4] Institute of Astrophysics, Foundation for Research and Technology – Hellas, Voutes 70013 Heraklion, Greece
[5] Department of Physics, University of Crete, 71003 Heraklion, Greece
[6] Institut de Radioastronomie Millimétrique, Avenida Divina Pastora 7, Local 20, 18012 Granada, Spain
[7] Max-Planck-Institut für Radioastronomie, Auf dem Hügel 69, 53121 Bonn, Germany
[8] Department of Astronomy and Atmospheric Sciences, Kyungpook National University, Daegu 702-701, Republic of Korea
[9] INAF – Istituto di Radioastronomia, Via Gobetti 101, 40129 Bologna, Italy
[10] INAF – Osservatorio Astronomico di Brera, Via E. Bianchi 46, 23807 Merate (LC), Italy
[11] Crimean Astrophysical Observatory RAS, P/O Nauchny 298409, Russia
[12] Saint Petersburg State University, 7/9 Universitetskaya nab., St. Petersburg 199034, Russia
[13] Special Astrophysical Observatory, Russian Academy of Sciences, 369167 Nizhnii Arkhyz, Russia
[14] Pulkovo Observatory, St.Petersburg 196140, Russia

Received 12 May 2023 / Accepted 24 October 2023

ABSTRACT

Context. Blazar AO 0235+164, located at a redshift of $z = 0.94$, has undergone several sharp multi-spectral-range flaring episodes over recent decades. In particular, the episodes that peaked in 2008 and 2015, which were subject to extensive multi-wavelength coverage, exhibited an interesting behavior.
Aims. We study the actual origin of these two observed flares by constraining the properties of the observed photo-polarimetric variability as well as of the broadband spectral energy distribution and the observed time-evolution behavior of the source. We use ultra-high-resolution total-flux and polarimetric very-long-baseline interferometry (VLBI) imaging.
Methods. The analysis of VLBI images allowed us to constrain kinematic and geometrical parameters of the 7 mm jet. We used the discrete correlation function to compute the statistical correlation and the delays between emission at different spectral ranges. The multi-epoch modeling of the spectral energy distributions allowed us to propose specific models of the emission; in particular, with the aim to model the unusual spectral features observed in this source in the X-ray region of the spectrum during strong multi spectral-range flares.
Results. We find that these X-ray spectral features can be explained by an emission component originating in a separate particle distribution than the one responsible for the two standard blazar bumps. This is in agreement with the results of our correlation analysis, where we did not find a strong correlation between the X-ray and the remaining spectral ranges. We find that both external Compton-dominated and synchrotron self-Compton-dominated models are able to explain the observed spectral energy distributions. However, the synchrotron self-Compton models are strongly favored by the delays and geometrical parameters inferred from the observations.

Key words. accretion, accretion disks – astroparticle physics – polarization – radiation mechanisms: general – relativistic processes – galaxies: jets

1. Introduction

Blazars are among the most energetic objects in the universe. They are generally believed to consist of a super massive black hole (SMBH), referred to as the central engine, surrounded by an accretion disk and, in most cases, a dusty torus, as well as two symmetrical jets of matter emanating from the innermost vicinity of the black hole and the accretion disk. Particles in the jet are accelerated and collimated through a variety of mechanisms (a subject of numerous research studies currently underway), thereby reaching speeds close to the speed of light. This results in the highly energetic emission of radiation across the entire electromagnetic spectrum when these particles interact with the jet itself, the magnetic fields, and the surrounding medium. In the case of blazars, the jet is pointing towards us, thus bringing on some relativistic effects related to light aberrations. Such effects include light travel-time delays that lead to (apparent) superluminal motions or a Doppler boosting of radiation that makes them appear several orders of magnitude brighter than non-blazar jets.

Blazars usually present a spectral energy distribution (SED) with two bumps: the first extending from the radio to optical wavelengths or even X rays in the case of high

synchrotron-peaked (HSP) blazars; the second extends from X rays, or γ-rays, to very high energy γ-rays. Synchrotron emission from the interaction of the charged relativistic particles of the jet with the magnetic fields in the medium is meant to account for the first bump. Several scenarios exist to explain the second bump. In the leptonic scenario, the second bump is explained by an inverse Compton effect of relativistic electrons interacting with ambient photons. A distinction is made based on whether these photons originate from the synchrotron emission inside the jet, in the case of which the mechanism is labeled as a "synchrotron self-Compton" (SSC). On the other hand, if the photon field is originated in a region external to the jet (typically, the broad line region or the dusty torus), the mechanism is labeled as "external Compton" (EC). There is an ongoing debate underway about the relevance of other different mechanisms, such as so-called "hadronic scenarios". Frequently, combination of more than one emission mechanism is necessary to explain the observed SEDs and variability properties of the sources, even if the exact ratio of their contributions, as well as the origin and location of photon fields and particles involved are not sufficiently well-established.

The study of the variability of blazars across the spectrum, combined with the analysis of sequences of ultra-high-resolution very-long-baseline interferometry (VLBI) images, has proven to be an effective way of constraining the different emission models at work in these objects (Blandford et al. 2019). In particular, knowledge about the exact regions around the supermassive black hole and the relativistic jet where the γ-ray emission originates is essential in terms of discarding or supporting different models.

Regarding the location of the γ-ray emission, two main possibilities have been under discussion, differing with respect to the distance to the central black hole (BH). The first one is the so-called "close-zone" scenario, very close to the BH (0.1−1 pc), which was frequently used to explain the short time scales of high energy (HE) variability. However, this contradicts the coincidence of γ-ray and mm-wave outbursts that are associated to strong superluminal jet features seen in VLBI image sequences much further ($\gg$1 pc) from the BH. In the second one, the so-called "far-zone" scenario, the emission region is located farther from the central engine, but multi-zone jet models are needed to explain the short time scales of variability reported at high- and very-high-energy γ-ray emission.

AO 0235+164 is an extragalactic BLLac-type blazar located at redshift $z = 0.94$ (Cohen et al. 1987). It shows strong variability across all the electromagnetic spectrum and has also displayed an interesting flaring behavior, with the most recent flares occurring in 2008 and 2015 studied with multi-wavelength (MWL) and VLBI. The source typically appears extremely compact at ultra-high-resolution 7 mm VLBI scales (showing the whole of the emission spanning <0.5 mas) and kinematic and geometrical parameters obtained from VLBI images confirm a highly compact, narrow jet geometry pointing closely towards the observer's line of sight with a very small opening angle (<2.4°) at high speed (Doppler factor $\delta > 24$). Altogether, this can explain the violent outbursts reported so far (Jorstad et al. 2001, Weaver et al. 2022). Agudo et al. (2011) reported a detailed analysis of all measurements available up to the 2008 flare, which we extend to 2020 in this paper. Here, we compare the two flaring episodes to shed further light about the origin and mechanisms involved in these extreme flares. The source has also been the subject of several previous observational campaigns that have produced light curves showing flares in previous years, for instance, 1992 and 1998 (see Raiteri et al. 2005). This points to the possibility of certain level of quasi periodicity with a characteristic time scale of about 6 years in the behavior of the source, which can serve as a guidance when developing models of the source, even when the data are not conclusive enough to settle this hypothesis, especially as examples of non-periodic wobbling of blazar jets exist (Agudo et al. 2012).

The 2008 flaring episode has received extensive coverage in the literature. Agudo et al. (2011) analyzed the flare from a multi-wavelength point of view, including the polarimetric data and VLBI imaging of the source. Their results favored a SSC scenario over EC to explain the γ-ray emission and constrained the location of the emitting region at >12 pc from the central engine. Ackermann (2012) also analyzed the 2008 flare and produced a fit for the SED in the peak of the flare. In their model, EC was the dominating emission mechanism in the γ-rays. However, the EC mechanism fails to explain the observed variability and the correlations between γ-ray and optical emission. Baring et al. (2017) managed to reproduce the SED of AO0235+164 during the peak, including the X-ray excess. Wang & Jiang (2020) concluded in their study that the γ-ray and mm-wave emitting zones coincided within the acceptable errors and were located several parsecs from the central engine. These authors proposed a helical model for the jet to explain the observed polarization, without discarding other possibilities such as the shock-in-jet scenario. For this work, we have used a standard flat ΛCDM cosmological model with Hubble constant $H_0 = 67.66\,\mathrm{km\,Mpc^{-1}}$, as given by Planck Collaboration VI (2020).

2. Observations

We have obtained and compiled time-dependent data in most available ranges of the electromagnetic spectrum, including polarimetry whenever possible and VLBI polarimetric images with submilliarcsecond resolution.

Our observations include 7 mm Very Long Baseline Array (VLBA) images from the blazar monitoring program at Boston University, which were reduced both for total flux and polarization using `AIPS` (see Weaver et al. 2022 for details on the data reduction and calibration). Single-dish data at 1 mm and 3 mm were obtained from the POLAMI (Polarimetric Monitoring of AGN at Millimeter Wavelengths)[1] program at the IRAM 30 m Telescope (Agudo et al. 2017a,b Thum et al. 2017). The optical (R-band) data were taken from Calar Alto (2.2 m Telescope) under the MAPCAT program, Yale University SMARTS blazar program, Maria Mitchell, Abastumani and Campo Imperatore observatories, Steward Observatory (2.3 and 1.54 m Telescopes), Perkins Telescope Observatory (1.8 m Telescope), Crimea Observatory AZT-8 (0.7 m Telescope), and the St. Petersburg State University LX-200 (0.4 m Telescope).

Ultraviolet (UV) measurements were obtained by the *Swift*-UVOT instrument. The data set also includes X-ray data in the 2.4–10 keV range from the RXTE satellite and in the 0.2–10 keV energy range from *Swift*-XRT. The light curves and spectral indices were derived from these data using a broken power-law model and the appropriate corrections for extinction. More details on the data reduction procedure from *Swift* is provided in Appendix B. The γ-ray data in the 0.1–200 GeV range come from the *Fermi* Large Area Telescope (LAT).

[1] https://polami.iaa.es

The ±180° polarization angle ambiguity in our *R*-band measurements was circumvented following the procedure described in Blinov & Pavlidou (2019), which minimizes the difference between successive measurements taking also into account their uncertainty. Clusters of close observations were then shifted by an integer multiple of 180° to match the angle reported at 3 mm. This allows us for a visual comparison of the joint evolution of the optical and millimeter range polarization angles.

Data from the infrared (IR) to the *UV* bands were corrected following the prescription by Raiteri et al. (2005) and the updated values by Ackermann (2012). This correction accounts for the local galactic extinction at $z = 0$ and the intervening galaxy ELISA at $z = 0.524$, as well as for ELISA's contribution to the observed emission. When these corrections are applied, a UV bump appears in the final spectra for some epochs; this was shown in Raiteri et al. (2005), although the results are in disagreement with the SEDs presented in Ackermann (2012). It must be noted that applying different correction factors available (NED[2], Junkkarinen et al. 2004, etc.) also produce bumps (albeit of different intensity) but the UV bump is present in every case. Here we have followed Raiteri et al. (2005) when producing the final, extinction-corrected SEDs and used the updated values in Ackermann (2012) for the extinction factors, together with the magnitudes for ELISA reported by Raiteri. A comparison with the older values by Junkkarinen et al. (2004) can be seen in Fig. 15.

The correction of X-ray spectral data was performed using a single absorbed power law with density $N_{\rm H} = 2.8 \times 10^{21}$ cm^{-2} (Madejski et al. 1996; Ackermann 2012), which accounts both for galactic extinction and the $z = 0.524$ absorber. This value agrees with the result obtained when letting $N_{\rm H}$ vary as a free parameter.

3. Results

3.1. Millimeter, optical, and high energies

The light curves at millimeter wavelengths (VLBA 7 mm, 1 mm, 3 mm), optical bands (*R*, *U*, *B*, *V*), *UV* bands (*UVW*1, *UVW*2, *UVM*2), X-rays (0.2–10 keV), and γ-rays (0.1–200 GeV) of AO 0235+164 are presented in Fig. 1. Polarization degree and polarization angles at optical (*R*-band) and millimeter wavelengths (1 mm, 3 mm, and VLBA 7 mm) are shown in Figs. 2 and 3, respectively. Figure 1 shows that flaring episodes happen almost simultaneously across all the electromagnetic spectrum. Variability is much more pronounced at HE, while it is milder at optical and UV wavelengths and even more so in the millimeter and radio bands.

3.2. Polarization

The Bayesian block representation (Scargle et al. 2013) of the polarization degree light curves makes it easier to discern the different behavior between quiescent and flaring states (Fig. 2) because it represents significantly different evolution states of the source. The source exhibits lower polarization degree at both optical and mm wavelengths during the quiescent period in between flares ($p_{L,R} = 9.5 \pm 6.0\%$, $p_{L,3\rm mm} = 2.5 \pm 1.4\,\%$ from 2010 to 2014) than during flares ($p_{L,R} = 14.5 \pm 8.5\%$, $p_{L,3\rm mm} = 3.34 \pm 1.3\%$ from 2014 to 2017). The 3 mm polarization angles also varies more slowly during the quiescent period: from 2010 to 2014, the polarization angle at mm wavelengths remains more or less stable, while from 2014 to 2017, it performs three full 180° rotations (as seen in Fig. 3). Rotations in the optical *R*-band also follow mm rotations, with a stronger variability, sometimes performing several 180° cycles while the 3 mm only varies a full cycle or a partial rotation. There is also an apparent delay of approximately a hundred days between 3 mm and *R*-band, as can be seen in Fig. 3.

The direction of the electric vector position angle (EVPA) of the VLBA components (indicated in Figs. 4–6 as black lines segments overlaid with the images) coincides with the momentary direction of the jet. This alignment is in agreement with the shock-in-jet model (Marscher et al. 2008), where the compression of the magnetic field in the plane perpendicular to the direction of propagation (slightly askew of the direction of the observer) makes the electric field align with the jet direction. This supports the association of the superluminal components ejected during flares with plane-perpendicular moving shock-waves.

3.3. VLBI imaging

Our study includes all available 7 mm (43 GHz) VLBA total flux and polarimetric images from the Boston University Blazar Group of the sourced from 2008 to 2020 (from the VLBA-BU-BLAZAR and BEAM-ME programs[3]). After reducing the data with `AIPS` (see Weaver et al. 2022), the most prominent jet features were fitted to Gaussian components with `Difmap` and then cross-identified along the observing epochs. This was done for a total of 142 observing epochs.

The VLBA images show a compact, stationary component at all epochs, A0, referred to here as the "core". Other features can be tracked at different epochs and their evolution is traced over time. Figure 4 shows some selected epochs with the identified knot features to give a general idea of the behavior of the source in time. Evolution curves in total and polarized flux intensity and the polarization degree for the total emission and single components were later produced from the images (Figs. 1–3) using the aforementioned identification.

The flux evolution shown in Fig. 1 at all wavelengths, also containing the light curves from the integrated VLBA 7 mm maps, allows us to distinguish two clear "flaring" periods, whose peaks of activity occurred in October 2008 and July 2015, respectively. The 2008 flare is associated with the B2 jet feature that developed southwest of the core (A0). In contrast, the 2015 flare is associated with jet components B5 and B6 that developed northwest. Other weaker components not associated with the main outbursts (e.g., B4), also propagate in different directions. This hints at a possible rotation or wobbling of the jet and supports a helical jet model, and might be associated to a pseudo periodic behavior as proposed by Raiteri et al. (2005). All VLBI jet components have lifetimes lasting several years. During their lifetimes, we observe them propagating quasi-ballistically in the same direction relative to the core, with trailing components maintaining the same direction of propagation as their leading component as well as for its EVPA alignment (parallel to the direction of propagation in the plane of the sky). It is therefore clear that jet nozzle changes direction with time since, in each flaring episode, the direction of propagation of the associated superluminal components is radically different for every on of these episodes.

[2] The NASA/IPAC Extragalactic Database (NED) is operated by the Jet Propulsion Laboratory, California Institute of Technology, under contract with the National Aeronautics and Space Administration: https://ned.ipac.caltech.edu

[3] https://www.bu.edu/blazars/BEAM-ME.html

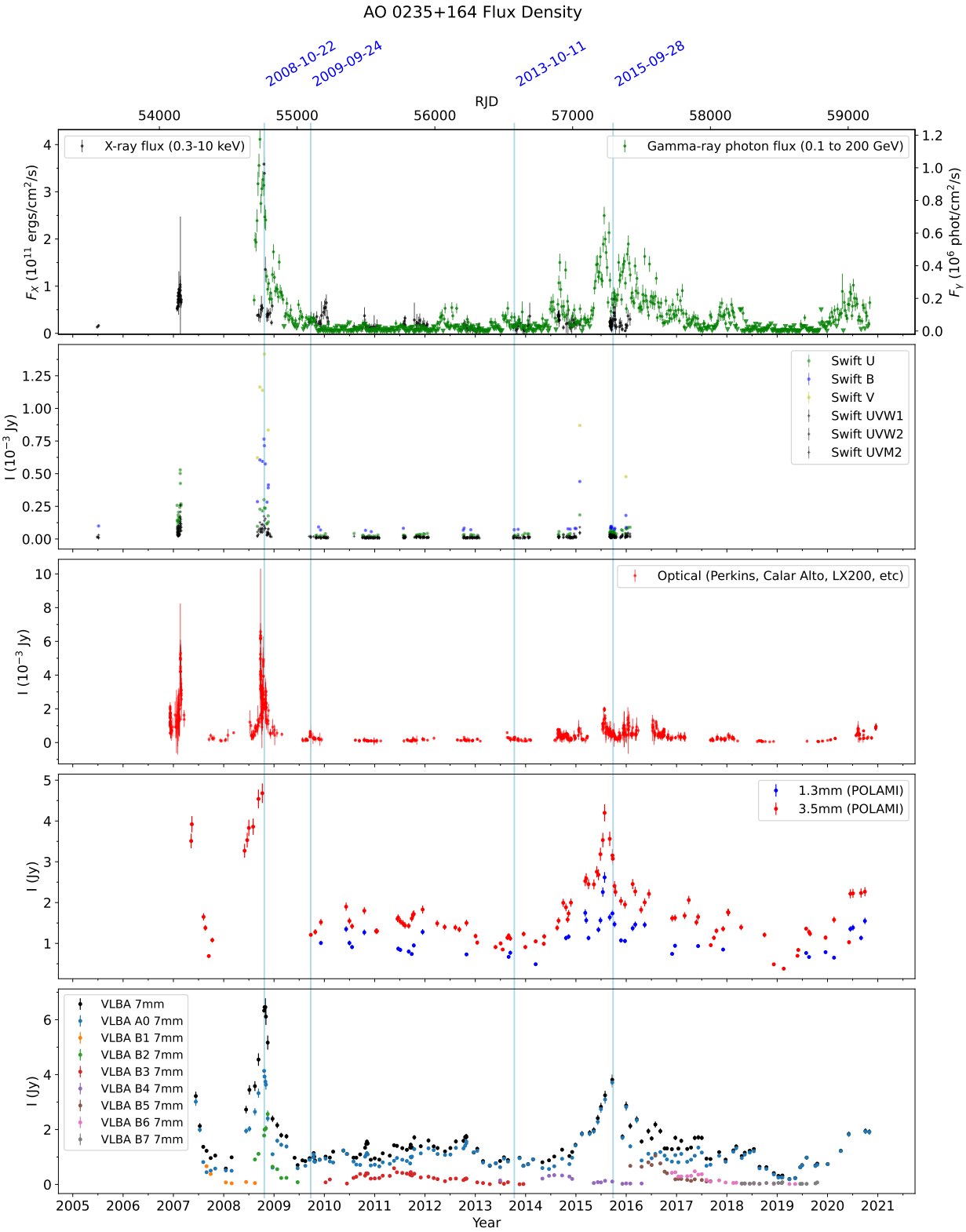

Fig. 1. Light curves of AO 0235+164 at different wavelengths. The vertical lines mark the epochs whose SEDs were analyzed in Sect. 4.4. The top panel shows both the X-ray and γ-ray fluxes in different axes (left for X-rays and right for γ-rays, respectively).

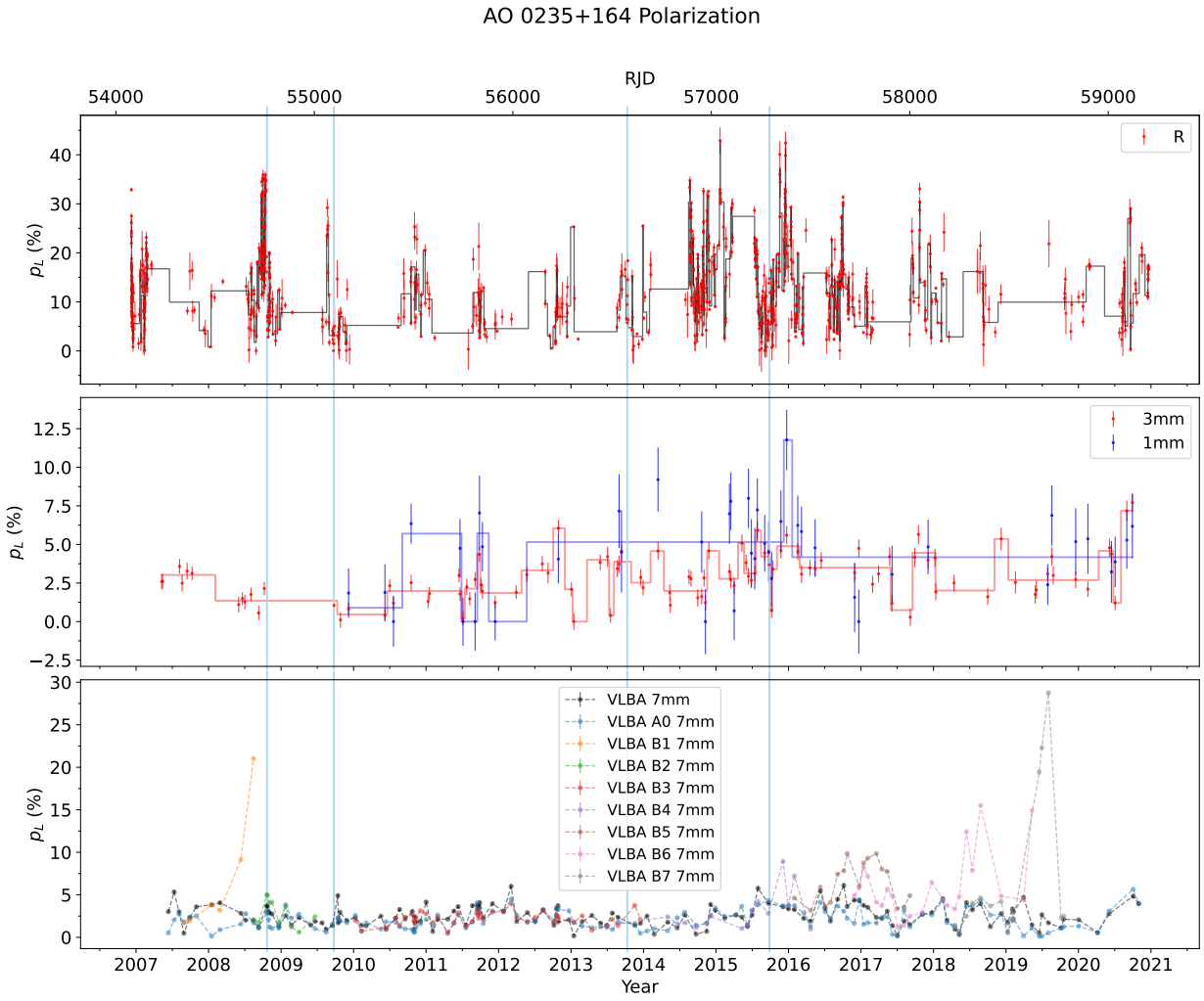

Fig. 2. Polarization degree evolution of AO 0235+164 at different wavelengths. Together with experimental data, a bayesian block representation is shown superimposed for *R* (black line) at a 99.9% confidence and for 1 mm (red) and 3 mm (blue) at a 90% confidence level. The vertical lines are the same as in Fig. 1 and correspond to the epochs whose SED was analyzed in Sect. 4.4.

3.4. Differences and similarities between 2008 and 2015 flares

The flare in 2008, reported by Agudo et al. (2011), featured a superluminal component ejected from the core during June 2008, which kept separating from the core in the southeast direction during the following months, until the last months of 2009, when the component went practically extinct. Agudo et al. also reported correlations between all wavelengths, from radio to γ-rays. The flare in 2008 reached a maximum in October 2008, peaking at 4.7 Jy in 3 mm and a magnitude of 14.2, having increased its brightness by more than a factor of 60 in optical *R* band with respect to its quiescent state. Although a general correlation was reported between optical and γ-ray bands, the correlation was poorer and less detailed during the main burst.

The second flaring activity begins approximately in autumn 2014, with a brightening of the core visible at 7 mm. The flux densities at all wavelength peak a year later, around autumn 2015, at all wavelengths. Comparatively, this flare is dimmer than the previous one of 2008, reaching 4.2 Jy in 3 mm and lower by 1.3 in magnitude in the optical *R* band. A plausible explanation for this will be given below through the interpretation of the flare in terms of emission zones and shocks.

The VLBI images reveal that the component responsible for the brightening of the core during the 2015 flare, named B5, originates in the core less than a few weeks before the brightening in total flux density begins. After it separates from the core, the component travels outwards at a position angle of ∼45° while increasing its brightness, and peaks around Fall 2016. Figure 5 shows the total and polarized intensity image of the source during nearest to this event. This is around a year later than the total flux peak. The interpretation for this is that the initial brightening of the total flux is due to the interaction of the component with the core, while the ensuing brightening of the component is due to acceleration or a change in the viewing angle.

A few months later another, a weaker component, named B6, originated from the core. This component follows the path of B5, peaking around April 2017 (Fig. 6), while B5 is still visible. This component is the one responsible for the subflare of 2017, visible

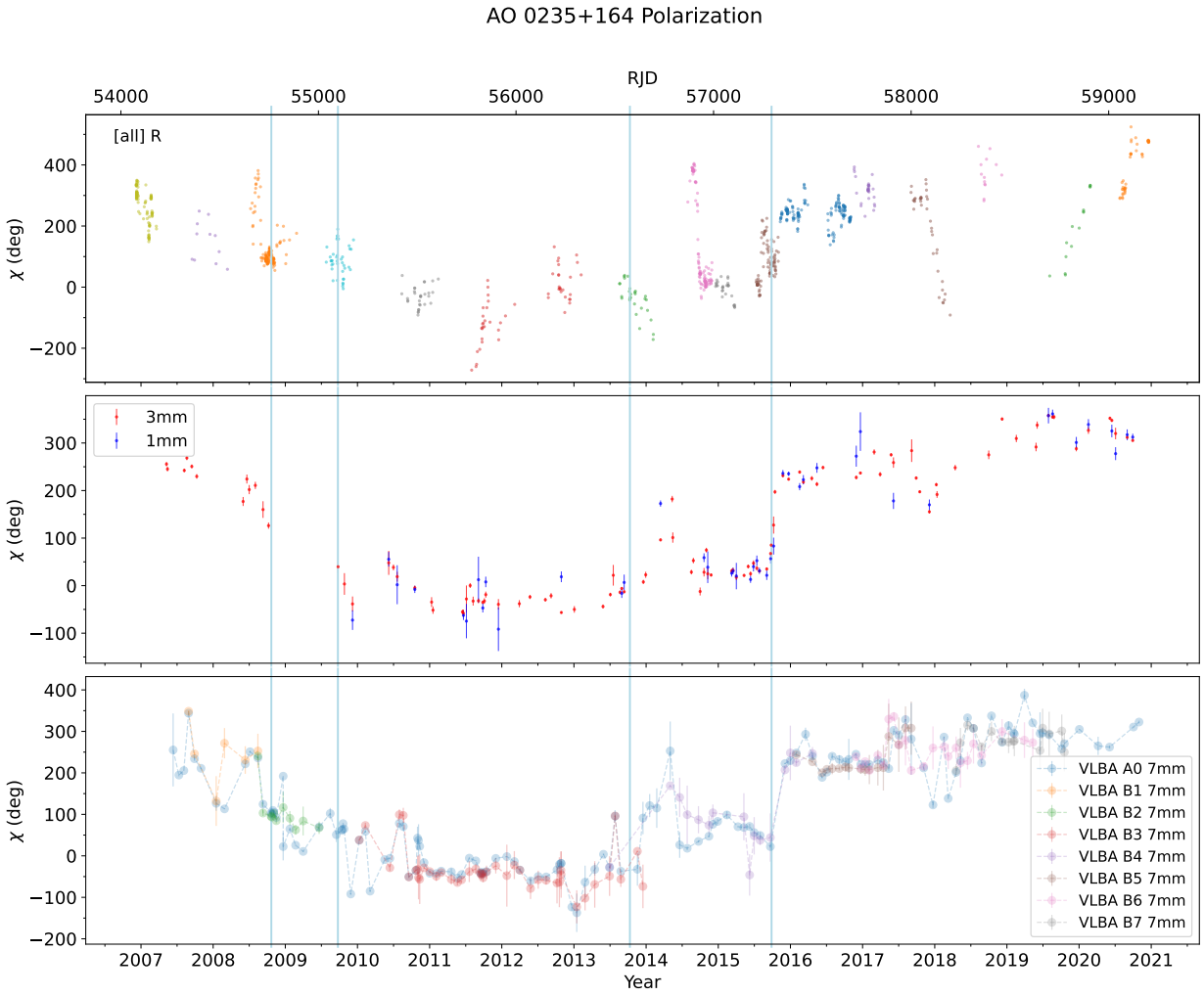

Fig. 3. Polarization angle evolution of AO 0235+164 at different wavelengths. The vertical lines are the same as in Fig. 1 and correspond to the epochs whose SEDs were analyzed in Sect. 4.4. All points in the first box correspond to *R* band, the colors denote the clusters that were shifted by $n \times 180°$, as noted in Sect. 3.2.

at all wavelengths in total flux. The behavior of this component is compatible with that of a trailing component of B5 as described by Agudo et al. (2001). By 2019, all activity had ended, with a minimum reached around March 2019.

The two flares present different time profiles at γ-ray energies. A comparison of these profiles can be found in Fig. 7, where also the 7mm flux of each identified VLBI component is shown. We have modeled the γ-ray profiles by fitting to standard exponential shapes given by (Abdo et al. 2010)

$$y(t)_{N_{\rm exp}} = \sum_{i}^{N_{\rm exp}} A_i \cdot \left(e^{(t-t_{ci})/t_{ri}} + e^{(t-t_{ci})/t_{di}}\right)^{-1}, \quad (1)$$

which allowed us to derive the rising and decaying times of each subflare, t_{ri} and t_{di}. Then, their asymmetry factor could be computed, defined as:

$$\xi_i = \frac{t_{ri} - t_{di}}{t_{ri} + t_{di}}. \quad (2)$$

An asymmetry factor close to zero corresponds to the case of a perfectly symmetric flare. There is some uncertainty in the number of exponential terms to use, since the source shows strong variability in timescales shorter than our binning allows us to track. The wide binning applied, (i.e., 7 days) was necessary to accommodate periods of low flux. Still, it can be seen that the source displays significant variations of flux even in these intervals. The value of $N_{\rm exp}$ chosen was the one that minimized the reduced χ^2-statistic. The results of both fits are shown in Fig. 7, and the corresponding parameters in Tables 1 and 2. The distance from the fitted γ-ray subflare maximum to the 7mm maximum in 2015 is 52 days (±8 days), a similar delay to the one found in the DCF analysis in Sect. 4.2 ($\tau_{R,\gamma}$ = 2 days, $\tau_{R,7\rm mm}$ = (64 ± 4) days).

For the 2015 flaring episode, the secondary flares in γ-rays are contemporaneous with the appearance of 7mm VLBI components. In particular, the first, second and third maxima happen at approximately the same time A0 rebrightens and the B5 and B6 components appear. This suggests that these emissions are spatially related.The failure in finding components responsible

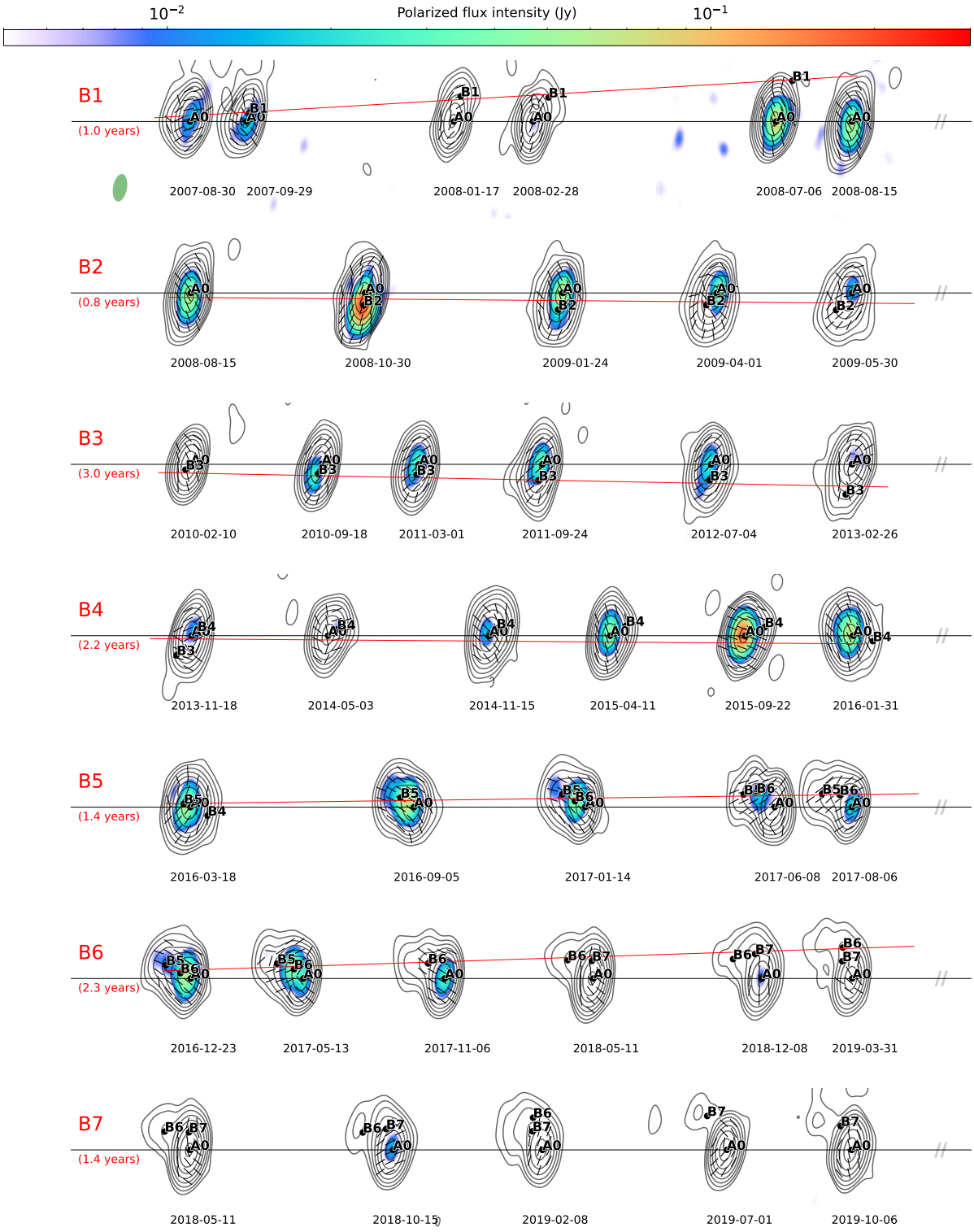

Fig. 4. Selected epochs illustrating the evolution of each identified knot, showing total (contours) and polarized (color scale) intensity. The beam size is indicated as a green ellipse in the first row. Horizontal black lines indicate the position of the core A0, black line segments within the image indicate the direction of polarization (EVPA). The red line in each row is the linear fit to the knot position. It is present for every knot except B7, whose flux was too low to accurately perform a fit. For each row, the spacing between plots is proportional to time, and the total time span is different and indicated in brackets.

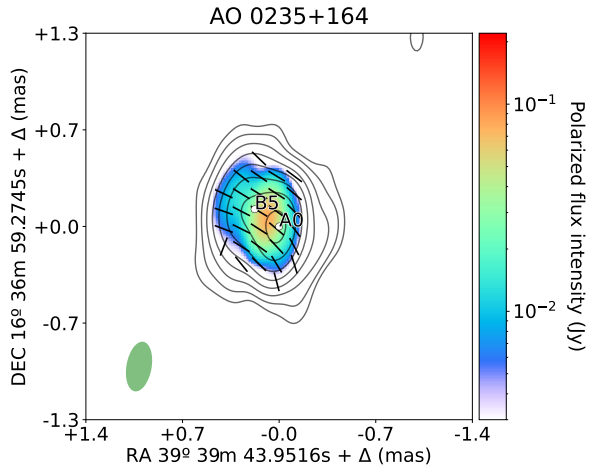

Fig. 5. Epoch 102 (2016-09-05) VLBI 7 mm image, showing total flux intensity (contours) and polarized flux intensity (color scale). Black line segments overlaid in the image represent the EVPA. The green ellipse in the lower left corner represents the beam size. The image showcases component B5 close to the peak of the 2015 flaring episode, demonstrating how the polarization angle is aligned with the direction of propagation.

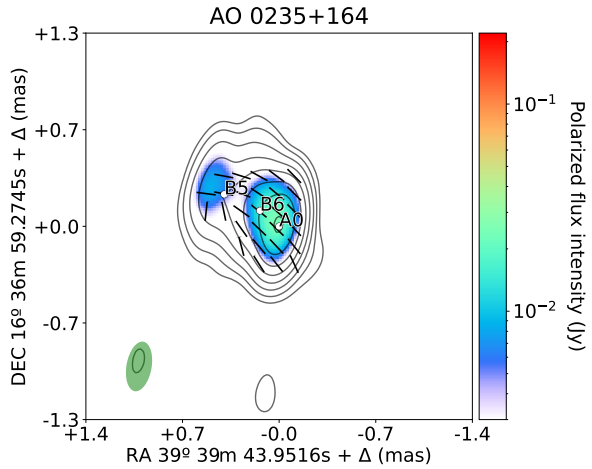

Fig. 6. Epoch 110 (2017-04-16) VLBI 7 mm image. The image shows the trailing component B6 moving in the same direction of B5, maintaining the alignment of the polarization angle (black line segments) with the momentary direction of the jet (northeast).

for the subsequent fitted subflares might be due to the difficulty in fitting low-flux VLBI components, the uncertainty in the γ-ray light curve, or a combination of both.

The same can be said about the first and second subflares of the 2008 flaring episode, where it seems that the brightening of the core A0 and the appearance of the B2 component are related to the first and second maximums at γ-rays, taking into account the aforementioned delay.

The γ-ray subflare that can be seen in Fig. 8 occurring one year before the start of the 2014 flaring episode might be related to the B4 component in the same way, but this relation and the associated delay are less clear. This could potentially be the case also with the B1 component and the flare that can be seen in

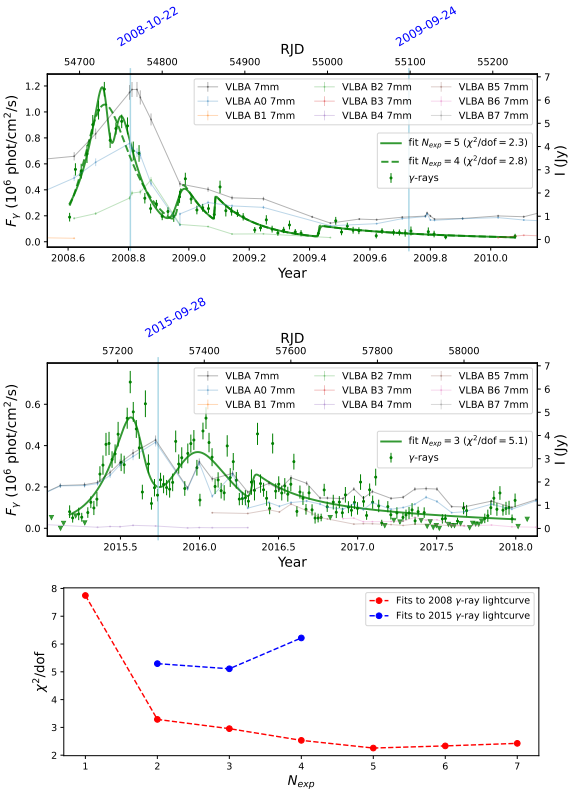

Fig. 7. Fits to the profiles of the 2008 (top) and the 2005 (middle) γ-ray flares by exponential functions as described by Eq. (1). The selected number of terms $N_{\rm exp}$ were chosen so that the reduced χ^2-statistic was minimized (bottom). The best-fit values are given in Tables 1 and 2. An alternative fit is given for the 2008 flare with a similar χ^2, that accounts for the double peak at the beginning with a single exponential term. The vertical lines mark the epochs whose SED was analyzed in Sect. 4.4, as in Fig. 1.

2006 (before the 2008 episode) in all wavelengths except γ-ray (due to the lack of observational data). Altogether, it seems that there is a direct relationship between the appearance of the 7 mm VLBI components and the successive γ-ray subflares.

For the 2015 flaring episode, the rising and decaying times shown in Table 2, which are as low as ~18 days (taking into account only the two strongest subflares), are compatible with the sizes found in the SED modeling of Sect. 4.4 (Table 7), which sets the shortest timescale where significant variations of flux can occur at a limit of 15 days (see Eq. (8)). These other values were obtained only from the modeling of the SEDs and the two analyses are completely independent. In the case of the 2008 flaring episode, however, the shorter times (~4 days) reveal some tension with the region sizes. This might be explained by unaccounted sources of γ-ray variability originating in smaller regions. However, it could also be caused by a wrong estimation of the rising and decaying times. It is possible to produce a fit with a single term accounting for the initial double peak that has a similar χ^2-square statistic, but rising and decaying times of 18 and 36 days (dashed line in Fig. 7). In any case, the observed delays between γ and mm might be explained by a combination of adiabatic expansion and cooling times (Tramacere et al. 2022).

Table 1. Parameters for the fit to the γ-ray light curve of the 2008 flaring episode to functions of shape given by Eq. (1).

$N_{\rm exp}$	A_i ($\times 10^6$)	t_{ri} [days]	t_{di} [days]	t_{ci} [year]	χ^2/d.o.f.	ξ
4	2.0 (0.1)	17.8 (4.3)	36.4 (3.2)	2008.698 (0.014)	2.8	−0.3
	0.4 (0.1)	<2.6	37.8 (20)	2008.968 (0.006)		−0.9
	0.2 (...)	<26	...	2009.085 (...)		−1.0
	0.09 (...)	<200	...	2009.430 (...)		−1.0
5	1.7 (0.4)	25.7 (2.1)	<4.4	2008.728 (0.008)	2.3	0.7
	1.5 (0.4)	5.3 (5.0)	27.9 (4.7)	2008.758 (0.007)		−0.7
	0.5 (0.1)	4.6 (2.9)	37.7 (21)	2008.965 (0.012)		−0.8
	0.2 (4×10^3)	<17.2	...	2009.086 (...)		−1.0
	0.09 (4×10^1)	<290	...	2009.432 (44)		−1.0

Notes. The resulting reduced χ^2-statistic for the fit is shown, and also the computed symmetry factor ξ_i for each subflare. Some values could not be computed. Upper limits are indicated with '<'. The result can be seen in Fig. 7.

Table 2. Parameters for the fit to the γ-ray light curve of the 2015 flaring episode.

$N_{\rm exp}$	A_i ($\times 10^6$)	t_{ri} [days]	t_{di} [days]	t_{ci} [year]	χ^2/d.o.f.	ξ
3	0.9 (0.2)	58 (12)	18.2 (7.7)	2015.605 (0.022)	5.1	0.5
	0.7 (0.1)	49 (35)	86 (48)	2015.941 (0.122)		−0.3
	0.15 (0.07)	3.2 (6.4)	490 (340)	2016.332 (0.018)		−1.0

Notes. The resulting reduced χ^2-statistic for the fit is shown, and also the computed symmetry factor ξ_i for each subflare. The result can be seen in Fig. 7.

4. Analysis

4.1. Kinematic parameters of the VLBI jet components

From the VLBI imaging data, some kinematics parameters associated to the different visible emission zones were computed following the procedure described in Weaver et al. (2022). These include t_0, the ejection time, which is the time where the extrapolated trajectory of the component crosses the core; $t_{\rm var}$, the timescale of variability, which is the timescale of the dimming of the component; $\beta_{\rm app}$, the apparent speed in units of c; $\delta_{\rm var}$, the variability Doppler factor; Γ, the Lorentz factor; and Θ, the viewing angle of the jet component.

The identified knot features in every epoch were traced and their positions adjusted to a linear fit, from which their speeds were obtained and their flux was also fitted to a decaying exponential function of $F = F_0 \exp(-t/t_{\rm var})$, obtaining a timescale of variability (Fig. 9).

The Doppler factor and apparent speed were then computed as (Jorstad et al. 2005, Casadio et al. 2015):

$$\delta_{\rm var} = \frac{1.6\, a_{S_{\rm max}}\, d_L}{c t_{\rm var}(1+z)}, \tag{3}$$

$$\beta_{\rm app} = \frac{v_r d_L}{c(1+z)}, \tag{4}$$

where $a_{S_{\rm max}}$ is the FWHM of the component measured at its maximum flux, v_r is the radial velocity of the knot, and d_L is the luminosity distance, but following the more robust approach found in Weaver et al. (2022) and using the value of $t_{\rm var}$ obtained from the fit. From these, the Lorentz bulk factor,

$$\Gamma = \frac{1}{2\delta_{\rm var}}\left(\beta_{\rm app}^2 + \delta_{\rm var}^2 + 1\right), \tag{5}$$

and the viewing angle,

$$\tan\Theta = \frac{2\beta_{\rm app}}{\beta_{\rm app}^2 + \delta_{\rm var}^2 - 1}, \tag{6}$$

can be computed.

Our results for these parameters (Table 3) agree with those of Weaver et al. (2022) within the expected margin of error associated with the identification of the components in the VLBA images.

The results agree with the observed behavior of the flares. The estimated viewing angle for the component responsible for the 2008 flare (B2) is 0.2°, between three and four times smaller than the 0.7° of the component responsible for the 2015 flare (i.e., B5). This consistently explains the lower brightness observed in 2015 as being caused by a weaker Doppler boosting of the emission. The viewing angle for the secondary component B6 is similar to the one of B2; however, it is also apparent that its speed is much lower than for any of the others.

4.2. Correlations across the spectrum

Correlations among the different light curves were computed using `MUTIS`[4]. In particular, since we are dealing with irregularly sampled signals (light curves), we computed the discrete correlation function (DCF) following the method from Welsh (1999), which is a normalized and binned DCF.

A uniform bin size of 20 days was used for all correlations. The choice of a uniform bin size was done so that the results of different correlations could be easily compared, the specific value of 20 days was done so that it was large enough to have statistics in any bin, but short enough that the correlations were not overly smoothed and peak positions could still be determined. To confirm the robustness of our choice, we also

[4] MUltiwavelength TIme Series. A Python package for the analysis of correlations of light curves and their statistical significance. https://github.com/IAA-CSIC/MUTIS

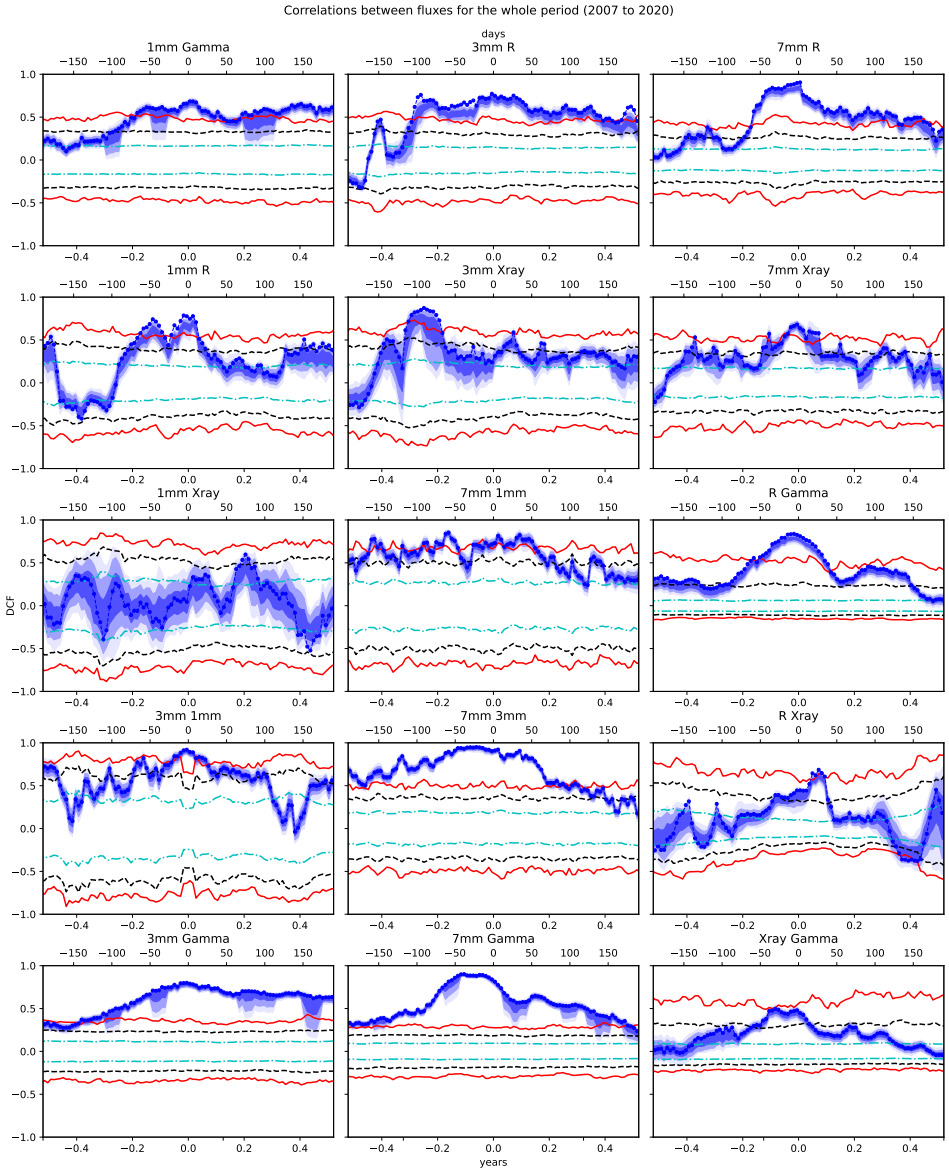

Fig. 8. Correlations between fluxes across all wavelengths. Horizontal lines show significance levels for 1σ, 2σ, and 3σ, computed using $N = 2000$ synthetic light curves, as described in Sect. 4.2. The DCFs here are computed using the whole period of available data, from 2007 to 2020.

Table 3. Kinematics parameters for identified knots of 0235+164 ($[v_r]$ = mas year^{-1}, $\langle a \rangle$ = mas, $t_{\rm var}$ = year, $[\Theta] = ^\circ$, other units are dimensionless).

Component	v_r	σ_{v_r}	t_0	σ_{t_0}	$\langle a \rangle$	σ_a	$t_{\rm var}$	$\sigma_{t_{\rm var}}$	$\delta_{\rm var}$	$\sigma_{\delta_{\rm var}}$	$\beta_{\rm app}$	$\sigma_{\beta_{\rm app}}$	Γ	σ_Γ	Θ	σ_Θ
B1	0.57	0.05	2007.52	0.09	0.29	0.02	0.32	0.02	70.5	5.4	28.28	2.55	40.9	6.3	0.56	0.06
B2	0.18	0.02	2007.98	0.12	0.16	0.01	0.19	0.00	67.8	3.6	9.14	1.09	34.5	4.0	0.22	0.03
B3	0.05	0.01	2008.06	0.11	0.17	0.01	0.82	0.01	16.8	1.0	2.61	0.29	8.6	1.1	1.04	0.12
B4	0.07	0.01	2012.42	0.21	0.15	0.01	0.60	0.02	20.3	1.7	3.40	0.73	10.5	1.9	0.92	0.20
B5	0.21	0.02	2015.61	0.09	0.24	0.01	0.47	0.01	39.8	2.2	10.57	0.94	21.3	2.5	0.71	0.07
B6	0.16	0.04	2016.08	0.22	0.28	0.01	0.35	0.02	63.5	5.4	7.87	1.76	32.3	6.0	0.22	0.05

reproduced our analysis with bin-sizes from 10 to 30 days, obtaining similar results; with the exception of some bins that did not have enough points to compute the correlation, as we discarded bins where the number of pairs was less than 11.

To estimate the significance of the correlations, a Monte Carlo approach was used, generating N=2000 synthetic light curves for each signal. The randomization of the Fourier transform was used for mm-wavelengths, while for the optical

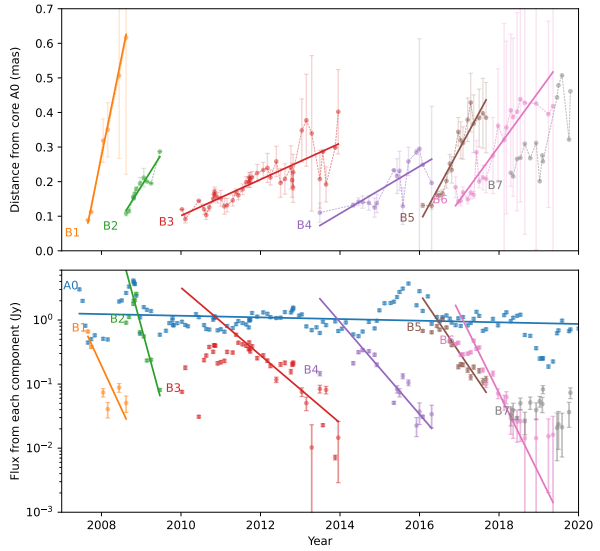

Fig. 9. Observed distance from core (top) and flux density (bottom) for every one of the identified component as a function of time, together with a linear weighted fit to knot distance and logarithmic fit to flux. The fit to the flux is done taking into account only the points after the peak of emission of each component. This was done for all components except B7, which due to its low flux, did not have enough points after the peak with low enough uncertainty to perform a fit.

and γ-ray data, we modeled the signals as Orstein-Uhlenbeck stochastic processes (Tavecchio et al. 2020). The uncertainties of the correlations were estimated using the uncertainties of the signals again with a Monte Carlo approach.

4.2.1. Correlation of the whole period (2007–2020)

The results from DCFs of the whole available period of data (2007–2020) show a clear correlation between the flux at almost all wavelengths ($>3\sigma$) with most peak positions close to zero (Fig. 8). The X-ray band is an exception to this, showing no significant ($>3\sigma$) correlation close to zero with some of the other bands. More hints about this will be provided in the following.

The correlation between the polarization degree and total flux is clear for the R band, where it shows a statistically significant maximum near zero, but it is not certain in the other bands. This may possibly be explained by the sparser sampling and larger errors (Fig. 10).

4.2.2. Correlations of flaring episode (2014 and 2017)

The results from DCFs of the flaring episode (2014 to 2020) again show significant ($>3\sigma$) correlation between flux at all wavelengths, with most peaks positions close to zero (Fig. 11). The clear exception to this general correlation is again the X-ray band. The absence of $>3\sigma$ correlation close to zero for the X-ray emission with the other bands (Fig. 11) hints at other emission mechanisms located in a different emission zone. This suggests that a different, separated processes could be responsible (at least partially) for the emission in the X-ray. This hypothesis was also favored by the analysis of the spectral energy distribution of the source (Sect. 4.4).

The interpretation of the peak positions in the DCFs is not straightforward. A debate on how accurately they represent the timing between different emission episodes is ongoing. This is especially the case when longer periods are taken into account, as a greater number of different processes and regions can be involved in the correlation. For the DCF of the whole period, the correlation only tells us about the probability that the processes causing the emissions are related. However, if we consider only the flaring episode, the relation between the peak position and timing of emissions will be more direct. Even then, the presence of several correlation peaks makes the interpretation of the results difficult. These peaks are the consequence of the low, non-uniform sampling of available data, and the complex structure of the flares. This is a fundamental flaw of any correlation analysis, since this correlation noise might result in peaks that do not correspond to the real delay between the signals. Several ways of dealing with these have been proposed, such as using the centroid instead of the maximum, but they are not free from biases and flaws, such as those discussed in Welsh (1999). Here, we follow Welsh (1999), using just the absolute maximum of the DCF and justifying the decision with the consistency of our results, as shown in the following.

If the position of the peak is to represent the real delay between the signals at different wavelengths, these delays should be more or less compatible between themselves when computed using different sets of correlations, for instance, the delay between A and B plus the delay between B and C should be close to the delay between A and C. In this sense, it is possible to build a compatibility chart, showing the relations between the different positions.

This is shown in Fig. 12 (Table 4) with the DCFs computed for the signals between 2014 and 2017 (the flare period, Fig. 11) and the band R as a reference. Our choice of R as the reference band is motivated by the fact that is the most densely sampled band during the periods of high variability. In this graph, each row corresponds to a band, i. The delays or peak positions between the row band i and any other band j, $\tau_{\rm p}^{i,j}$, are plotted along the x-axis, shifted by the delay between the band, i, and the reference band, $\tau_{\rm p}^{i,R}$, so that they fall aligned on the same positions.

We see that indeed the positions fall more or less aligned in most cases, justifying our interpretation, and our choice of the maximum. The points for 1 mm and γ are very dispersed, but the correlation between R and γ presents a prominent peak, with high confidence and without spurious peaks close (Fig. 11), so we take $\tau_{\rm p}^{R,\gamma} \sim +2$ days as the correct delay, $\tau_{\rm R,\gamma}$.

Discarding the 1 mm and γ rows, we estimated that the mean delays with respect to R for 7 mm, 3 mm, and X-ray, $\tau_{i,R} = \langle \tau_{\rm p}^{i,R} \rangle$ are 64 ± 4 days, 42 ± 6 days, and 73 ± 4 days, respectively. The delays for 7 mm, 3 mm, and R are consistent with expectations if the mechanism of emission is synchrotron cooling, which should result in delays of the form $\tau_s \propto \nu_s^{-1/2}$, where ν_s is the synchrotron frequency, as can be seen in Fig. 13.

The delay obtained for X-ray with respect to R is much larger than for any other band. This strengthens the hypothesis that emission at X-ray energies might involve a different mechanism, as is already suggested by the lower level of correlation found and as the analysis of the spectral energy distributions revealed (see Sect. 4.4).

4.3. Geometry of the emission regions

We can also compute the corresponding sizes implied by the variability timescales, since they are constrained due to causality

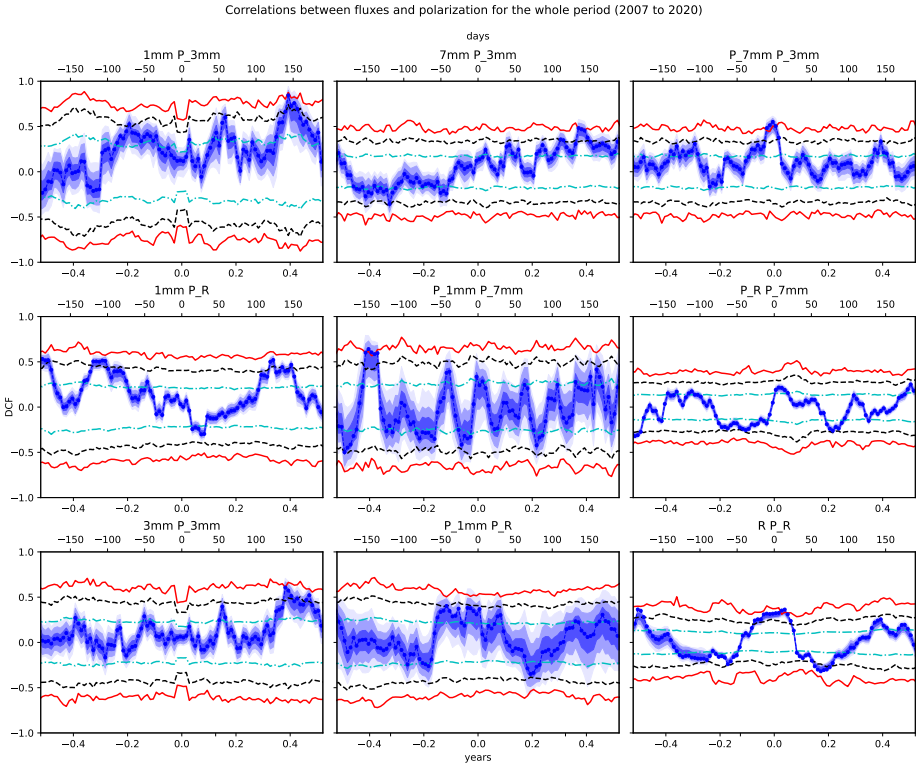

Fig. 10. Correlations between fluxes and polarization degree across all wavelengths. Horizontal lines show significance levels for 1σ, 2σ, and 3σ, computed using $N = 2000$ synthetic light curves, as described in Sect. 4.2. The DCFs here are computed using the whole period of available data, from 2007 to 2020.

and special relativity, according to the following formula:

$$d = \frac{c\beta\Delta t}{(1-\beta\cos\theta)(1+z)} = \frac{\beta_{\rm app} c\Delta t}{(1+z)\sin\theta}. \quad (7)$$

This same formula can also be used to compute the relative distances between emission regions implied by the time delays obtained in the correlation analysis, under the hypothesis that they result from the distances (although this may not necessarily be the case if they arise from synchrotron cooling, as shown in the previous section).

The sizes of the emitting region can be constrained with:

$$R_b = \frac{ct_{\rm var}\delta_D}{1+z}. \quad (8)$$

For the moving component B2 corresponding to the 2008 outburst, using the timescale of variability in Table 3 and the $\delta_D \simeq 67$, we obtain sizes of around 2 pc, consistent with the angular measure of VLBI images. Using the γ-ray variability one obtains much lower sizes, of around 0.2 pc, since variability at these energies is observed in timescales as short as 8 days (Ackermann 2012). This smaller high-energy emitting region is in agreement with the expected result of synchrotron cooling in the proposed model which explains the longer duration of flaring activity in mm. The maximum viewing angle of this jet is cited to be $\lesssim 2.4^\circ$ (Agudo et al. 2011). Via the relations between this angle and the true speed and Doppler factor, namely,

$$\beta = \sqrt{1-1/\Gamma^2}, \quad (9)$$

$$\mu_s = \frac{1}{\beta}\left(1-\frac{1}{\Gamma\delta_D}\right) = \cos\Theta, \quad (10)$$

and Eq. (8) limits us to a minimum of 1 pc the sizes of the mm-emitting regions.

The relative distances of the core and knots to the base of the jet can be ascertained using a model for the geometry of the jet. Following Wang & Jiang (2020) and using a conical geometry, we have:

$$r_{\rm core} = \frac{r_\perp}{\varphi} = \frac{0.5\theta_d d_L}{(1+z)^2\varphi}, \quad (11)$$

where φ is the half-opening angle of the jet and θ_d is the angular diameter.

With our knot identification, we can estimate the half-opening angle as $\varphi = (\Theta_{0,\rm max} - \Theta_{0,\rm min})/2 \simeq 0.4^\circ$. However, this way of estimating the half-opening angle is very sensitive to the weakest components. A second way to estimate this angle is (Weaver et al. 2022) $\varphi = \theta_{\rm p}\sin\Theta_0$, where $\theta_{\rm p}$ is the projected opening semi-angle of the jet and is taken to be twice the standard deviation of the jet position angle, or of the visible component in the case of a wobbling jet direction. With our parameters, this gives about 0.78°, closer to the more widely cited (Weaver et al. 2022, Wang & Jiang 2020) value of about $\simeq 1^\circ$ for B2, the brightest component and the responsible for the 2008 flare.

For a core size at 43 GHz of $\theta_d \simeq 0.059$ mas (similar to that obtained by Kutkin et al. 2018), this gives $r_{\rm core,43\,GHz} \simeq 17$ pc. This would situate the distance from the base of the jet to the

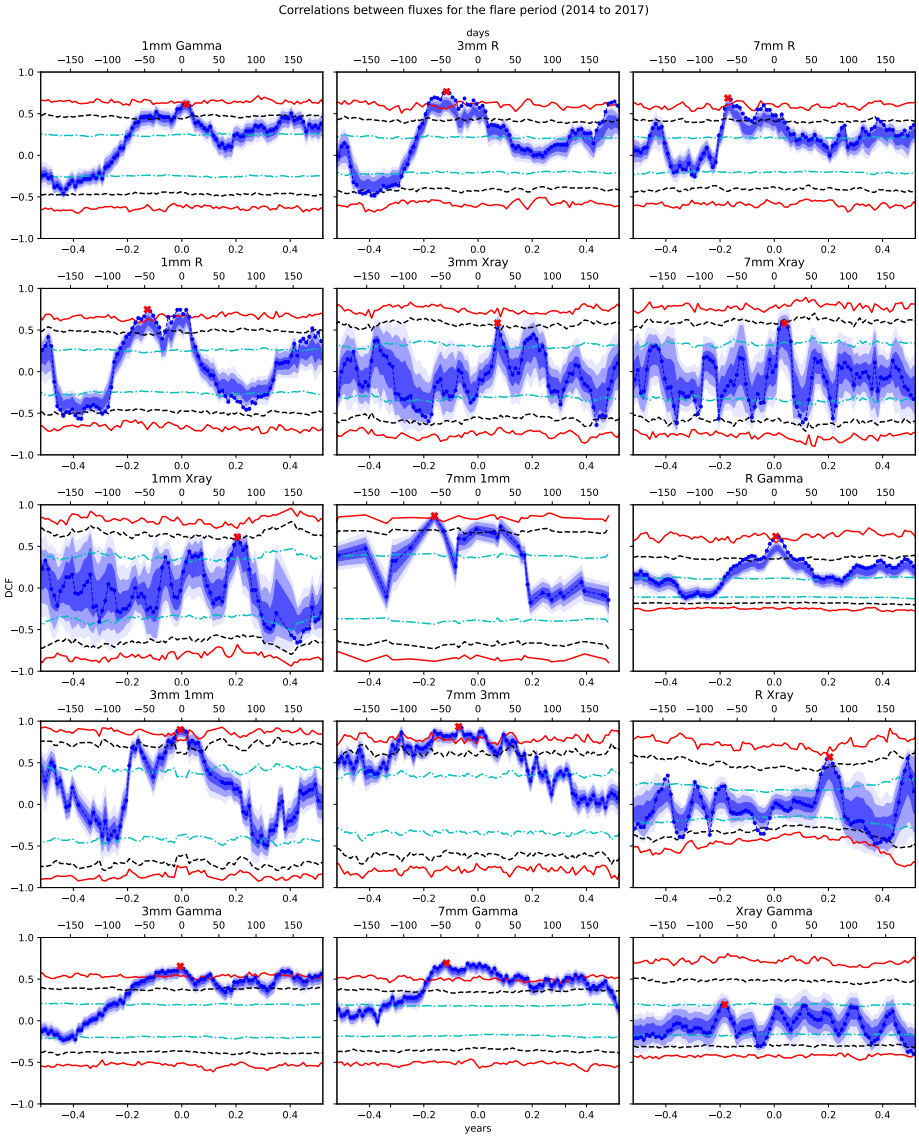

Fig. 11. Correlations between fluxes across all wavelengths. Horizontal lines show significance levels for 1σ, 2σ, and 3σ, computed using $N = 2000$ synthetic light curves, as described in Sect. 4.2. The DCFs here are computed using only the flaring episode from 2014 to 2017.

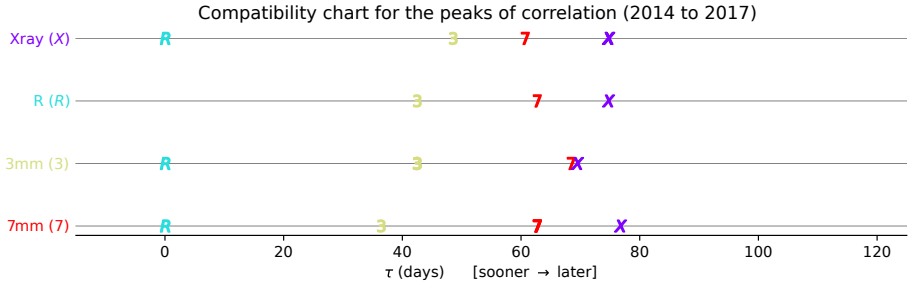

Fig. 12. Correlations compatibility chart for τ_p. Each row corresponds to a band i. The delays or peak positions between the row band i and any other band j, $\tau_p^{i,j}$, are plotted along the x-axis, shifted by the delay between the band i and the reference band, $\tau_p^{i,R}$. The peaks selected are the one with highest values of the DCF, marked with red dots in Fig. 11. The DCFs here use the flaring episode from 2014 to 2017.

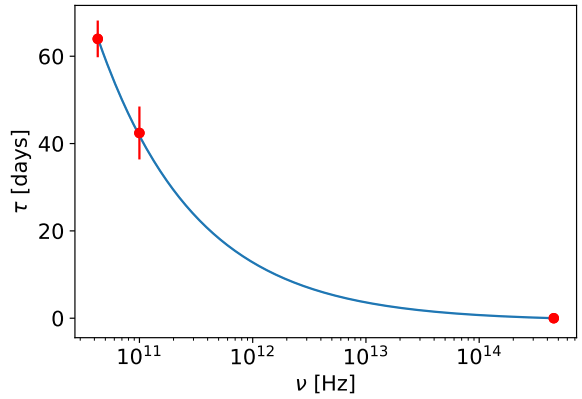

Fig. 13. Fit to the function $y = ax^{-1/2} + b$, which is the expected form if the time delays are due to different synchrotron cooling times. Fit results are $a = 1.341 \pm 0.009 \times 10^7$, $b = -6 \pm 1 \times 10^{-1}$, $p(\chi^2) = 0.909$, and $r^2 = 0.9998$. Parameter b is close to zero and accounts for an arbitrary reference delay, which is R in our case.

43 GHz core much closer than the $r_{\rm core,15\,GHz} \simeq 29$ pc obtained by Wang & Jiang (2020) at 15 GHz, consistent with opacity effects. The result is also compatible with the constraint >12 pc from Agudo et al. (2011).

4.4. Spectral energy distribution

We produced complete SEDs for the two epochs of flaring and quiescent state related to the 2008 outburst, where the MWL coverage was highest: MJD 54761 (2008-10-22), which corresponded to the peak of the flare, and MJD 55098 (2009-09-14). Analogously, we built the SED for two epochs related to the 2015 outburst: MJD 56576 (2013-10-11), which was taken as a quiescent epoch, and MJD 57293 (2015-09-28), as the flaring epoch. The last epoch is the closest one to the peak of the flare with observations in enough bands to perform an accurate modeling. These four epochs were marked with vertical lines in the MWL flux plot (Fig. 1) and their SEDs are represented together in Fig. 14 for comparison.

It can be seen that both the 2008 and 2015 flaring epochs, MJD 54761 and MJD 57923, exhibit a softening of the spectrum between the hard UV and soft X-ray ranges (Fig. 14). The feature manifests itself as a increase of the flux from optical to UV wavelengths, with the slope in the SED in the UV becoming positive, and as a increased flux in the X-ray region, with the slope becoming negative. The UV increase is much higher when using the extinction values by Junkkarinen et al. (2004), as seen in Fig. 15, but this probably overestimates the correction in the hard UV. The feature is still present in both epochs when using the values for extinction given by Ackermann (2012), specially for MJD 57923 and considerably dimmer for MJD 54761, and we have used these values to built the final SEDs. The unexplained feature seems to disappear when the source is quiescent, for both the 2008 and the 2015 flares.

The origin of this feature is still under debate, although its presence has been reported before in the literature, also for previous flares of this source. Raiteri et al. (2008) reported the presence of the UV feature in the peak of the 2006-2007 flare, and also in some other earlier epochs where the source was fainter. The change of slope in X-rays was also present in the SED reported in Ackermann (2012) for the MJD 54761-3 epoch, even though the UV increase was not evident in their SED plots. In contrast, our analysis shows that in epoch MJD 54761 that the bump is visible both in the UV and the X-ray. Raiteri et al. (2008) emphasizes that the fact that the bump is visible during flaring states is unusual for quasars. In most cases, similar features are only visible in the faintest states and are attributed to thermal emission from the disk. In contrast, 0235+164 exhibits this feature even during the brightest epochs, thus ruling out such an explanation. The thermal origin of the feature is invalidated further by the high temperatures that would be necessary to result in a bump at these energies and by the fact that the thermal emission from the disk should be approximately stable, while the difference in flux when the feature becomes visible is of more than one order of magnitude. Raiteri et al. (2008) also reported the presence of the feature in the UV for a quiescent epoch related to the 2007 flares, and some intermediate states. This, together with the lower values for the correlation of the X-rays found in our DCF analysis (Sect. 4.2) hints at a different process involved at least partially in the emission at these energies.

Table 4. Estimated delays (in days) obtained from peaks of the DCFs (Fig. 11) and represented in the compatibility chart (Fig. 12), with their average and dispersion.

	7 mm	3 mm	X-ray
7 mm	–	36.4	76.8
3 mm	68.7	–	68.7
R	62.6	42.4	74.7
Xray	60.6	48.5	–
mean	64.0	42.4	73.4
std	4.2	6.1	4.2

Notes. The delay between R and γ can be extracted directly from the DCF in Fig. 11 and it is of 2.0 days, as discussed in Sect. 4.2.

In the remainder of this section, we briefly review previous existing models and perform a comparison between them and ours, summarizing the results in Table 5. A schematic representation of the physical setup can be found in Fig. 16.

Agudo et al. (2011) postulated that the mechanism of emission was predominantly SSC from the joint analysis of VLBI images, long-term multi-wavelength light curves from mm to γ-ray energies, including polarization, and time delays. They interpreted the outburst as the result of "the propagation of a disturbance, elongated along the line of sight by light-travel time delays" that passes through a standing recollimation shock in the core and propagates down the jet, thereby creating the "superluminal knot". They also demonstrated the general correlation between the MWL flux at different bands and the appearance of the 43 GHz VLBA superluminal features and obtained the associated time delays. They argued that the variability in γ rays could not be explained within the EC scenario. Instead, they favored a model where the stronger variability in γ-rays is explained by the delayed variability in a multi-zone turbulent cell model (Marscher et al. 2010). This was supported by the general multi-wavelength correlation, as well as the variability of the polarization and the parameters derived from the superluminal components in VLBI images (see Table 5).

Ackermann (2012) produced a model of the SEDs for epochs 54761-3 (2008-10-22 – 24) and 54803-5 (2008-12-03 – 05). The high state epoch 54761 presented a secondary soft X-ray bump, which was modeled as a bulk-Compton feature, although no hint of a bump was present in the hard UV region in the SED. For

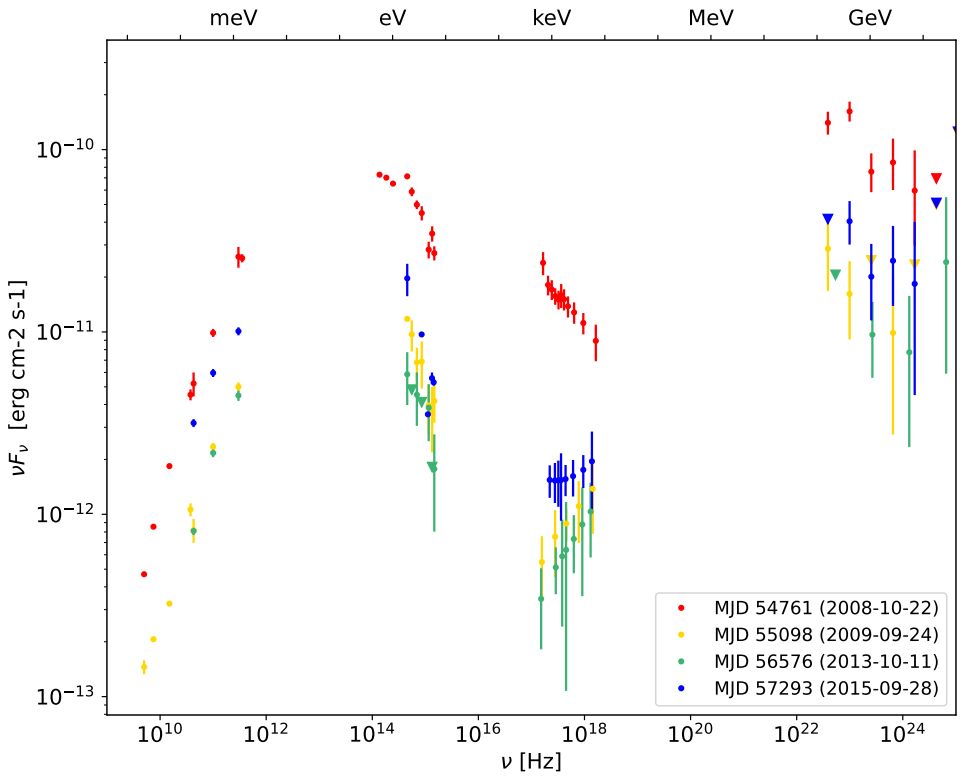

Fig. 14. Four epochs for which the SEDs were analyzed, represented together for comparison. MJD 54761 and MJD 57293 correspond to flaring epochs of the 2008 and the 2015 outbursts, respectively, while MJD 55098 and MJD 56576 correspond to quiescent epochs. The appearance of an X-ray bump is evident in the 2008 flaring epoch. It is also visible, albeit dimmer, in the 2015 flaring epoch. Both quiescent epochs lack this X-ray feature.

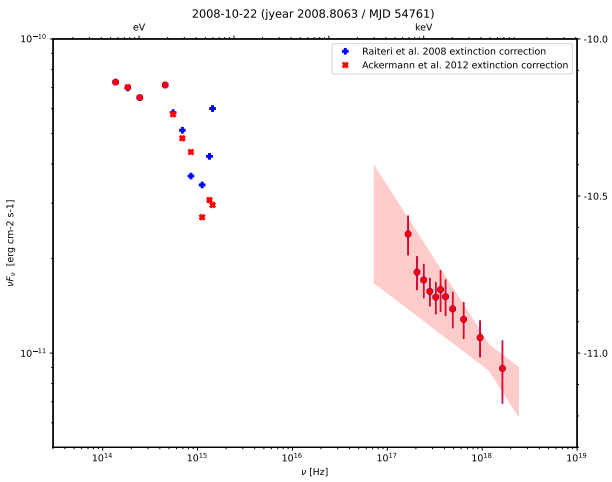

Fig. 15. Resulting UV bump applying the extinction correction from Raiteri et al. (2008) and Ackermann (2012). An increase is present in both cases, but it is much dimmer with the values by Ackermann (2012).

both of the epochs, ERCIR (Compton emission from infrared radiation from the dusty torus) was the dominating component at higher frequencies. The bulk-Compton feature was not present in the quiescent state. Ackermann argues that EC must dominate SSC for any reasonable covering factor of the broad-line region. The model presents an emission zone located outside the BLR close to the BH (1.7 pc) with a Lorentz factor $\Gamma = 20$, opening angle 2.9°, magnetic field $B' = 0.22$ G, and viewing angle 2.3°. The electron energy distribution was modeled by a doubly broken power law. The bulk-Compton feature is modeled by a population of cold electrons.

Baring et al. (2017) modeled the same epoch MJD 54761. They do so with a Lorentz factor $\Gamma = 35$. These authors modeled the energy distribution of electrons by simulating their acceleration process through diffusive shock acceleration (DSA). The bulk-Compton feature is also not present in the quiescent state. First- and second-order SSC also contributes to the second bump but is dominated at all energies by the external Compton. However, the authors notice that the Lorentz factor required by this source is significantly higher than the usual value ($\Gamma \sim 10$–20) for EC-dominated sources. The *Swift*-XRT excess is modeled as IC of a seed radiation field of $T \sim 1000$ K, postulated to be a dusty torus. Dreyer & Böttcher (2021) also presented a modeling of the SED for the same epoch, based on Baring et al. (2017), where the X-ray bump is explained by bulk-Compton emission. The second bump is also explained by external Compton from the dusty torus. If bulk Comptonization is responsible for the X-ray bump, a prediction is made that it should result in partial polarization in the X-ray bands.

In this work, we have modeled the emission of AO 0235+164 using the `JetSeT framework`[5] (Tramacere 2020; Tramacere et al. 2011, 2009), using a SSC + EC scenario. The

[5] https://jetset.readthedocs.io/en/latest/

Table 5. Summary of the comparison between different models for the flaring epoch MJD 54761.

Reference		Agudo et al. (2011) [b]	Ackermann (2012) [c]	Baring et al. (2017) [d]
Model components [a]		Synch + SSC (dom.)	Synch + EC (DT) (dom.) + SSC + BC	Synch + EC (BC) (dom.) + SSC
Bulk Lorentz factor	Γ	39.4	20 (Γ_b = 10)	35
Viewing angle	Θ	$\leqq$2.4°	2.3°	1.7°
Doppler factor	δ	24	20 (δ_b = 16)	–
Opening angle	θ	2.3°	2.9° (θ_b = 2.3°)	–
Location	r	12 pc	1.7 pc	–
Size of the emission region	R	–	–	1×10^{16} cm
Magnetic field intensity	B	–	0.22 G	2.5 G
Electrons	$\gamma_{\rm min}$	–	100	–
	$\gamma_{\rm max}$		5.8×10^3	1.61×10^3
	$n_{e^-}(E)$	–	doubly broken pwl. $p_1 = 1.5$, $p_2 = 2.03$, $p_3 = 3.9$	See footnote [e]
Protons	n_{e^-}/n_{p^+}	–	9	–
Disk luminosity	$L_{\rm disk}$	–	4×10^{45} erg s^{-1}	3.4×10^{44} erg s^{-1}
Disk temperature	$T_{\rm disk}$	–	3.5×10^3 K [f]	1×10^3 K
Disk radius	$R_{\rm disk}$	–	–	6×10^{17} cm

Notes. [a]The components considered are synchrotron (Synch), synchrotron self-Compton (SSC), external Compton (EC) from the dusty torus (DT), and bulk-Compton (BC). [b]The values for Agudo et al. (2011) do not come from a SED model, but from the DCF analysis and kinematic parameters from VLBI images, assuming a SSC scenario. The value for Γ is not cited in the paper, it is the one obtained by Weaver et al. (2022) for the same component in VLBI. [c]Parameters for the blazar zone (their model includes a second population of relativistic cold electrons to account for the secondary soft X-ray bump, whose parameters are indicated between parenthesis. [d]The secondary soft x-ray bump is modeled by bulk Comptonization of a background seed field from a dusty torus); the H.E. bump by the external Compton of the electron population. [e]The energy distribution is simulated from diffusive shock acceleration (DSA) and the resulting parameters are not explicitly indicated. [f]From the given radiation temperature of 0.3 eV.

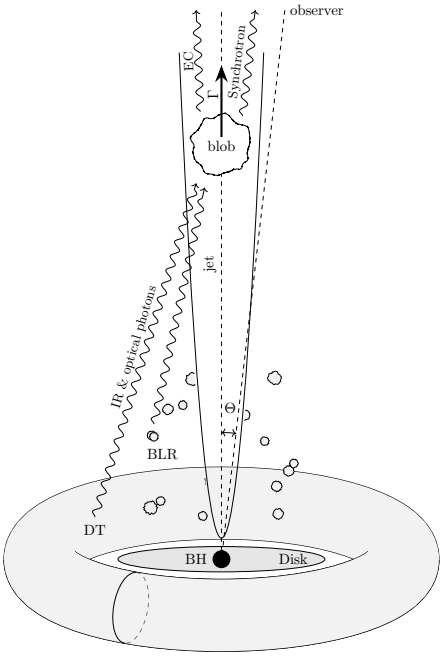

Fig. 16. Schematic representation of the physical setup. In the proposed scenario, an electron distribution (blob) in the jet, characterized by its geometrical properties, its energy distribution, and its magnetic field (Tables 7 and 8), emits synchrotron radiation. Infrared and optical photons from the disk, the dusty torus and the broad line region reach the blob and are upscattered to high energies by inverse Compton. The observer, narrowly aligned with the jet, sees the emission boosted by relativistic effects. In the case of bulk-Compton emission, an additional, different distribution would exist, closer to inner region of the blazar (Table 6).

accretion disk spectrum is modeled as a multi-temperature black body as described in Frank et al. (2002), with a luminosity fixed to $L_{\rm Disk} = 5 \times 10^{45}$ erg s^{-1}, an accretion efficiency (η) fixed to the standard value of 0.08, and a BH mass fixed to $5 \times 10^8\ M_\odot$, with an external radius of the order of a few hundreds of Schwarzschild radii. The BLR is modeled as a thin spherical shell with an internal radius determined by the phenomenological relation provided by Kaspi et al. (2007), $R_{\rm BLR,in} = 3 \times 10^{17} L_{\rm Disk,46}^{1/2}$ cm. The external radius of the BLR is assumed to be $0.1 R_{\rm BLR,in}$, with a coverage factor of $\tau_{\rm BLR} = 0.1$. The dusty torus (DT) is assumed to be described by spherical uniform radiative field, with a radius $R_{\rm DT} = 2 \times 10^{19} L_{\rm Disk,46}^{1/2}$ cm (Cleary et al. 2007), and a reprocessing factor $\tau_{\rm DT} = 0.1$. The emitting region is modeled as a single spherical zone with a radius, R, located at a distance, $R_{\rm H}$, from the central black hole. The jet has a conical geometry, with an half opening angle of $\phi \approx 3$ deg, with the emitting region size determined by $R = R_{\rm H} \tan\phi$. The emitting region moves along the jet axis with a bulk Lorentz factor, Γ, oriented at a viewing angle, θ, and a consequent beaming factor of $\delta = 1/(\Gamma \sqrt{1 - \beta_\Gamma \cos(\theta)})$. For the relativistic emitting electron distribution (EEE), we tested a broken power law (BKN) distribution:

$$n(\gamma) = N \begin{cases} \gamma^{-p} & \gamma_{\rm min} \leq \gamma \leq \gamma_b, \\ \gamma^{-p_1} \gamma_b^{p-p_1} & \gamma_b < \gamma < \gamma_{\rm max}, \end{cases} \quad (12)$$

with an index of p and p_1 below and above the break energy, γ_b, respectively, and a power law distribution with a cut-off (PLC) distribution of

$$n(\gamma) = N \gamma^{-p} \exp \frac{\gamma}{\gamma_{\rm cutoff}}, \gamma_{\rm min} \leq \gamma \leq \gamma_{\rm max}. \quad (13)$$

The initial values of $L_{\rm Disk}$ and $T_{\rm Disk}$ were determined by `JetSeT` during the pre-fit stage and $L_{\rm Disk}$ is frozen to the value of $L_{\rm Disk} = 5 \times 10^{45}$ erg s^{-1}. The model minimization was performed

Table 6. Parameters for the models of the bulk-Compton (BC) emission both with simple and conical geometries, shown in Figs. A.3, A.1, and A.2 for the epoch MJD 54761.

Epoch			MJD 54761	MJD 54761	MJD 54761
Model [(a)]			SSC-dominated + BC (simple)	EC-dominated + BC (simple)	EC-dominated + BC (conical)
Geometrical parameters					
Bulk Lorentz factor	Γ		10	10	10
Location	r	pc	4.86×10^{-3}	4.86×10^{-3} ($<1 \times 10^{-1}$)	1.30×10^{-4}
(extended)			–	–	2.76×10^{-3}
Size	R	pc	3.28×10^{-3} (3.83×10^{-5})	3.24×10^{-3}	1.56×10^{-4}
(extended)			–	–	3.32×10^{-3}
Light crossing time	$t_{\rm var}^{\rm obs}(R, \Gamma, \theta)$	day	0.4	0.4	0.02
(extended)			–	–	0.4
Magnetic field	B	G	9.14×10^{-2} G (4×10^{-2})	9.19×10^{-2} G (7×10^{-3})	0.1
(extended)					0.1
Particle distribution					
Minimum Lorentz factor	$\gamma_{\rm min}$		1.0	1.00	1.0
Maximum Lorentz factor	$\gamma_{\rm max}$		4.0 (1×10^{-1})	4.33 ($<1 \times 10^{-2}$)	1.2
Type	$n_{\rm e^-}(E)$		PL	PL	PL
Density	N	$\rm cm^{-3}$	4.46×10^5 (2×10^4)	4.33×10^5 ($<1 \times 10^{-3}$)	3.11×10^5
Spectral slope	p		2.85 (7×10^{-2})	3.00 ($<1 \times 10^{-2}$)	1.0

Notes. Uncertainties for the best-fit values were automatically obtained using the `HESSE` method of second derivatives and are indicated in parentheses. Parameters without uncertainties were frozen during the fit. For uncertainties smaller than the third significant digit, an upper limit is given. The rest of the parameters for the models can be found in Tables 7 and 8, together with their uncertainties and fit statistics. [(a)]Only the parameters of the bulk-Compton emission are shown here. See Tables 7 and 8 for the rest of the parameters.

using the `JetSeT ModelMinimizer` module plugged into the `iminuit` Python interface (Dembinski et al. 2020). The errors were estimated from the matrix of second derivatives, using the `HESSE` method. We fit the data above 30 GHz, excluding data below the synchrotron self-absorption frequency. To avoid the small errors in the UV-to-radio frequencies biasing the fit toward the lower frequencies, we added a 20% systematic error to data below 10^{16} Hz. We find that the PLC model provides a slightly better fit to the data, thus, in the following, we present only the results for this model. All the states presented in this analysis can be modeled by a single-zone EC-dominated (see Figs. A.4, A.6, and A.8 as well as Table 7) or an SSC-dominated scenario (see Figs. A.5 and A.7 and Table 8), with the SSC-dominated scenario resulting in systematically lower values of B, needed to accommodate for the proper $U_{\rm e}/U_{\rm B}$ ratio able to match the peak flux and frequency of the IC emission. On the contrary, for the flaring state on MJD 54761, the presence of a strong and soft bump in the X-ray makes both the SSC and EC unable to model the data. As suggested by Celotti et al. (2007), Ackermann (2012), this spectral feature can be explained by the Comptonization of the external radiative fields by a population of cold electrons. We have introduced such bulk-Compton (BC) component, modeled as a spherical region with a radius, $R_{\rm BC}$, moving with corresponding bulk factor of $\Gamma = 10$, at a distance, r, from the BH and with a total number of particles, $N_{\rm BC}$.

We notice that for a purely cold population, namely, for electrons with $\gamma_{\rm min} = \gamma_{\rm max} = \gamma = 1$, the resulting shape of the BC radiation was always too steep to reproduce the observed data (see e.g., Celotti et al. 2007); on the contrary, we found that a reasonable fit to the data was provided by increasing the fit range of $\gamma_{\rm max}$ to 5, and setting $r = 1.5 \times 10^{16}$ cm. With this model configuration, the fit converged with a resulting value of $\gamma_{\rm max} \approx 4$ and a resulting total number of cold electrons of $N_{\rm BC} \approx 1.8 \times 10^{54}$ (see Fig. A.2 and left column in Table 6). These values are compatible with those reported in Ackermann (2012; $N_{\rm BC} = 2.4 \times 10^{54}$ and $r = 5 \times 10^{15}$ cm), anyhow we stress that in Ackermann (2012) the BC spectral shapes is assumed to be a PL, whilst in the present analysis, it is obtained by the actual Comptonization of the cold electrons. We also applied the BC model to an SSC-dominated scenario (see Fig. A.3 and Tables 6 and 8), we notice that even though the overall agreement of the model with the data is still reasonable, the model shows some tension in the optical-IR and X-ray data. At the high-energy branch of the X-ray data, the excess of flux in the model is due to the broader spectrum of IC emission compared to the EC case, originating from the broader spectrum of the synchrotron seed photons compared to the narrower seed photon spectrum of the external fields.

Another possible option that would be able to produce a PL shape for the BC could be obtained by assuming a purely cold electron population with a truncated conical geometry. The higher energy part of the BC would be produced by the low-number electrons closer to BH and the higher energy would be produced by the larger number of electrons in the upper part of the truncated cone. To mimic such a geometry we implemented a BC model with two spherical regions.The radius of the two regions is obtained so that the two spheres match the volume of the upper and lower parts of the truncated cone. We find that a reasonable modeling of the BC emission is obtained assuming a truncated cone, with an opening angle of 45° and an height of $\approx 9 \times 10^{15}$ cm. The smaller spherical region corresponds to the segment of the truncated cone with an height of $\approx 5 \times 10^{15}$ cm and the larger spherical region corresponds to the segment with an height of $\approx 8 \times 10^{15}$ cm The total number of cold electrons is of $N_{\rm BC} \approx 1.4 \times 10^{54}$ (see Fig. A.2 and left column in Table 6). Since the introduction of this extra component introduces new parameters, first, we used the `ModelMinimizer` to fit the model to the data without the BC component and excluding the X-ray data (statistics are reported in Tables 7 and 8) and, in a second step, we added the X-ray data and we proceeded to a qualita-

Table 7. Parameters in the external-Compton (EC) scenario for epochs MJD 54761 (Figs. A.1 and A.2), MJD 55098 (Fig. A.4), MJD 56576 (Fig. A.6), and MJD 57293 (Fig. A.8).

Epoch			MJD 54761	MJD 55098	MJD 56576	MJD 57293
Model			EC-dominated + BC [(a)]	EC-dominated	EC-dominated	EC-dominated
Geometrical parameters						
Bulk Lorentz factor	Γ		34.0 ($<1\times10^{-1}$)	20.4 (5×10^{-1})	16.5 ($<\times10^{-1}$)	25 (3)
Viewing angle	Θ	$^\circ$	1.50 ($<1\times10^{-2}$)	1.33 (6×10^{-2})	1.07 ($<\times10^{-2}$)	1.40 (8×10^{-2})
Opening angle	θ	$^\circ$	3.0	=	=	=
Location of the emission region	r	pc	5.41 ($<1\times10^{-2}$)	4.52	4.78 ($<\times10^{-2}$)	4.60 (9×10^{-2})
Size of the emission region	R	pc	0.28	0.24	0.25	0.24
Light crossing time	$t_{\rm var}^{\rm obs}(R,\Gamma,\theta)$	day	17 (1)	15 (1)	19 (1)	15 (3)
Magnetic field intensity	B	G	6.03×10^{-2} ($<1\times10^{-4}$)	2.9×10^{-1} (2×10^{-2})	5.00×10^{-2} ($<10^{-4}$)	7.7×10^{-2} (4×10^{-3})
Particle distribution						
Minimum Lorentz factor	$\gamma_{\rm min}$		1.06 ($<1\times10^{-2}$)	1.10 (3×10^{-2})	1.06 ($<10^{-2}$)	1.6 (3×10^{-1})
Maximum Lorentz factor	$\gamma_{\rm max}$		7.20×10^{5} ($<1\times10^{3}$)	7.6×10^{5} (6×10^{4})	1.11×10^{5} ($<10^{3}$)	9.1×10^{4} (2×10^{3})
Type	$n_{\rm e^-}(E)$		PLC	=	=	=
Density	N	cm^{-3}	3.39×10^{1} ($<1\times10^{-1}$)	$4.7(3\times10^{-1})$	6.96×10^{1} ($<\times10^{-1}$)	5.7×10^{1} (1×10^{1})
Cutoff Lorentz factor	$\gamma_{\rm cutoff}$		4.70×10^{3} ($<1\times10^{1}$)	3.6×10^{3} (1×10^{2})	6.6×10^{3} (7×10^{2})	4.0×10^{3} (2×10^{3})
Spectral slope	p		2.05 ($<1\times10^{-2}$)	2.35 (1×10^{-2})	2.30 ($<\times10^{-2}$)	2.4 (1×10^{-1})
Accretion disk						
Black hole mass	$M_{\rm BH}$	$M_\odot$	5×10^{8}	=	=	=
Accretion efficiency	η		8×10^{-2}	=	=	=
Disk inner radius	$R_{\rm disk,in}$	$R_{\rm S}$	3.0	=	=	=
Disk outer radius	$R_{\rm disk,out}$	$R_{\rm S}$	5×10^{2}	=	=	=
Disk luminosity	$L_{\rm disk}$	erg s^{-1}	5.0×10^{45}	=	=	=
Disk temperature	$T_{\rm disk}$	K	5.96×10^{4}	=	=	=
Disk torus (DT)						
Temperature	$T_{\rm DT}$	K	330	=	=	=
Fraction of disk luminosity reprocessed	$\tau_{\rm DT}$		0.1	=	=	=
Broad line region (BLR)						
Inner radius	$R_{\rm BLR,in}$	pc	6.87×10^{-2}	=	=	=
Outer radius	$R_{\rm BLR,out}$	pc	7.56×10^{-2}	=	=	=
Fraction of disk luminosity reprocessed	$\tau_{\rm BLR}$		0.1	=	=	=
Fit statistics						
degrees of freedom	d.o.f.		14	16	18	15
chi-squared statistic	χ^2		21.9	16.0	10	10.1

Notes. Uncertainties for the best-fit values were automatically obtained using the HESSE method of second derivatives and are indicated between parenthesis, parameters without them were frozen during the fit. For uncertainties smaller than the third significant digit, an upper limit is given. The degrees of freedom and the χ^2 statistic for the model fit are indicated in the last rows, the residuals are shown in the figures. [(a)]The model for this epoch includes an additional component which is independently modeled as bulk-Compton emission from the disk, the reported values refer to the SSC/EC components alone, with the exclusion of the X-ray data. Two possible geometries where considered for the EC-dominated scenario, and their parameters can be found Table 6.

tive fitting of the BC conical component (the values of the BC component are reported in Table 6).

The flaring epoch MJD 57293 could also be modeled using a single-zone model, although the observed softening of the X-ray spectrum could be explained by bulk-Compton emission in two-zone model. This could be done in a similar manner to the case of MJD 54761, as the DCF analysis for 2014-2017 indicates.

5. Discussion and conclusions

We have presented new and updated multi-wavelength photometric and polarimetric data of AO 0235+164, all across the spectrum from radio cm and mm wavelengths up to γ-ray energies. The analysis of the correlations have shown that the emission at different wavelengths is statistically correlated, linking their emission mechanisms, with the notable exception of the X-ray band.

We have analyzed and shown the compatibility between the positions of the peaks of the different correlations, strengthening their interpretation as the delay between emissions. In this context, we have also shown that the obtained delays are compatible with the proposed emission mechanisms: from mm to optical wavelengths, the delays agree with what it is to be expected for synchrotron emission.

In addition, we have also seen that the γ-ray light curve is indeed correlated with the mm and R-band emissions, which is

Table 8. Parameters in the SSC-dominated scenario scenario for epochs MJD 54761, MJD 55098, MJD 56576, and MJD 57293, corresponding to models shown in Figs. A.3, A.5, and A.7.

Epoch			MJD 54761	MJD 55098	MJD 56576
Model components			SSC-dominated + BC [(a)]	SSC-dominated	SSC-dominated
Geometrical parameters					
Bulk Lorentz factor	Γ		38.4 (5)	21.1 (1)	25.0 ($<10^{-2}$)
Viewing angle	Θ	$^\circ$	1.55 (1×10^{-2})	1.79 ($<\times10^{-2}$)	1.66 ($<\times10^{-2}$)
Opening angle	θ	$^\circ$	3.0	1.5	1.5
Location of the emission region	r	pc	32.4 ($<10^{-1}$)	16.2	16.2 ($<10^{-1}$)
Size of the emission region	R	pc	1.70	0.42	0.42
Light crossing time	$t_{\rm var}^{\rm obs}(R,\Gamma,\theta)$	day	106 (20)	33 (3)	30 (1)
Magnetic field intensity	B	G	2.00×10^{-3} ($<10^{-5}$)	6.74×10^{-3} (7×10^{-4})	5.63×10^{-3} ($<10^{-5}$)
Particle distribution					
Minimum Lorentz factor	$\gamma_{\rm min}$		4.38×10^{1} ($<1\times10^{-1}$)	1.10×10^{2} (<1)	4.57×10^{1} ($<10^{-1}$)
Maximum Lorentz factor	$\gamma_{\rm max}$		9.12×10^{6} (4×10^{4})	8.71×10^{5} ($<10^{3}$)	7.30×10^{5} ($<10^{3}$)
Type	$n_{e^-}(E)$		PLC	PLC	PLC
Density	N	cm^{-3}	9.94×10^{-2} (3×10^{-4})	5.35×10^{-1} ($<10^{-3}$)	8.51×10^{-1} ($<10^{-3}$)
Cutoff Lorentz factor	$\gamma_{\rm cutoff}$		1.50×10^{4} ($<10^{2}$)	9.33×10^{3} ($<10^{1}$)	8.73×10^{3} ($<10^{1}$)
Spectral slope	p		1.50 ($<10^{-2}$)	1.64 ($<10^{-2}$)	1.68 ($<10^{-2}$)
Accretion disk					
Black hole mass	$M_{\rm BH}$	$M_\odot$	5×10^{8}	=	=
Accretion efficiency	η		8×10^{-2}	=	=
Disk inner radius	$R_{\rm disk,in}$	$R_{\rm S}$	3.0	=	=
Disk outer radius	$R_{\rm disk,out}$	$R_{\rm S}$	5×10^{2}	=	=
Disk luminosity	$L_{\rm disk}$	erg s^{-1}	5.0×10^{45}	=	=
Disk temperature	$T_{\rm disk}$	K	5.96×10^{4}	=	=
Disk torus (DT)					
Temperature	$T_{\rm DT}$ (K)	330	=	=	
Fraction of disk luminosity reprocessed	$\tau_{\rm DT}$	0.1	=	=	
Broad line region (BLR)					
Inner radius	$R_{\rm BLR,in}$	pc	6.87×10^{-2}	=	=
Outer radius	$R_{\rm BLR,out}$	pc	7.56×10^{-2}	=	=
Fraction of disk luminosity reprocessed	$\tau_{\rm BLR}$		0.1	=	=
Fit statistics					
degrees of freedom	d.o.f.		20	16	10
chi-squared statistic	χ^2		44.4	6.9	7.2

Notes. Uncertainties for the best-fit values were automatically obtained using the HESSE method of second derivatives and are indicated in parentheses, parameters without uncertainties were frozen during the fit. For uncertainties smaller than the third significant digit, an upper limit is given. The degrees of freedom and the χ^2 statistic for the model fit are indicated in the last rows, the residuals are indicated in the figures. [(a)]The model for this epoch includes an additional componed which is independly modeled as bulk-Compton emission from the disk. See Table 6 for the parameters of the BC emission model.

to be expected if the dominating emission mechanism is SSC or EC. Furthermore, the γ-ray subflares seem to be related to the appearance of identifiable VLBI components.

On the other hand, we have not found a significant correlation between the X-ray light curve and the rest of the bands. This is explained by the presence of the X-ray bump in the SED. This bump can not be accounted for by a closely correlated emission (SSC or EC) with the rest of the bands. Instead, it is proposed that it corresponds to bulk-Compton emission from a different population of particles. The large obtained delays imply that this emitting zone is separated by a large distance from the main emission component and this is further confirmed by the results from the SED modeling.

Understanding how our observational data and results fit in the current landscape of existing blazar models is a difficult task. There is the rebrightening of knot features, which could be explained by successive recollimation shocks with the jet, and the difference in Doppler factor and speed between different components, which could be explained by different energies of a shock wave, points toward a shock-in-jet model. The observed post-maximum subflares in 3 mm and γ-ray can be explained by less energetic recollimation of the same dulled shockwave,

analogously to the rebrightning of knot features farther from the jet as seen in the VLBA images, they even appear to be more or less simultaneous. The observed longer duration of the flare in mm wavelengths is explained in this model by the longer cooling of synchrotron electrons. This smears out the peak in the correlation and shifts the correlation shape to show a delay of mm emission.

The question about whether SSC or EC dominates the high energy bump does not have a clear, definite answer. EC-dominated SED models seem to be favored by literature (Ackermann 2012, Dreyer & Böttcher 2021). However, as we present in this paper, SSC-dominated models are also possible (as shown in Sect. 4.4). It is generally easier and more common to produce a fit with dominant EC, however, the model is harder to explain physically and the obtained delays in the correlation analysis and the results from VLBI observations favor SSC-dominated models.

The delays between signals are not directly interpretable as the relative time at which emissions at different wavelengths start; this interpretation would be valid only if the signals had the same shape but were shifted with respect to each other, which is not the case here. However, the correlation between R and γ shows a clear peak whose position is $\tau_{\rm p}^{R,\gamma}$ of 2 days, which corresponds to a distance of less than 1 pc after accounting for relativistic effects. Meanwhile, the large delay obtained between R and X-ray place the emission regions at tens of parsecs away, which aptly fits the obtained distances in the SSC scenario where the X-ray is produced by bulk-Compton emission.

The results from the kinematic analysis of VLBI components show that the 43 GHz core is located at distances from 12 pc to 17 pc downstream from the central BH, assuming a conical jet geometry. The best-fit distances obtained in SSC-models (Table 8) are in better agreement with the ones obtained from the VLBI kinematic analysis and, in any case, since the SSC emission is less dependent on the distance to the BH, other distances are easier to accommodate. This is not the case in the EC-scenario.

Scenarios where the γ-emitting zone is close to the central BH are ruled-out by the long-term and highly significant correlation (Fig. 10) between γ, R, and mm light curves, since the emissions must be close enough and from analysis of VLBI images we know this is more than ten parsecs away from the central engine. SED models also help us discard these scenarios.

The presence of IC flares after the synchrotron flares has already ceased, as in the case in some instances between the 2008 and 2015 flares, is also an indicator of SSC (Sokolov et al. 2004). They can be explained by the time-delays and crossing times, specially for small viewing angles such as AO 0235+164. However, this is not valid in a EC scenario. Also, the observed stronger variability in γ-rays with respect to low energies is harder to explain in the EC scenario, where there is no reasonable source of increased variability.

A good test to determine whether the emission is SSC or EC might be the polarization of the γ-rays. Generally, EC is not expected to have significant polarization, while SSC is expected to have a polarization degree about half of the corresponding synchrotron emission. While the X-ray polarization is already being measured by some instruments (IXPE), γ-ray polarization is still not possible, although recent technological developments have opened the possibility up in the next decade.

Acknowledgements. The IAA-CSIC team acknowledges financial support from the Spanish "Ministerio de Ciencia e Innovación" (MCIN/AEI/10.13039/501100011033) through the Center of Excellence Severo Ochoa award for the Instituto de Astrofísica de Andalucía-CSIC (CEX2021-001131-S), and through grants PID2019-107847RB-C44 and PID2022-139117NB-C44. This research has made use of the NASA/IPAC Extragalactic Database (NED), which is operated by the Jet Propulsion Laboratory, California Institute of Technology, under contract with the National Aeronautics and Space Administration. J.Y.K. was supported for this research by the National Research Foundation of Korea (NRF) grant funded by the Korean government (Ministry of Science and ICT; grant no. 2022R1C1C1005255). IRAM is supported by INSU/CNRS (France), MPG (Germany) and IGN (Spain). The VLBA is an instrument of the National Radio Astronomy Observatory, USA. The National Radio Astronomy Observatory is a facility of the National Science Foundation operated under cooperative agreement by Associated Universities, Inc. This study was based (in part) on observations conducted using the 1.8 m Perkins Telescope Observatory (PTO) in Arizona (USA), which is owned and operated by Boston University. The BU group was supported in part by US National Science Foundation grant AST-2108622, and NASA *Fermi* GI grants 80NSSC20K1567 and 80NSSC22K1571.

References

Abdo, A. A., Ackermann, M., Ajello, M., et al. 2010, ApJ, 722, 520
Ackermann, M., et al. 2012, ApJ, 751, 159
Agudo, I., Gómez, J.-L., Martí, J.-M., et al. 2001, ApJ, 549, L183
Agudo, I., Marscher, A. P., Jorstad, S. G., et al. 2011, ApJ, 735, L10
Agudo, I., Marscher, A. P., Jorstad, S. G., et al. 2012, ApJ, 747, 63
Agudo, I., Thum, C., Molina, S. N., et al. 2017a, MNRAS, 474, 1427
Agudo, I., Thum, C., Ramakrishnan, V., et al. 2017b, MNRAS, 473, 1850
Arnaud, K. A. 1996, in Astronomical Data Analysis Software and Systems V, eds. G. H. Jacoby, & J. Barnes, ASP Conf. Ser., 101, 17
Baring, M. G., Böttcher, M., & Summerlin, E. J. 2017, MNRAS, 464, 4875
Barthelmy, S. D., Barbier, L. M., Cummings, J. R., et al. 2005, Space Sci. Rev., 120, 143
Blandford, R., Meier, D., & Readhead, A. 2019, ARA&A, 57, 467
Blinov, D., & Pavlidou, V. 2019, Galaxies, 7, 46
Breeveld, A. A., Curran, P. A., Hoversten, E. A., et al. 2010, MNRAS, 406, 1687
Burrows, D. N., Hill, J. E., Nousek, J. A., et al. 2005, Space Sci. Rev., 120, 165
Casadio, C., Gómez, J. L., Jorstad, S. G., et al. 2015, ApJ, 813, 51
Celotti, A., Ghisellini, G., & Fabian, A. C. 2007, MNRAS, 375, 417
Cleary, K., Lawrence, C. R., Marshall, J. A., Hao, L., & Meier, D. 2007, ApJ, 660, 117
Cohen, R. D., Smith, H. E., Junkkarinen, V. T., & Burbidge, E. M. 1987, ApJ, 318, 577
Dembinski, H., Ongmongkolkul, P., Deil, C., et al. 2020, https://zenodo.org/records/8249703
Dreyer, L., & Böttcher, M. 2021, ApJ, 910, 2
Evans, P. A., Beardmore, A. P., Page, K. L., et al. 2009, MNRAS, 397, 1177
Frank, J., King, A., & Raine, D. J. 2002, Accretion Power in Astrophysics: Third Edition (Cambridge University Press)
Gehrels, N., Chincarini, G., Giommi, P., et al. 2004, ApJ, 611, 1005
Hill, J. E., Burrows, D. N., Nousek, J. A., et al. 2004, in X-Ray and Gamma-Ray Instrumentation for Astronomy XIII, eds. K. A. Flanagan, & O. H. W. Siegmund, SPIE Conf. Ser., 5165, 217
Jorstad, S. G., Marscher, A. P., Mattox, J. R., et al. 2001, ApJS, 134, 181
Jorstad, S. G., Marscher, A. P., Lister, M. L., et al. 2005, AJ, 130, 1418
Junkkarinen, V. T., Cohen, R. D., Beaver, E. A., et al. 2004, ApJ, 614, 658
Kaspi, S., Brandt, W. N., Maoz, D., et al. 2007, ApJ, 659, 997
Kutkin, A. M., Pashchenko, I. N., Lisakov, M. M., et al. 2018, MNRAS, 475, 4994
Madejski, G., Takahashi, T., Tashiro, M., et al. 1996, ApJ, 459, 156
Marscher, A. P., Jorstad, S. G., D'Arcangelo, F. D., et al. 2008, Nature, 452, 966
Marscher, A. P., Jorstad, S. G., Larionov, V. M., et al. 2010, ApJ, 710, L126
Moretti, A., Campana, S., Mineo, T., et al. 2005, in UV, X-Ray, and Gamma-Ray Space Instrumentation for Astronomy XIV, ed. O. H. W. Siegmund, SPIE Conf. Ser., 5898, 360
Planck Collaboration VI. 2020, A&A, 641, A6
Poole, T. S., Breeveld, A. A., Page, M. J., et al. 2008, MNRAS, 383, 627
Raiteri, C. M., Villata, M., Ibrahimov, M. A., et al. 2005, A&A, 438, 39
Raiteri, C. M., Villata, M., Larionov, V. M., et al. 2008, A&A, 480, 339
Roming, P. W. A., Kennedy, T. E., Mason, K. O., et al. 2005, Space Sci. Rev., 120, 95
Scargle, J. D., Norris, J. P., Jackson, B., & Chiang, J. 2013, ApJ, 764, 167
Sokolov, A., Marscher, A. P., & McHardy, I. M. 2004, ApJ, 613, 725
Tavecchio, F., Bonnoli, G., & Galanti, G. 2020, MNRAS, 497, 1294
Thum, C., Agudo, I., Molina, S. N., et al. 2017, MNRAS, 473, 2506
Tramacere, A. 2020, Astrophysics Source Code Library [record ascl:2009.001]
Tramacere, A., Giommi, P., Perri, M., Verrecchia, F., & Tosti, G. 2009, A&A, 501, 879
Tramacere, A., Massaro, E., & Taylor, A. M. 2011, ApJ, 739, 66
Tramacere, A., Sliusar, V., Walter, R., Jurysek, J., & Balbo, M. 2022, A&A, 658, A173
Wang, Y.-F., & Jiang, Y.-G. 2020, ApJ, 902, 41
Weaver, Z. R., Jorstad, S. G., Marscher, A. P., et al. 2022, ApJS, 260, 12
Welsh, W. F. 1999, PASP, 111, 1347

Appendix A: Spectral Energy Distribution models

This is a collection of the spectral energy distribution (SED) models presented in Sect. 4.4.

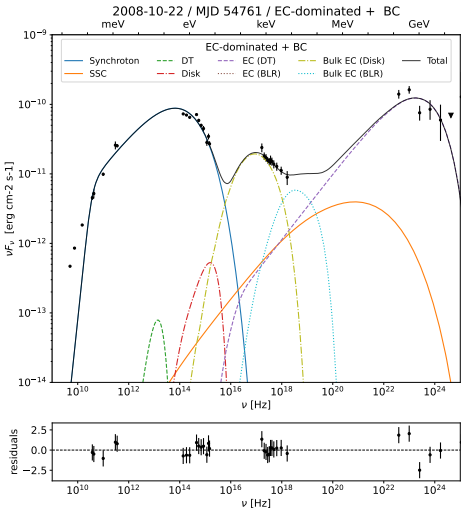

Fig. A.1. SED model for epoch MJD 54761. The model includes the usual synchrotron plus SSC components, but the high-energy bump is dominated by EC emission from a dusty torus (Table 7). The X-ray bump is modeled by bulk-Compton emission from the disk by a secondary particle distribution much closer to the central engine (Table 6), consistent with the much lower correlation and higher delays in the DCFs between X-ray and the other bands (Fig. 12).

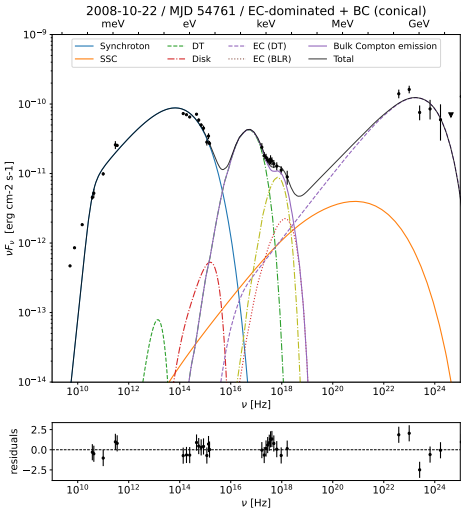

Fig. A.2. SED model for epoch MJD 54761. The EC-dominated model includes a bulk-Compton component with a conical shape.

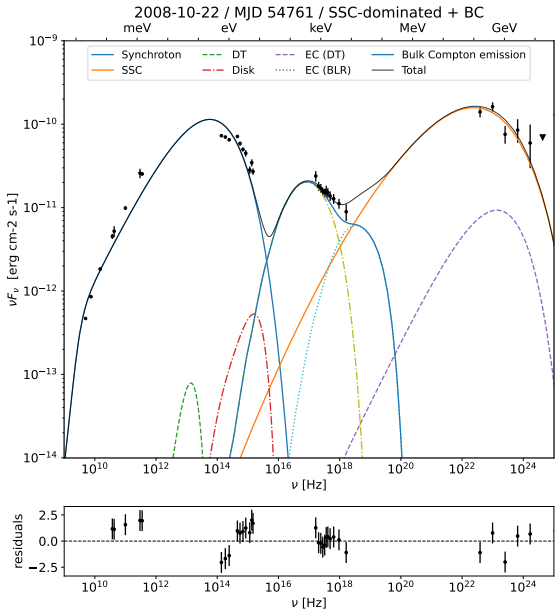

Fig. A.3. SED model for epoch MJD 54761 in the SSC-dominated scenario. The X-ray bump is modeled as bulk-Compton emission from the disk in a similar way to the EC-dominated model (Table 6).

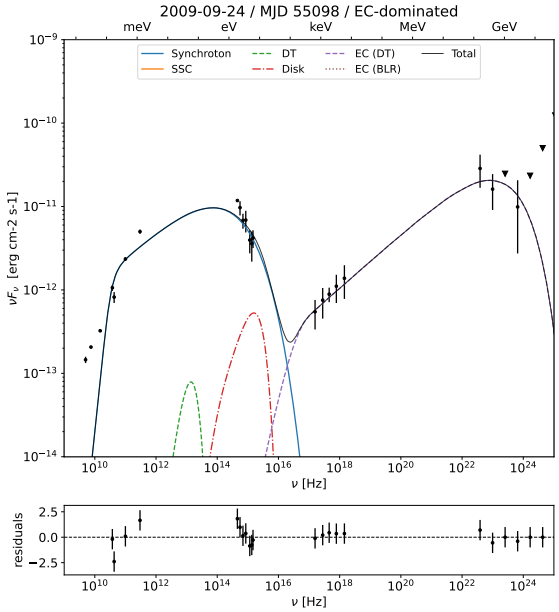

Fig. A.4. SED model for epoch MJD 55098 in the EC-dominated scenario (Table 7).

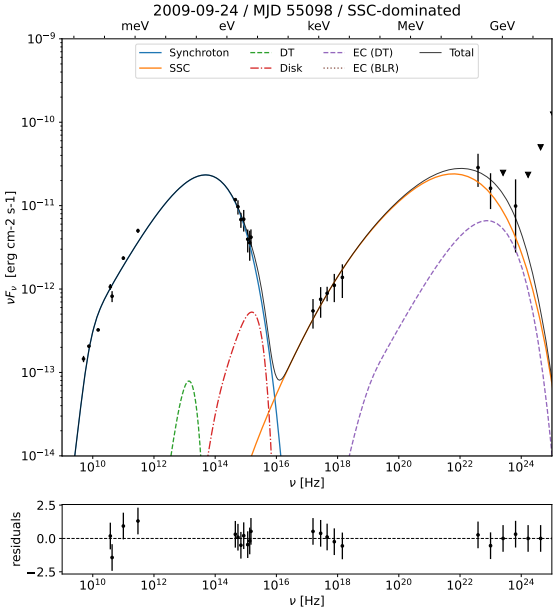

Fig. A.5. SED model for epoch MJD 55098 in the SSC-dominated scenario (Table 8).

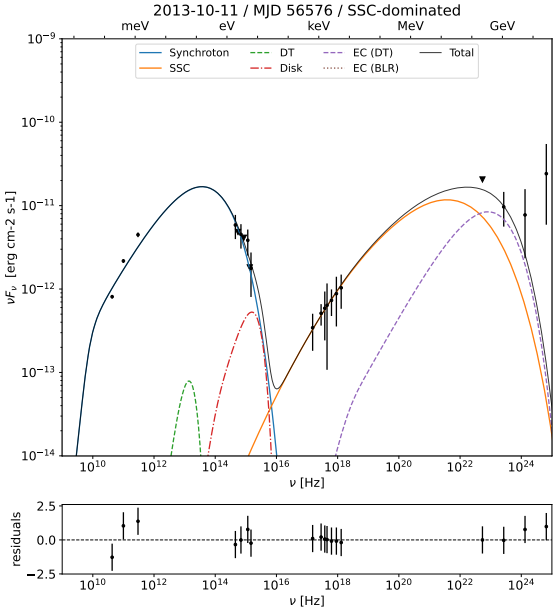

Fig. A.7. SED model for epoch MJD 56576 in the SSC-dominated scenario (Table 8).

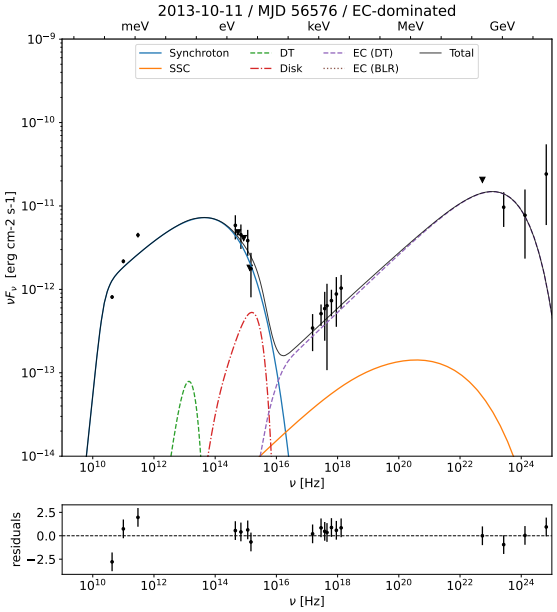

Fig. A.6. SED model for epoch MJD 56576 in the EC-dominated scenario (Table 7).

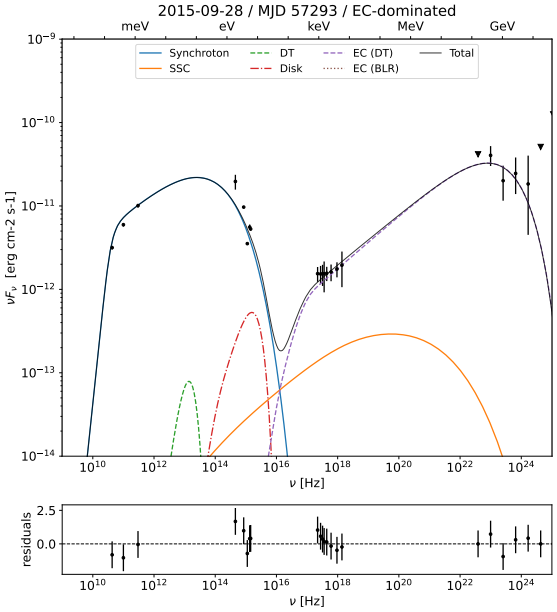

Fig. A.8. SED model for epoch MJD 57293 in the EC-dominated scenario (Table 8). Unlike the models for the older flaring epoch 54761 (Figs. A.1, A.2), this model does not include a bulk-Compton component and can be explained with only the usual SSC+EC components. The source exhibits an important softening in the X-ray spectrum that could also be explained by bulk-Compton emission.

Appendix B: Swift observations

The *Neil Gehrels Swift* observatory satellite (Gehrels et al. 2004) carried out 195 observations of AO 0235+164 between 2005 June 28 (MJD 53549) and 2016 February 11 (MJD 57429). The observations were performed with all three on-board instruments: the X-ray Telescope (XRT; Burrows et al. 2005, 0.2–10.0 keV), Ultraviolet/Optical Telescope (UVOT; Roming et al. 2005, 170–600 nm), and the Burst Alert Telescope (BAT; Barthelmy et al. 2005, 15–150 keV).

All XRT observations were performed in photon counting mode (for a description of XRT read-out modes, see Hill et al. 2004). The XRT spectra were generated with the *Swift*-XRT data product generator tool at the UK Swift Science Data Centre[6] (for details, see Evans et al. 2009). Spectra having count rates higher than 0.5 counts s^{-1} may be affected by pile-up. To correct for this effect, the central region of the image was excluded and the source image has been extracted with an annular extraction region with an inner radius that depends on the level of pile-up (see e.g., Moretti et al. 2005). We used the spectral redistribution matrices in the Calibration database maintained by HEASARC. The X-ray spectral analysis was performed using the `XSPEC 12.13.0c` software package (Arnaud 1996). Data were grouped for having at least 20 counts per bins with `grppha` and the chi square statistics is used. All XRT spectra are fitted with an absorbed log-parabola model, except for cases with low number of counts, and a HI column density fixed to 2.8×10^{21} cm^{-2} for taking into account the absorption effects of both our own Galaxy and an intervening $z = 0.524$ system (see e.g. Madejski et al. 1996).

The hard X-ray flux of this source is usually below the sensitivity of the BAT instrument for daily short exposures. Moreover, the source is not included in the Swift-BAT 157-month catalogue[7]. During the *Swift* pointings, the UVOT instrument observed the sources in its optical (v, b, and u) and UV ($w1$, $m2$, and $w2$) photometric bands (Poole et al. 2008; Breeveld et al. 2010). The UVOT data in all filters were analysed with the `uvotimsum` and `uvotmaghist` tasks and the 20201215 CALDB-UVOTA release. Source counts were extracted from a circular region of 5 arcsec radius centered on the source, while background counts were derived from a circular region with a 20 arcsec radius in a nearby source-free region.

[6] http://www.swift.ac.uk/user_objects

[7] https://swift.gsfc.nasa.gov/results/bs157mon/

Chapter 4

The Flaring Activity of Blazar AO 0235+164 During Year 2021

The article has been accepted and published in *Astronomy & Astrophysics* (`https://doi.org/10.1051/0004-6361/202449726`). The full reference can be found at [38].

A&A, 689, A56 (2024)
https://doi.org/10.1051/0004-6361/202449726

Astronomy & Astrophysics

The flaring activity of blazar AO 0235+164 in 2021

Juan Escudero Pedrosa[1,⋆], Iván Agudo[1], Till Moritz[1], Alan P. Marscher[2], Svetlana Jorstad[2,9], Andrea Tramacere[3], Carolina Casadio[4,5], Clemens Thum[6], Ioannis Myserlis[6], Albrecht Sievers[6], Jorge Otero-Santos[1], Daniel Morcuende[1], Rubén López-Coto[1], Filippo D'Ammando[7], Giacomo Bonnoli[8,1], Mark Gurwell[10], José Luis Gómez[1], Ramprasad Rao[10], and Garrett Keating[10]

[1] Instituto de Astrofísica de Andalucía, CSIC, Glorieta de la Astronomía s/n, 18080 Granada, Spain
[2] Institute for Astrophysical Research, Boston University, 725 Commonwealth Avenue, Boston, MA 02215, United States
[3] Department of Astronomy, University of Geneva, ch. d'Ecogia 16, 1290 Versoix, Switzerland
[4] Department of Physics, University of Crete, 71003 Heraklion, Greece
[5] Institute of Astrophysics, Foundation for Research and Technology – Hellas, Voutes, 70013 Heraklion, Greece
[6] Institut de Radioastronomie Millimétrique, Avenida Divina Pastora 7, Local 20, 18012 Granada, Spain
[7] INAF – Istituto di Radioastronomia, Via Gobetti 101, 40129 Bologna, Italy
[8] INAF Osservatorio Astronomico di Brera, Via E. Bianchi 46, 23807 Merate (LC), Italy
[9] Saint Petersburg State University, 7/9 Universitetskaya nab., St. Petersburg 199034, Russia
[10] Center for Astrophysics – Harvard & Smithsonian, 60 Garden Street, Cambridge, MA 02138, USA

Received 25 February 2024 / Accepted 15 May 2024

ABSTRACT

Context. The blazar AO 0235+164, located at redshift $z = 0.94$, has displayed interesting and repeating flaring activity in the past, with recent episodes in 2008 and 2015. In 2020, the source brightened again, starting a new flaring episode that peaked in 2021.
Aims. We study the origin and properties of the 2021 flare in relation to previous studies and the historical behavior of the source, in particular the 2008 and 2015 flaring episodes.
Methods. We analyzed the multiwavelength photo-polarimetric evolution of the source. From Very Long Baseline Array images, we derived the kinematic parameters of new components associated with the 2021 flare. We used this information to constrain a model for the spectral energy distribution of the emission during the flaring period. We propose an analytical geometric model to test whether the observed wobbling of the jet is consistent with precession.
Results. We report the appearance of two new components that are ejected in a different direction than previously, confirming the wobbling of the jet. We find that the direction of ejection is consistent with that of a precessing jet. Our derived period agrees with the values commonly found in the literature. Modeling of the spectral energy distribution further confirms that the differences between flares can be attributed to geometrical effects.

Key words. accretion, accretion disks – astroparticle physics – polarization – radiation mechanisms: general – relativistic processes – galaxies: jets

1. Introduction

Blazars, a type of active galactic nucleus (AGN), are amongst the most energetic objects in the Universe. They are generally accepted to consist of a supermassive black hole (BH) surrounded by an accretion disk and usually a dusty torus (DT), with symmetrical jets of matter emanating from the vicinity of the BH that can extend far beyond the size of its host galaxy. The exact mechanisms by which high-energy emission from blazars is generated are not well understood, and questions remain about the exact mechanisms by which plasma in the jet is collimated and accelerated to speeds close to that of light, as well about the particle composition of the jet and the location and cause of the observed variability and γ-ray emission.

AO 0235+164 is a BL Lacertae-type blazar located at redshift $z = 0.94$ (Cohen et al. 1987). It exhibits strong variability across the entire spectrum, and has repeatedly displayed high-amplitude flaring behavior in recent years. In particular, episodes in 2008 (Agudo et al. 2011) and 2015 (Escudero et al. 2024), which received extensive multiwavelength (MWL) coverage, displayed significant similarities: significant correlations and short delays between emission at different bands, X-ray spectrum features beyond the absorption expected from our Galaxy (Madejski et al. 1996), and the association of flaring episodes with the appearance of superluminal components in very long baseline interferometry (VLBI) images of the source, among others (Agudo et al. 2011; Escudero et al. 2024).

The similar time span between these episodes, together with older studies of the source (Raiteri et al. 2005) that reported flares in previous decades (1992, 1998), hints at a pseudo-periodic behavior with a characteristic timescale of 6–8 years (Otero-Santos et al. 2023). A similar timescale was suggested by Ostorero et al. 2004, who explained the nearly periodic long-term variability at lower frequencies with a helical model of the jet that precisely matched most of the flares at 8 GHz between 1975–2000 with a period of almost 6 years. The predicted flare in 2004, however, failed to occur, although a period of stronger variability started that peaked in early 2006 and culminated in the historic peak of October 2008. So far, all attempts at uncovering a significant and clear periodicity in the emission of

⋆ Corresponding author; jescudero@iaa.es

AO 0235+164 have failed: the emission, albeit repeating and presenting striking similarities each time, is not periodic (i.e., there is no precise delay or close resemblance between different periods). On the other hand, the flares are a recurrent phenomenon, and the existence of a characteristic timescale for the system related to the apparent delay of 6–8 years between flares cannot be discarded. In this regard, there might be other hints of periodic or pseudo-periodic behavior in this source.

We present data from the most recent flare of AO 0235+164, which occurred in 2021, extending the dataset from Escudero et al. (2024) by 4 years, from 2019 to 2023. The new episode confirms the relationship between flares in the different spectral ranges, the appearance of superluminal components in VLBI images, and the changing direction of the propagation of these components. The timing of this new flare and its detailed characteristics, which we present here, further strengthen the hypothesis of a pseudo-periodic behavior.

For this work we used a standard flat ΛCDM cold dark matter cosmological model with Hubble constant H_0 = 67.66 km/Mpc, as given by Planck Collaboration VI (2020).

2. Observations

The new dataset presented in this study extends in time by about three years the one in Escudero et al. (2024), and includes 7mm (43 GHz) Very Long Baseline Array (VLBA) images from the Boston University blazar monitoring program (VLBA-BU-BLAZAR and BEAM-ME programs), reduced both for total flux density and polarization using AIPS (see Weaver et al. 2022); single-dish photo-polarimetric data at 1 mm and 3 mm from the POLAMI[1] program at the IRAM 30m Telescope (Agudo et al. 2017a; Thum et al. 2017; Agudo et al. 2017b); photometric data at 1mm and 0.8μm from the Submillimeter Array (SMA), including photo-polarimetric data at 1mm from the SMAPOL program (see Appendix A for details); 8mm observations from the Metsähovi Radio Observatory, and optical data from the Calar Alto (2.2 m Telescope) under the MAPCAT program and from the Perkins Telescope Observatory (1.8 m Telescope). Gamma-ray data in the 0.1–200 GeV range come from the *Fermi*/Large Area Telescope. The historical light curve shown in Figure 1 also contains previously published optical data from the Crimea Observatory AZT-8 (0.7 m Telescope) and the St. Petersburg State University LX-200 (0.4 m Telescope), as well as ultraviolet data from the *Swift*/UVOT instrument, X-ray data in the 2.4–10 keV range from the RXTE satellite, and in the 0.2–10 keV energy range from *Swift*/XRT (see Escudero et al. 2024 for details).

We followed the procedure described in Blinov & Pavlidou (2019) to overcome the ±180° polarization angle ambiguity in our *R*-band measurements, minimizing the difference between successive measurements while also taking into account their uncertainty. We also shifted clusters of close observations by an integer multiple of 180° to match the angle reported at 3mm, enabling a visual comparison of the joint evolution of the optical and millimeter range polarization angles, while maintaining the short time evolution intact. Data from the infrared to the ultraviolet bands were corrected following the prescription by Raiteri et al. (2005) and the updated values by Ackermann et al. (2012). This correction accounts for the local Galactic extinction at $z = 0$ and the intervening galaxy ELISA at $z = 0.524$, as well as for ELISA's contribution to the observed emission. Details about the correction to the X-ray present in the historical light curve are available in Escudero et al. (2024).

[1] https://polami.iaa.es

3. Analysis and results

3.1. Multiwavelength flux and polarization behavior

In Figure 1 we present the MWL light curves consisting of our compiled data in the millimeter, optical, and high-energy ranges from 2008 to 2023. This period includes the three recent flaring episodes of the source in 2008, 2015 and 2021. A detailed view into the last of these flaring episodes can be found in Figure 2. During the flare, emission at all wavelengths experienced an increase, from millimeter-wave to high-energy γ-rays, as happened in previous flaring episodes. Compared to previous flares of the source, the 2021 flare was weaker, following a trend that started with the 2015 episode. In agreement with past episodes, the light curve during the 2021 flare shows a multi-peak structure, with sharper variability at higher energies.

The evolution of both the linear polarization degree and the polarization angle at all wavelengths are shown in Figures 3 and 4, respectively. The polarization degree also increased during the episode, from $p_{L,\mathrm{R}} = 10.0 \pm 6.0\%$ and $p_{L,3\mathrm{mm}} = 3.0 \pm 1.4\%$ in the time spanned from 2018 to 2019 to $p_{L,\mathrm{R}} = 12.5 \pm 6.3\%$ and $p_{L,3\mathrm{mm}} = 3.7 \pm 2.0\%$ from 2019 to 2023, although this increase was not as dramatic as in the previous flaring episodes (Escudero et al. 2024). In contrast to the 2015 episode, the polarization angle at 3mm remained more stable, with no clear rotations apparent in the available data.

3.2. VLBA imaging

We analyzed a total of 49 new VLBA 7mm (43 GHz) images of AO 0235+164, extending the dataset presented in Escudero et al. (2024) by about 4 years. In our new VLBI images, the most recent flare is accompanied by the ejection of newly emerged components B8 and B9, as can be seen in Figure 5 for some selected epochs. These components move away from the compact, stationary region present at all epochs known as the "core". As in our previous studies, these components were obtained by fitting the reduced VLBA total flux maps to circular Gaussian components in the (u, v) plane using `Difmap`. After model fitting of the most prominent jet features, we cross-identified them along the different observing epochs. This was done for all new 49 observing epochs. Their resulting flux and polarization evolution is shown in Figures 3 and 4, together with that of the core region (labeled as component A0) and the total integrated emission from the source at 7mm.

The connection between the MWL flare and the ejection of superluminal components in VLBA images at 7mm is confirmed here for the 2021 flare, as was also found for the 2006–2008 flare(s), which was accompanied by the appearances of components B1 and B2, and for the 2015 flare, when components B5, B6, and B7 were ejected. We observe that the increase in brightness of the core (A0) begins almost a year before the new B8 component can be differentiated, although the polarization angle is already aligned with the future direction of B8. This alignment is maintained for most of the lifetime of the component, except for short rotations just after its ejection. This behavior was also reported previously for the superluminal components associated with the 2008 and 2015 flares, and also for components B3 and B4 during the quiescent period in between those two flares (Escudero et al. 2024).

Remarkably, the direction of propagation of these new components is very different from that of traveling components identified previously in AO 0235+164 with the VLBA at 7mm. In

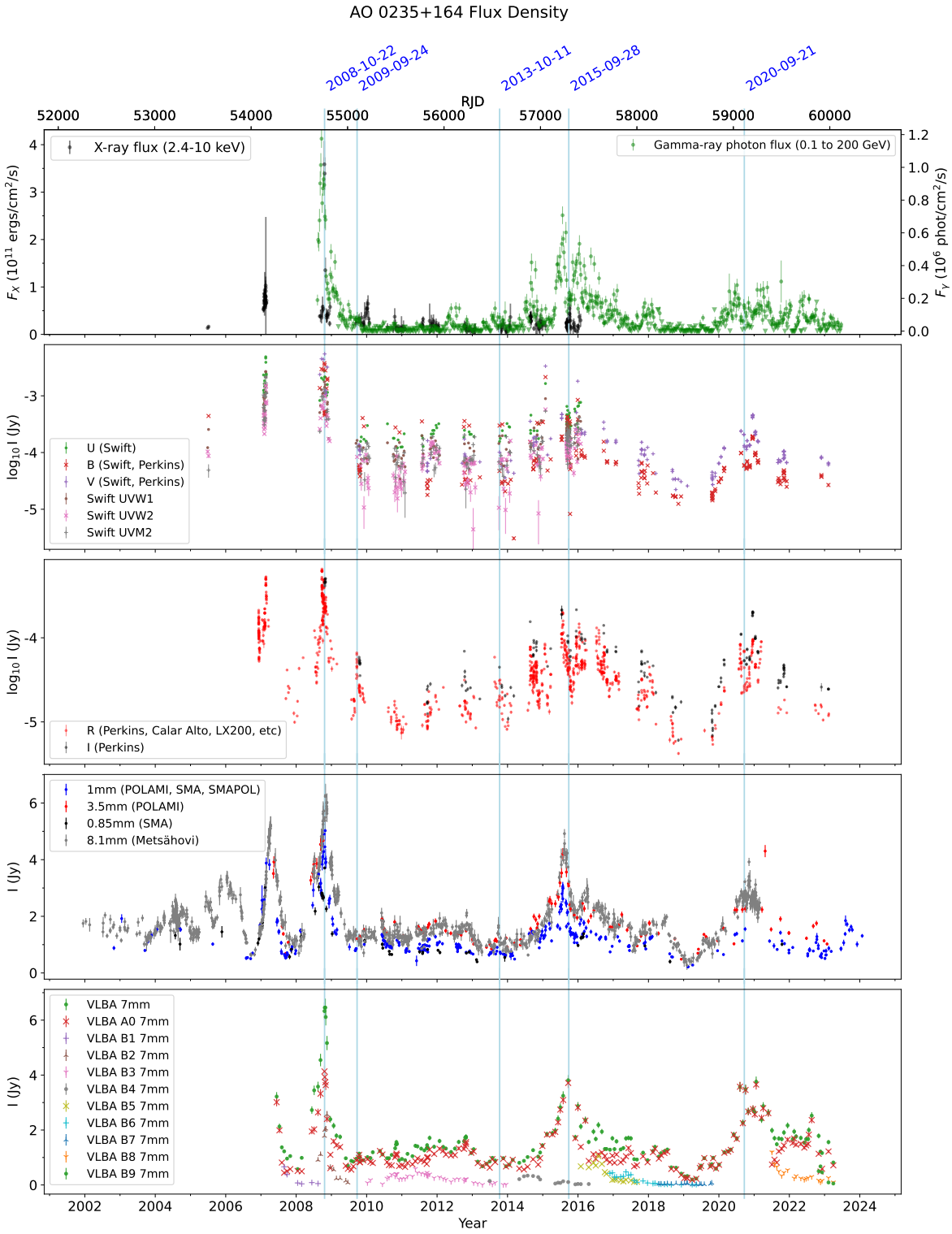

Fig. 1. Historical light curves of AO 0235+164 at different wavelengths. The first four vertical lines mark the epochs analyzed in Escudero et al. (2024); the last one corresponds to the epoch analyzed in Sect. 3.6.

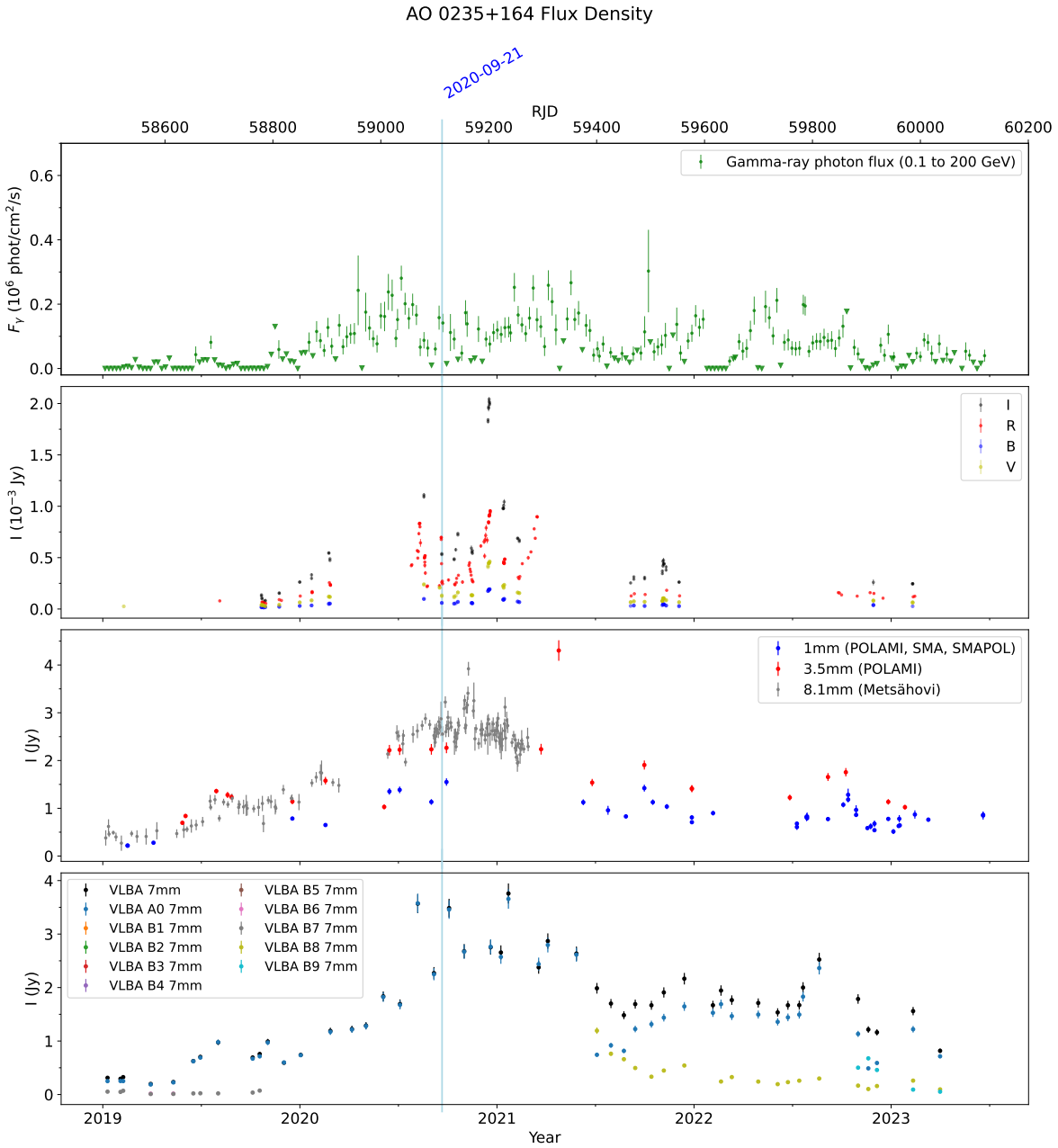

Fig. 2. Zoomed-in view of the flux evolution of AO 0235+164 at different wavelengths in 2019–2923. The vertical line corresponds to the last marked date in Fig. 1.

fact, it has been the case for AO 0235+164 that the direction of ejection has consistently changed from one episode to the next: B1 (111 ± 3°), B2 (−72 ± 16°), B3 (−73 ± 10°) , B4 (153 ± 21°), B5 (29 ± 4°), B6 (40 ± 10°), B7 (70 ± 10°), B8 (147 ± 8°), and B9 (144 ± 8°). The new flare and its associated traveling components confirm the wobbling of the jet and its narrow viewing angle. A very low viewing angle of the jet is necessary for any reasonably small change in its direction to produce such radical changes in the direction on the sky of propagation of the superluminal components.

3.3. Kinematic parameters of the VLBI jet components

We computed the kinematic parameters of the new B8 component following the procedure described in Weaver et al. (2022), as was done in Escudero et al. (2024) for B1 to B6. The procedure involved tracing the identified features in the VLBA images across all new epochs and fitting their positions to a linear function to obtain their speed (v_r) and time of ejection (t_0), as well as fitting their fluxes to a decaying exponential to obtain the timescale of variability ($t_{\rm var}$). This allowed us to compute

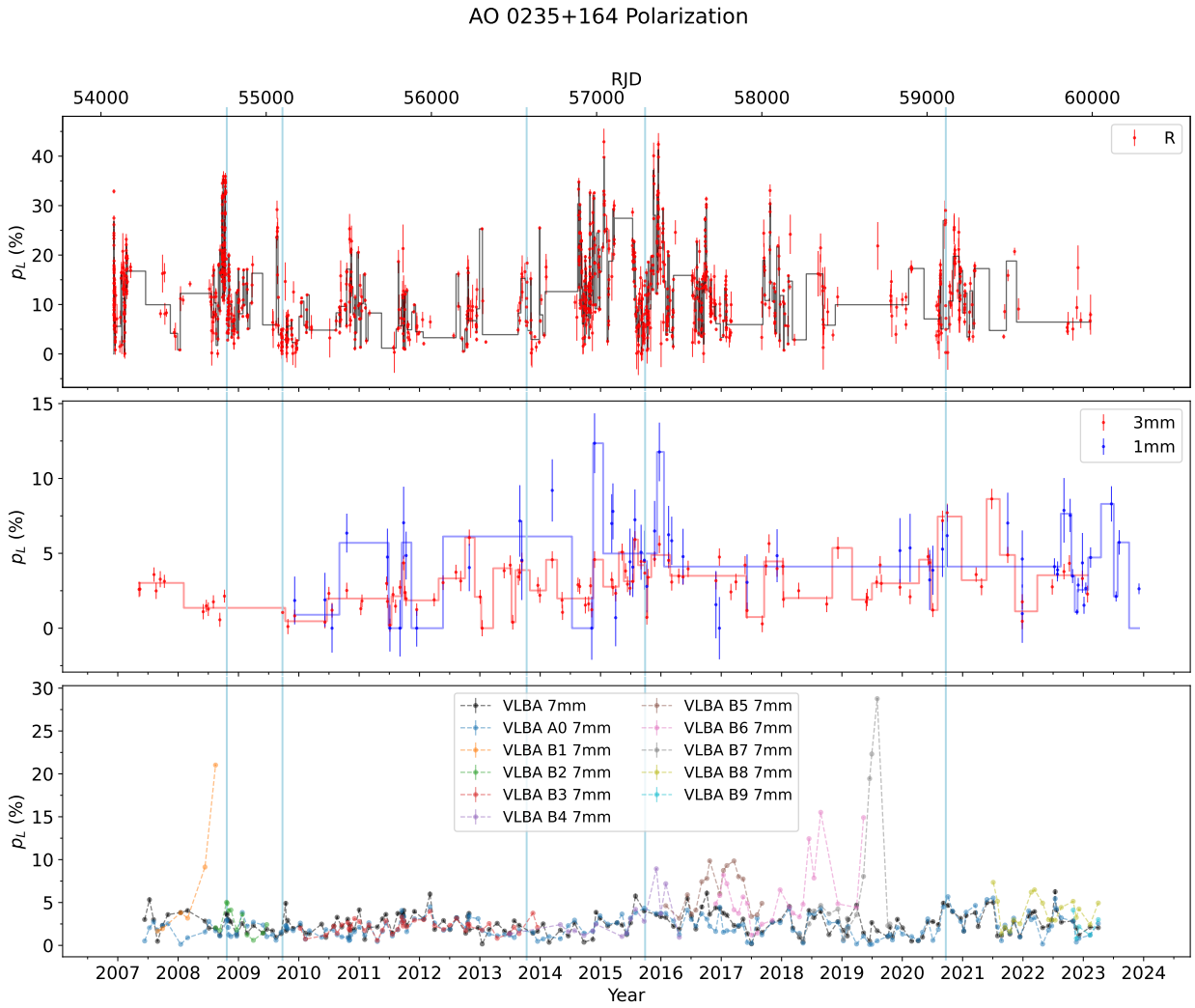

Fig. 3. Historical evolution of the polarization degree of AO 0235+164. A Bayesian block representation is shown superimposed for R at 99.9% confidence and for 1mm and 3mm at 90% confidence. Vertical lines corresponds to the dates marked in Fig. 1.

their Doppler factor δ and apparent speeds $\beta_{\rm app}$ (Jorstad et al. 2005; Casadio et al. 2015). From these, the corresponding bulk Lorentz factors, Γ, and viewing angles, Θ, could be computed using the usual expressions. As was the case for B7 during the previous flare, the kinematic parameters of B9 could not be correctly estimated due to the low number of observations, and only the time of ejection could be computed for B7 and B9. The fits to the position and flux of B8 can be found in Figure 6. For B8, we obtained a time of ejection $t_0 = 2020.0 \pm 0.2$ year, Doppler factor $\delta_{\rm var} = 25.5 \pm 1.5$, apparent speed $\beta_{\rm app} = 6.7 \pm 1.0$, bulk Lorentz factor $\Gamma = 13.6 \pm 1.7$ and viewing angle $\Theta = 1.1 \pm 0.2°$. These results are in agreement with those found in Escudero et al. (2024). The Doppler factor of B8, the main ejected component responsible for the 2021 flare, is much lower than that of B2 for the 2008 flare ($\delta = 67.8 \pm 3.6$) and B5 for the 2015 flare ($\delta = 39.8 \pm 2$), explaining the relatively diminished luminosity of each flare as a consequence of weaker Doppler boosting.

3.4. Change in jet direction

To try to explain the observed wobbling of the jet, we used the derived times of ejection of the superluminal components and their direction of propagation to test for signs of a precessing jet by fitting to an analytical model for the angle of propagation. If we assume that the ejection happens at approximately constant distance from the base of the jet, this location, when projected in the plane of the sky, must trace an ellipse for which the eccentric anomaly E is given by the precessed angle, $E = \omega t$. The eccentricity of this ellipse will be given by the angle between the axis of precession and the observer. In arbitrary units, the semi-axes of this ellipse can be taken to be $a = 1$ and $b = \cos\varphi$. In the plane of the sky, the center of this ellipse will be displaced with respect to the basis of the jet by a distance $d \sin\varphi$, and the major semi-axis will form an arbitrary angle, ψ, with regard to the x-axis. The polar coordinate of this region orbiting along the ellipse with respect to the basis of the jet is the observed angle of propagation

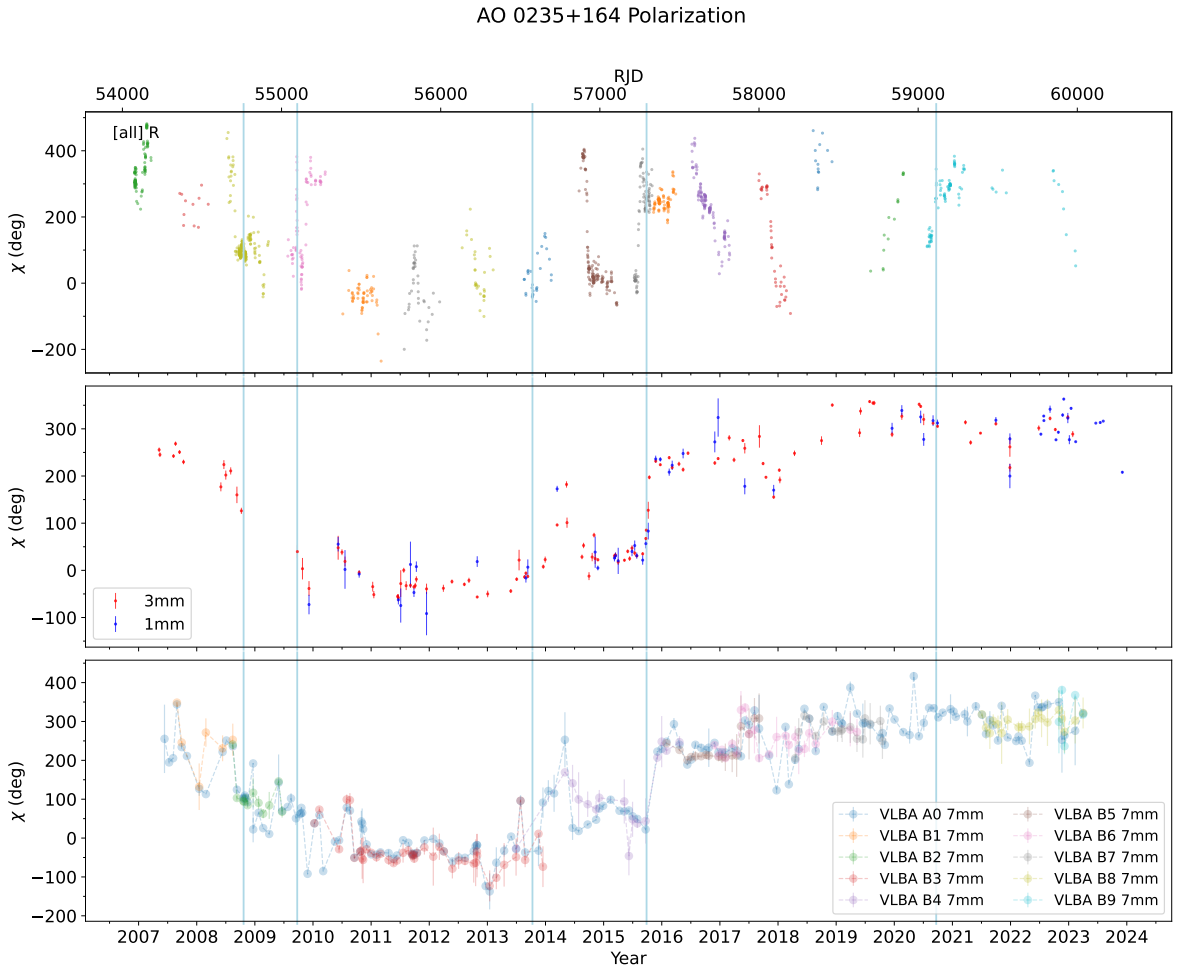

Fig. 4. Historical evolution of the polarization angle of AO 0235+164. Vertical lines correspond to the dates marked in Fig. 1. All points in the first panel correspond to the *R* band; the different colors denote the clusters that were shifted by $n \times 180^\circ$ to follow the evolution of the polarization angle at 3mm, as discussed in Sect. 2.

of the superluminal component. If the angle between the precession axis and the observer is high enough compared to the tilt of the jet with regard to the precession axis, the jet will have a definite direction in the sky, and all components will be emitted in the span of some arc. When the jet is narrowly pointing toward us, even for small precession angles, the superluminal components will appear to propagate in all directions. This would be the case for AO 0235+164.

Figure 7 shows the result of simultaneously fitting $(t_0, \cos\theta)$ and $(t_0, \sin\theta)$, where θ is the propagation angle of a component. This fit was preferred to directly fitting the angle θ because it removes any ambiguity in the position angle. The uncertainties in the parameters were computed using a Monte Carlo approach. Only components B2 to B8 were used for the fit, on the basis of selecting only those with a significant number of epochs to compensate for the high uncertainties in the positions of the fitted Gaussian features mentioned in Sect. 3.2. We examined the impact of considering all components in the fit and concluded that the optimal fit values were comparable, despite a significant increase in the model uncertainties. The resulting best-fit model has a period of $T = (6.0 \pm 0.1)$ years, which is within the range of periods proposed in the literature. The obtained eccentricity of the ellipse gives an angle of $\phi = 0.11^\circ$ for the hypothetical precession axis with regard to the observer, although this value is not well constrained by our fit. Because of the low number of points and the significant uncertainties in the times of ejection of jet features, usual fit statistics such as the p-value are not suitable to reaffirm or reject our hypothesis, and therefore do not allow us to claim precession in AO 0235+164. Nevertheless, we find it interesting to examine Figures 7 and 8, where it can be seen that most of the points fall inside the 3σ region when accounting for their uncertainties. We propose that the model might be used to affirm or discard the hypothesis of precession when more data become available in subsequent decades. We also emphasize that the value for the period found in this analysis, derived from the propagation angle of superluminal components, is independent of the periods suggested in the literature (Otero-Santos et al. 2023; Raiteri et al. 2005; Ostorero et al. 2004), which are derived from analysis of variations in the light curves. They nevertheless agree within their uncertainties. The small value obtained for the possible precession axis relative to the line of sight, together with the viewing

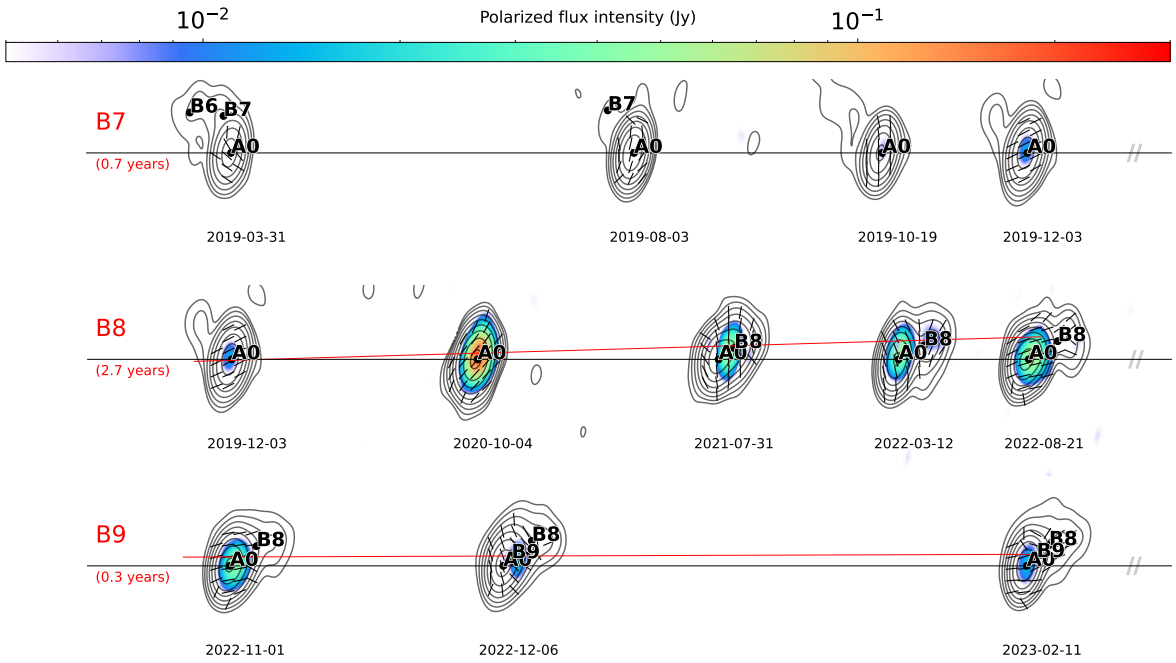

Fig. 5. Selected epochs illustrating the evolution of the last three identified components, B7, B8, and B9. The figure shows the total intensity (contours), polarized flux intensity (color sale), and polarization direction (black line segments). The horizontal black line marks the position of the core, A0. The red line in each row is a linear fit to the knot position, present for all except B7 due to its low flux. For each row, the spacing between plots is proportional to the elapsed time, with the total time indicated in parentheses. The full temporal evolution is available as an online movie.

angles obtained in the kinematic analysis (Sect. 3.3), is also in agreement with the observed behavior of the jet, which ejects components in completely different directions.

3.5. Correlations across the spectrum

We computed the correlations between the light curves at different wavelengths using `MUTIS` [2]. We used the normalized discrete correlation function (DCF) proposed by Welsh (1999), which applies normalization and binning, making it suitable for our irregularly sampled signals. A uniform bin size of 20days was used, a value that was chosen to allow for enough bin statistics without smoothing the correlations too much. To validate our choice, the same results were derived using binning sizes from 10 days to 30 days, confirming the consistency of our results. The significance of the correlations was estimated using a Monte Carlo approach, generating $N = 2000$ synthetic light curves for each signal. Randomization of the Fourier transform was used for millimeter wavelengths, generating light curves with similar statistical properties and power-spectrum density (PSD). For optical and γ-ray data we modeled the signals as Orstein-Uhlenbeck stochastic processes (Tavecchio et al. 2020), which better reproduces the qualitative shape of these signals. The uncertainties of the correlations were estimated using the uncertainties of the signals, again with a Monte Carlo approach. We find high and significant correlations between emission from all bands except X-rays (Fig. 9), for which correlation was generally lower and found only at 2σ with some bands. This is in agreement with our previous results (Escudero et al. 2024) that found decreased correlation for the X-ray band and attributed it to a different emission mechanism located at a different region. Nonetheless, the achieved significance of those correlations involving X-rays are generally higher than those previously found, thanks to the improved dataset. This is especially the case for the correlation between X-rays and 1mm, where no significant correlation was previously found. This decreased correlation for the X-ray is also expected from the spectral energy distribution modeling presented in Sect. 3.6 and that of Escudero et al. (2024), where the bulk Compton emission dominates the X-rays in its high state, while in its low state it is dominated by the same region responsible for emission in other bands. Regarding correlations restricted only to the last episode (2019–2023), the new flare is too weak and data too sparse to produce any meaningful correlations, which are dominated by noise, so they have been omitted here.

Analysis of the PSD of the signals was performed using the Lomb-Scargle periodogram (Lomb 1976; Scargle 1982), suitable for our unevenly sampled light curves. The resulting power spectra locate the peak frequencies of the 1mm, 3mm, 7mm, 8mm, and R-band light curves at equivalent timescales of 5.7, 5.4, 5.1, 4.2, and 6.8 years, respectively (Fig. 10). Computed false-alarm probabilities are close to zero in all cases ($\ll$0.1%). The interpretation of this probability is subtle (VanderPlas 2018), but instead hints at a low probability of a purely stochastic process, since it represents the probability of a purely noise signal producing a peak higher than ours. The derived timescales agree with those suggested in the literature (Otero-Santos et al. 2023; Raiteri et al. 2005; Ostorero et al. 2004) and with the one independently obtained in Sect. 3.4.

[2] MUltiwavelength TIme Series. A Python package for the analysis of correlations of light curves and their statistical significance. https://github.com/IAA-CSIC/MUTIS

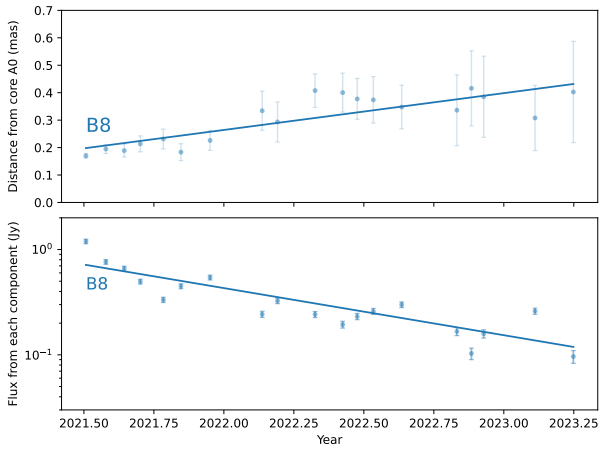

Fig. 6. Observed distance from the core (top) and flux density (bottom) for the newly identified component, B8, together with the linear weighted fit to the flux knot position and the logarithmic fit to the knot flux used in the computation of the kinematic parameters.

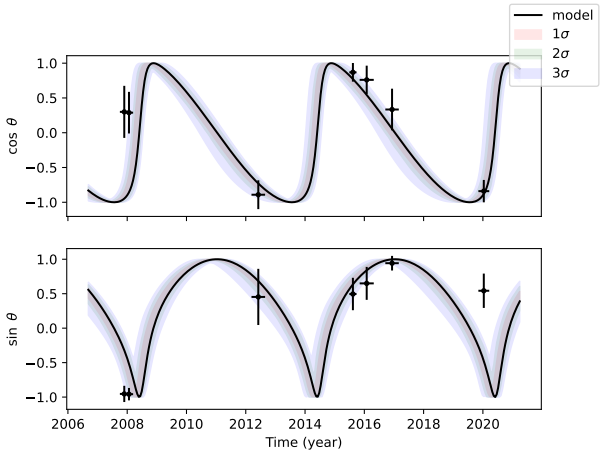

Fig. 7. Simultaneous fit to the sine and cosine of the average position angle, θ, of the identified VLBI jet features as a function of their computed time of ejection. Most of the points lie within the 3σ model uncertainty region. The simultaneous fit avoids the ± 180 uncertainty in the position angle. The corresponding plot for the position angle, θ, can be found in Fig. 8.

3.6. Spectral energy distribution

Unlike for previous flares, no *Swift* XRT or UVOT data are available during the flaring period in 2021. The night with the broadest MWL coverage (MJD 59113, October 20, 2020) was selected to perform a spectral energy model of the source.

We modeled the emission using the JetSeT framework (Tramacere 2020; Tramacere et al. 2011, 2009) using both a single-zone synchrotron self-Compton (SSC) scenario and an SSC plus external Compton (EC) scenario. The common physical setup consists of a spherical emitting region formed by a population of relativistic electrons of radius R at a distance R_H from the central BH that moves at a small angle, θ, to the line of sight with a bulk Lorentz factor, Γ. Synchrotron radiation is emitted through interaction of the relativistic electrons with the jet magnetic field, B. These same synchrotron photons and electrons interact by inverse Compton scattering to produce high-energy photons (SSC). In the EC scenario, additional radiation is produced from inverse Compton scattering of photons coming from a disk torus (disk) and broad line region (BLR) surrounding the BH. The electron energy distribution is assumed to be well described by a power law with a cutoff (PLC):

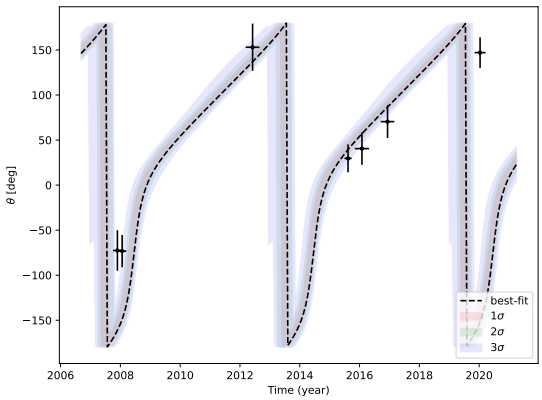

Fig. 8. Observed ejection angles of the identified VLBI components B2-B8 with respect to their computed time of ejection, together with the best-fit model. The shaded areas represent the 1σ (68.27%), 2σ (95.45%), and 3σ (99.73%) uncertainties of the model.

$$n(\gamma) = N\gamma^{-p} \exp \frac{\gamma}{\gamma_{\rm cutoff}}, \gamma_{\rm min} \leq \gamma \leq \gamma_{\rm max}, \quad (1)$$

where p is the spectral index and γ is the electron Lorentz factor. A broken power law was also attempted, but the resulting fit was systematically worse, consistent with the results of Escudero et al. (2024), and therefore we only show the model with the PLC distribution.

In the single-zone SSC scenario, it was found that the region of emission was best described as having a radius $R = 2.77^{+0.18}_{-0.17} \times 10^{18}$ cm, situated at a distance $R_H = 9.3 \times 10^{19}$cm with a bulk Lorentz factor $\Gamma = 14.0^{+0.9}_{-1.2}$, and a viewing angle of $\theta = 0.89^{\circ}{}^{+0.12}_{-0.16}$, while the electron distribution was best modeled as having a spectral index $p = 1.47^{+0.08}_{-0.07}$, and minimum and maximum Lorentz factors of $\gamma_{\rm min} = 105^{+15}_{-15}$, $\gamma_{\rm max} = 1.72^{+0.3}_{-0.3} \times 10^{+5}$, and a cutoff of $\gamma_{\rm cut} = 7.7^{+0.5}_{-0.5} \times 10^{+3}$. The best-fit value for the magnetic field was $B = 3.6^{+0.4}_{-0.4} \times 10^{-3}$ G. All values reported are best-fit values, with 1σ asymmetric errors computed using Markov chain Monte Carlo approach. The result has been represented in Fig. 11. The obtained parameters are in agreement with those obtained by Escudero et al. (2024), and the resulting bulk Lorentz factor, viewing angle, and Doppler factor ($\delta = 25$) agree precisely with those obtained in the kinematic analysis of section 3.3 within their uncertainties.

In the EC scenario, the disk, DT, and BLR parameters were frozen. The disk was assumed to have luminosity $L_{\rm Disk} = 5 \times 10^{45}$ erg s^{-1}, accretion efficiency $\eta = 0.08$, and inner and outer radii $R_{\rm Disk,\,in} = 3R_{\rm s}$ and $R_{\rm Disk,out} = 300R_{\rm s}$, respectively. The DT temperature was fixed to $T_{\rm DT} = 830$K, its radius determined by the phenomenological relation $R_{\rm DT} = 2 \times 10^{19} L^{1/2}_{\rm Disk,46}$ cm (Cleary et al. 2007), with reprocessing factor $\tau_{\rm DT} = 0.1$. The BLR was modeled as a thin spherical shell with an internal radius as provided by the phenomenological relation $R_{\rm BLR,in} = 3 \times 10^{17} L^{1/2}_{\rm Disk,46}$ cm (Kaspi et al. 2007) and its outer radius was

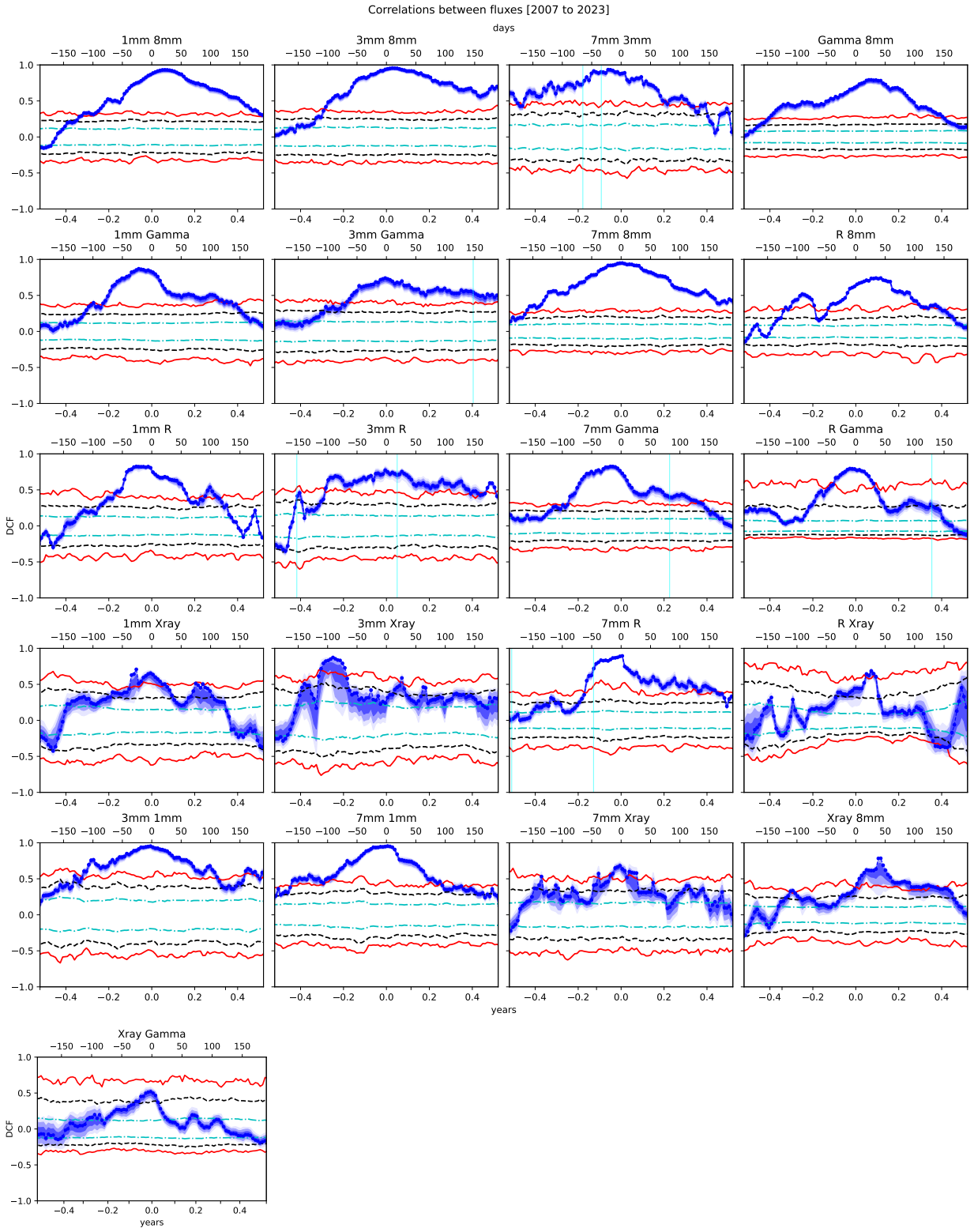

Fig. 9. Correlations between fluxes at all wavelengths. Horizontal lines represent the 1σ, 2σ, and 3σ significance levels and were computed using a Monte Carlo approach with $N = 2000$ synthetic light curves. We find clear and significant ($>3\sigma$) correlations near zero between all bands except for the X-ray.

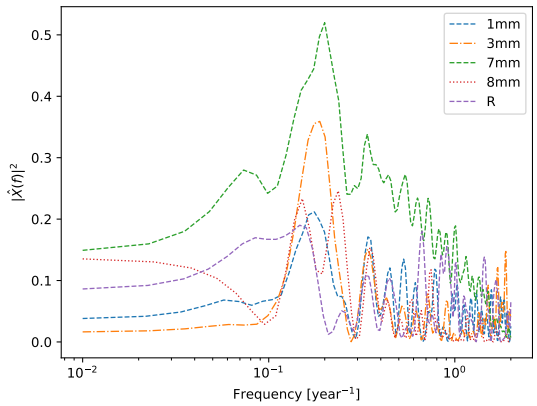

Fig. 10. Normalized PSD computed using the Lomb-Scargle periodogram for the 1mm, 3mm, 7mm, 8mm, and *R* light curves, showing peak frequencies corresponding to characteristic timescales of 5.7, 5.4, 5.1, 4.2, and 6.8 years, respectively. These timescales are mostly in agreement with the 5–8 year timescale found in previous works. The false alarm probability in all cases is close to zero ($\ll$0.1%), meaning that there is a very low probability that such a peak would be caused by a pure noise signal.

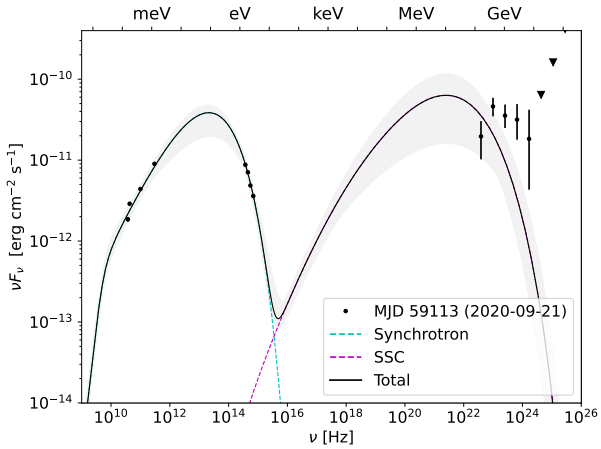

Fig. 11. Spectral energy distribution from September 21, 2023, together with the best fit of the one-zone SSC model discussed in Section 3.6. The gray area represents the 3σ uncertainty region. The downward pointing triangles represent upper limits.

assumed to be $R_{\rm BLR,out} = 1.1R_{\rm BLR,in}$, with a coverage factor $\tau_{\rm BLR} = 0.1$. The mass of the BH was set to $M_{\rm BH} = 5 \times 10^8\ M_\odot$.

Two alternative SSC+EC models were produced, one allowing Γ and θ to vary freely and the other fixing them to the values obtained from the kinematic analysis. In the former case, the emitting region was best described by best-fit values $\theta = 1.68^{+0.08}_{-0.04}$ °, $\Gamma = 50^{+1.55}_{-5.75}$, $B = 5.3^{+0.5}_{-0.3} \times 10^{-2}$ G, $N = 113^{+10}_{-10}$cm^{-3}, $\gamma_{\rm min} = 1.12^{+0.12}_{-0.06}$, $\gamma_{\rm max} = 6.48^{+0.3}_{-0.6} \times 10^5$, $\gamma_{\rm cut} = 1.83^{+0.9}_{-0.1} \times 10^3$, and $p = 1.50^{+0.11}_{-0.03}$. In the latter, fixing $\Gamma = 13.6$ and $\theta = 0.9°$, we obtained $B = 2.59^{+0.05}_{-0.05} \times 10^{-2}$ G, $N = 88.4^{+0.2}_{-0.2}$cm^{-3}, $\gamma_{\rm min} = 9.17^{+0.02}_{-0.02}$, $\gamma_{\rm max} = 3.48^{+0.08}_{-0.07} \times 10^4$, $\gamma_{\rm cut} = 4.27^{+0.08}_{-0.08} \times 10^3$, and $p = 1.94^{+0.004}_{-0.004}$. The higher bulk Lorentz factor in the first cause with respect to that measured at the VLBI case might be attributed to deceleration. The results have been represented in

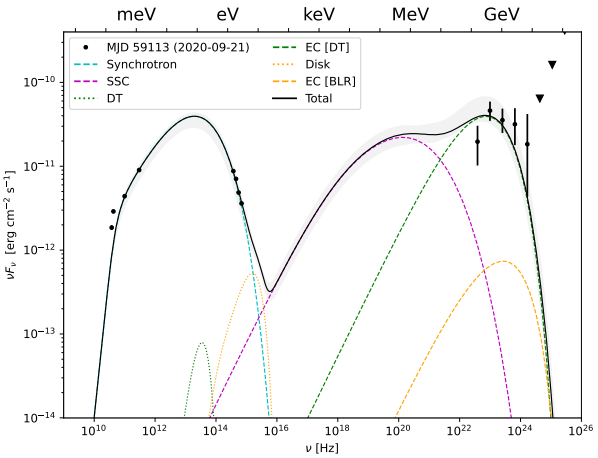

Fig. 12. Spectral energy distribution from September 21, 2023, together with the best fit of the SSC+EC model with freely varying Γ and θ as discussed in Section 3.6. The gray area represents the 3σ uncertainty region. The downward pointing triangles represent upper limits.

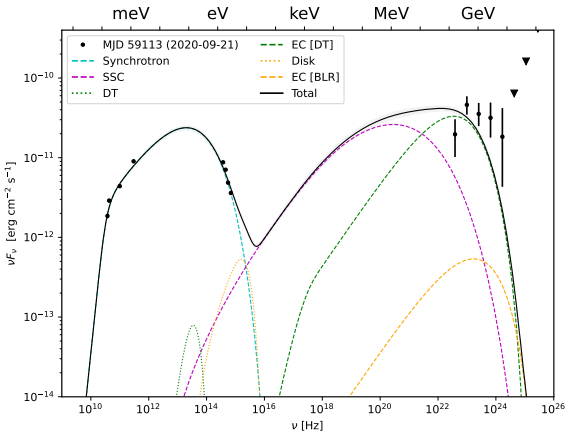

Fig. 13. Spectral energy distribution from September 21, 2023, together with the best fit of the SSC+EC model with fixed Γ and θ as discussed in Section 3.6. The gray area represents the 3σ uncertainty region. The downward pointing triangles represent upper limits.

Figs. 12 and 13. In any case, for all models the resulting Doppler factors are lower than that obtained for the flaring epochs in the 2008 ($\delta = 37$) and 2015 ($\delta = 32$) episodes (Escudero et al. 2024), which consistently explains the lower apparent luminosities of the successive flares as caused, at least partially, by relativistic effects.

4. Discussion and conclusions

We have presented new and updated data from the blazar AO 0235+165, extending previous works to cover its most recent flaring episode, which peaked in 2021.

The new flare is again associated with the appearance of two new components in 7mm VLBA images, B8 and B9. The behavior of B9 and B8 is compatible with that of trailing components (Agudo et al. 2001), as was the case with B6 and B5 during the 2015 episode. This can be interpreted in the context of a shock-in-jet model, in agreement with the alignment of the polarization

angle in the direction of the jet axis that begins during the core re-brightening phase (Fig. 5). The two newly identified components, B8 and B9, propagate in a different direction compared to previous components, confirming the wobbling of the jet.

We have proposed a purely geometrical model that aims to explain the observed changes in the direction of the ejection of the VLBI components as the result of a precessing jet. We have found that the observed position angles and calculated times of ejection are mostly compatible with a jet precessing with a period of 6 years. This value is independently obtained but compatible with those found in the existing literature. Although precession is a strictly periodic phenomenon and no exact periodicity is found in the MWL light curves of AO 0235+164, it is important to keep in mind that the model in Sect. 3.4 relates only to the position angle of the ejected components. However, the periodicity found in this model must indeed have an origin that could justify the timescale of variability – not periodicity – of 6−8 years found in the light curves in previous works (Raiteri et al. 2005; Otero-Santos et al. 2023) and in Sect. 3.5. The absence of a strict periodicity in the flux evolution of the source is to be expected due to the fact that jet emission is a complex process that can be affected by many factors (jet angle, speed, magnetic field, matter accretion, and available energy, to name only a few) and is inherently stochastic. However, the possible origins of wobbling, or jet precession, are more restricted, the most common causes being a binary system (Abraham 2018) or an off-axis accretion disk (Lense-Thirring effect), and this exact periodicity can be distortedly reflected in light curves. A precessing jet with a periodicity of around ∼6 years could explain the pseudo-periodic timescale found in the light curves in previous works.

Modeling of the spectral energy distribution reveals that the emission process is similar to that of previous epochs, both flaring and quiescent (Escudero et al. 2024), with the difference in the Doppler factor explaining at least partially the flux variability. This is the case for all bands but cannot be confirmed in X-rays due to the absence of data during the 2021 flaring episode. However, previous works found that emission in X-rays was caused at least partially by different, uncorrelated mechanisms involving a different emitting region, and that this region was responsible for the bulk of emission when the X-ray emission was in its high state (Ackermann et al. 2012; Escudero et al. 2024). Therefore, more complex models are necessary to fully explain the MWL emission. Moreover, even the aforementioned models fail to include hadronic processes despite increasing evidence of neutrino emission in blazars (IceCube Collaboration 2018).

The re-brightening of the core suggests the existence of a standing shock, with the ejected components that accompany each flaring episode interpreted as trailing components (Agudo et al. 2001). Such stationary shocks can be explained by bends in the jet, which are expected in wobbling jet scenarios, although such bends need not be caused by rotations of the jet nozzle: they can also be the result of dynamical processes. In addition, stationary shocks can be explained by the interaction of the jet with the external medium (Gómez et al. 1997). In any case, the recurrence of the flaring episodes, the wobbling of the jet, and the modeling of the spectral energy distribution suggest the existence of a characteristic timescale of a periodic and geometric origin that must be well characterized to achieve a full understanding of the mechanisms of AO 0235+164 emission.

Data availability

Movie associated with Fig. 5 is available at https://www.aanda.org

Acknowledgements. The IAA-CSIC team acknowledges financial support from the Spanish "Ministerio de Ciencia e Innovación" (MCIN/AEI/10.13039/501100011033) through the Center of Excellence Severo Ochoa award for the Instituto de Astrofísica de Andalucía-CSIC (CEX2021-001131-S), and through grants PID2019-107847RB-C44 and PID2022-139117NB-C44. This research has made use of the NASA/IPAC Extragalactic Database (NED), which is operated by the Jet Propulsion Laboratory, California Institute of Technology, under contract with the National Aeronautics and Space Administration. IRAM is supported by INSU/CNRS (France), MPG (Germany) and IGN (Spain). The VLBA is an instrument of the National Radio Astronomy Observatory, USA. The National Radio Astronomy Observatory is a facility of the National Science Foundation operated under cooperative agreement by Associated Universities, Inc. This study was based (in part) on observations conducted using the 1.8 m Perkins Telescope Observatory (PTO) in Arizona (USA), which is owned and operated by Boston University. The BU group was supported in part by U.S. National Science Foundation grant AST-2108622, and NASA Fermi GI grants 80NSSC23K1507, 80NSSC22K1571 and 80NSSC23K1508. The Submillimeter Array is a joint project between the Smithsonian Astrophysical Observatory and the Academia Sinica Institute of Astronomy and Astrophysics and is funded by the Smithsonian Institution and the Academia Sinica. We recognize that Maunakea is a culturally important site for the indigenous Hawaiian people; we are privileged to study the cosmos from its summit.

References

Abraham, Z. 2018, Nat. Astron., 2, 443
Ackermann, M., Ajello, M., Ballet, J., et al. 2012, ApJ, 751, 159
Agudo, I., Gómez, J.-L., Martí, J.-M., et al. 2001, ApJ, 549, L183
Agudo, I., Marscher, A. P., Jorstad, S. G., et al. 2011, ApJ, 735, L10
Agudo, I., Thum, C., Molina, S. N., et al. 2017a, MNRAS, 474, 1427
Agudo, I., Thum, C., Ramakrishnan, V., et al. 2017b, MNRAS, 473, 1850
Baring, M. G., Böttcher, M., & Summerlin, E. J. 2017, MNRAS, 464, 4875
Blinov, D., & Pavlidou, V. 2019, Galaxies, 7
Casadio, C., Gómez, J. L., Jorstad, S. G., et al. 2015, ApJ, 813, 51
Cleary, K., Lawrence, C. R., Marshall, J. A., Hao, L., & Meier, D. 2007, ApJ, 660, 117
Cohen, R. D., Smith, H. E., Junkkarinen, V. T., & Burbidge, E. M. 1987, ApJ, 318, 577
Escudero, J., Agudo, I., Tramacere, A., et al. 2024, A&A, 682, A100
Gómez, J. L., Martí, J. M., Marscher, A. P., Ibáñez, J. M., & Alberdi, A. 1997, ApJ, 482, L33
Ho, P. T. P., Moran, J. M., & Lo, K. Y. 2004, ApJ, 616, L1
IceCube Collaboration (Aartsen, M. G., et al.) 2018, Science, 361, eaat1378
Jorstad, S. G., Marscher, A. P., Lister, M. L., et al. 2005, AJ, 130, 1418
Kaspi, S., Brandt, W. N., Maoz, D., et al. 2007, ApJ, 659, 997
Lomb, N. R. 1976, Ap&SS, 39, 447
Madejski, G., Takahashi, T., Tashiro, M., et al. 1996, ApJ, 459, 156
Ostorero, L., Villata, M., & Raiteri, C. M. 2004, A&A, 419, 913
Otero-Santos, J., Peñil, P., Acosta-Pulido, J. A., et al. 2023, MNRAS, 518, 5788
Planck Collaboration VI. 2020, A&A, 641, A6
Primiani, R. A., Young, K. H., Young, A., et al. 2016, J. Astron. Instrum., 5, 1641006
Raiteri, C. M., Villata, M., Ibrahimov, M. A., et al. 2005, A&A, 438, 39
Scargle, J. D. 1982, ApJ, 263, 835
Shaw, R. A., Payne, H. E., & Hayes, J. J. E. 1995, ASP Conf. Ser., 77, 433
Tavecchio, F., Bonnoli, G., & Galanti, G. 2020, MNRAS, 497, 1294
Thum, C., Agudo, I., Molina, S. N., et al. 2017, MNRAS, 473, 2506
Tramacere, A. 2020, JetSeT: Numerical modeling and SED fitting tool for relativistic jets, Astrophysics Source Code Library [record ascl:2009.001]
Tramacere, A., Giommi, P., Perri, M., Verrecchia, F., & Tosti, G. 2009, A&A, 501, 879
Tramacere, A., Massaro, E., & Taylor, A. M. 2011, ApJ, 739, 66
VanderPlas, J. T. 2018, ApJS, 236, 16
Weaver, Z. R., Jorstad, S. G., Marscher, A. P., et al. 2022, ApJS, 260, 12
Welsh, W. F. 1999, PASP, 111, 1347

Appendix A: SMAPOL observations

The SMA (Ho et al. (2004)) was used to obtain polarimetric millimeter radio measurements at 1.3 mm (230 GHz) within the framework of the SMAPOL (**S**MA **M**onitoring of **A**GNs with **POL**arization) program. SMAPOL follows the polarization evolution of forty γ-ray bright blazars, including AO 0235+164, on a bi-weekly cadence, as well as other sources in a target-of-opportunity mode. The observations reported here were conducted between July 2022 and December 2023.

The SMA observations use two orthogonally polarized receivers, tuned to the same frequency range in full polarization mode, and use the SWARM correlator (Primiani et al. (2016)). These receivers are inherently linearly polarized but are converted to circular using the quarter-wave plates of the SMA polarimeter (Primiani et al. (2016)). The lower sideband (LSB) and upper sideband (USB) covered 209-221 and 229– 241GHz, respectively. Each sideband was divided into six chunks, with a bandwidth of 2GHz, and a fixed channel width of 140kHz. The SMA data were calibrated with the MIR software package [3]. Instrumental polarization leakage was calibrated independently for USB and LSB using the MIRIAD task `gpcal` (Shaw et al. (1995)) and removed from the data. The polarized intensity, position angle, and polarization percentage were derived from the Stokes I, Q, and U visibilities.

AO 0235+164 was observed 14 times within the above period on June 1, 4, and 16 with integration times between 2.4 and 15 minutes. The total flux density, linear polarization degree and polarization angle results are given in the table attached. MWC 349 A, Callisto, Uranus, Neptune, and Ceres were used for the total flux calibration according to their visibility, and the calibrator 3C 286, which has a high linear polarization degree and stable polarization angle, was observed regularly as a cross-check of the polarization calibration.

[3] https://lweb.cfa.harvard.edu/ cqi/mircook.html

Chapter 5

IOP4, the Interactive Optical Photo-Polarimetric Python Pipeline

The article has been accepted and published in *The Astronomical Journal* (`https://doi.org/10.3847/1538-3881/ad5a80`). The full reference can be found at [26].

The Astronomical Journal, 168:84 (9pp), 2024 August https://doi.org/10.3847/1538-3881/ad5a80

IOP4, the Interactive Optical Photo-Polarimetric Python Pipeline

Juan Escudero Pedrosa[1], Iván Agudo[1], Daniel Morcuende[1], Jorge Otero-Santos[1], Giacomo Bonnoli[2], Vilppu Piirola[3], César Husillos[1,4], Mabel Bernardos[1], Rubén López-Coto[1], Alfredo Sota[1], Victor Casanova[1], Fran J. Aceituno[1], and Pablo Santos-Sanz[1]
[1] Instituto de Astrofísica de Andalucía, Glorieta de la Astronomía, s/n. Granada, 18008, Spain; jescudero@iaa.es
[2] INAF Osservatorio Astronomico di Brera, Via E. Bianchi 46. Merate (LC), 23807, Italy
[3] Department of Physics and Astronomy, University of Turku, Vesilinnantie 5. Turku, FI-20014, Finland
[4] Geological and Mining Institute of Spain (IGME-CSIC), Calle Ríos Rosas 23, E-28003, Madrid, Spain
Received 2024 April 23; revised 2024 June 11; accepted 2024 June 18; published 2024 July 22

Abstract

IOP4 is a pipeline to perform photometry and polarimetry analysis of optical data from Calar Alto (CAHA) and Sierra Nevada (OSN) observatories. IOP4 implements Object Relational Mapping to seamlessly integrate all information about the reduction and results in a database that can be used to query and plot results, flag data, and inspect the reduction process in an integrated fashion with the whole pipeline. It also ships with an already built-in web interface that can be used out of the box to browse the database and supervise all pipeline processes. It is built to ease debugging and inspection of data. Reduction from five different instruments are already implemented: RoperT90, AndorT90, DIPOL (at OSN 0.9 m telescope), AndorT150 (OSN 1.5 m telescope), and CAFOS (CAHA 2.2 m telescope). IOP4's modular design allows for easy integration of new observatories and instruments, and its results have already featured in several high-impact refereed publications. In this paper we describe the implementation and characteristics of IOP4.

Unified Astronomy Thesaurus concepts: Astronomy data analysis (1858); Photometry (1234); Polarimetry (1278); Astronomy databases (83); Open source software (1866)

1. Introduction

Optical photo-polarimetric observational programs, especially those dedicated to monitoring, can regularly produce large quantities of data that can take considerable time and effort to be managed and reduced. The effort necessary to produce good quality results extends beyond the use of automatic tools and can include a human-supervised iterative process of debugging the reduction and comparing the employed methods and results with those of different programs. The use of automatic tools is therefore necessary; however, in many instances they obscure the process of reduction and intermediate results, making the debugging of any problem in the results a hard task.

IOP4 implements object-relational mapping using Django's ORM system. This allows to transparently keep the database schema up to date with the models used by the pipeline without any need to mess with the underlying SQL queries. The choice of Django's as ORM backend allows to seamlessly use the rest of Django Framework to serve the results, including but not limited to its admin interface to inspect the database, and Django's debug web server. These tools are all written in Python and packaged for pip and conda, a programming language and distributions that many astronomers are already familiarized with, easing its installation and usage. This also makes IOP4 a multi-platform software, compatible both with macOS and Linux.

The main goal of being a multiinstrument pipeline differentiates IOP4 from preexisting software, which is usually instrument-specific. Five different instruments (RoperT90, AndorT90, AndorT150, DIPOL, and CAFOS) from three different telescopes (Sierra Nevada Observatory (OSN) 0.9 m, OSN 1.5 m, and Calar Alto Observatory (CAHA) 2.2m) in two different observatories (Sierra Nevada and Calar Alto) are already implemented (see Section 6). The choice of Python as the main programming language and IOP4's modular design facilitate the integration of new instruments and the implementation of new reduction procedures to the wider astronomical community. IOP4 intends to be not only a pipeline for data reduction, but to provide a fully equipped portal and web interface. This is specially useful for teams where the tasks of performing observations, reducing, inspecting, and debugging data, and publication or sharing of results are divided among several people, as large monitoring and observational programs often require.

IOP4 builds on top of existing technologies, some of them already cited: Django (ORM and web application framework), SQLite (default database backend), astrometry.net (blind astrometric calibration; Lang et al. 2010), Bokeh (high quality and interactive plots in the web interface), Vue.js (single-page web application), Quasar (user interface components), and JS9 (a ds9 web port for interactive FITS visualization). Many other open-source packages are used, the complete list can be found in the `pyproject.toml` file. All of them are automatically installed together with IOP4.

Hardware requirements of IOP4 are low, even compared today to modern day consumer-end laptops. The blind astrometric calibration using the astrometry.net solver and its index files can take as much as 35 GB with the default configuration, although this requirement can be lowered. SSD storage is also recommended, although not necessary, since IOP4 needs to read significant amounts of data and will benefit from the increased speed, especially during the astrometric calibration. Although it is able to run on a single-core,

The Astronomical Journal, 168:84 (9pp), 2024 August

significant speed improvements can be gained from using up to 20 cores, the recommended maximum with the default configuration and database (DB) backend. Higher levels of concurrency are possible by tuning the DB configuration or specifying a different backend. A good internet connection can speed up the first execution of IOP4, including tests, since it will need to download astrometry index files.

IOP4 facilitates both automatic reduction and manual inspection of the procedure. The `iop4` command provides several options to select different epochs and files and automatically process them. The IOP4LIB allows any user to write its own custom reduction scripts, and provides the tools to invoke any part of the reduction procedure, and inspect and manipulate any object in the database from an interactive terminal, a Python script or a Jupyter Notebook. The IOP4API implements several Application Public Interface (API) end points and web applications that allow end users to easily query results, produce plots, flag bad data, and inspect any object. The portal can be used standalone as in the ready for use IOP4SITE project, or integrated into other sites to be served to the general public.

2. General Reduction Procedure

The automatic reduction procedure generally starts with a simple invocation of the `iop4` command. The main script can be requested to select epochs in the local archive or to discover and download epochs in the remote telescope repositories. For each epoch, the script goes through the usual steps of photo-polarimetric reduction:

1. Classification of raw science images: this includes their type (bias, darks, flats, and science images), discovering the instrument and type of observation (photometry or polarimetry), and translation of standard and nonstandard keywords (exposure time, band, datetime, rotator angles, and objects).
2. Creation of master calibration frames: images of each type (bias, darks, and flats) are grouped and merged together to create the master calibration frames available for each night.
3. Reduction and calibration of science images: raw images are applied the corresponding master calibration frames. The reduced images are also given a correct World Coordinate System (WCS) in their header after astrometric calibration.
4. Computation of photo-polarimetric results: at the moment, the procedure implements relative photometry using known calibrators in the field, and polarimetry both for half-wave ($\lambda/2$) retarder based polarizers and polarized filter wheels.
5. Post-processing of results: this includes correction of magnitude and degree of polarization to account for the host contribution (Nilsson et al. 2007), and the possibly needed transformation to a standard photometric system, if the instrument used for the observations does not have one.

The same methods that the main script uses for bulk processing of epochs, can be invoked from the command line or custom scripts using the IOP4LIB directly. The IOP4LIB can used to query objects in the DB, debug the reduction process, or create custom procedures, as the examples in the documentation show.

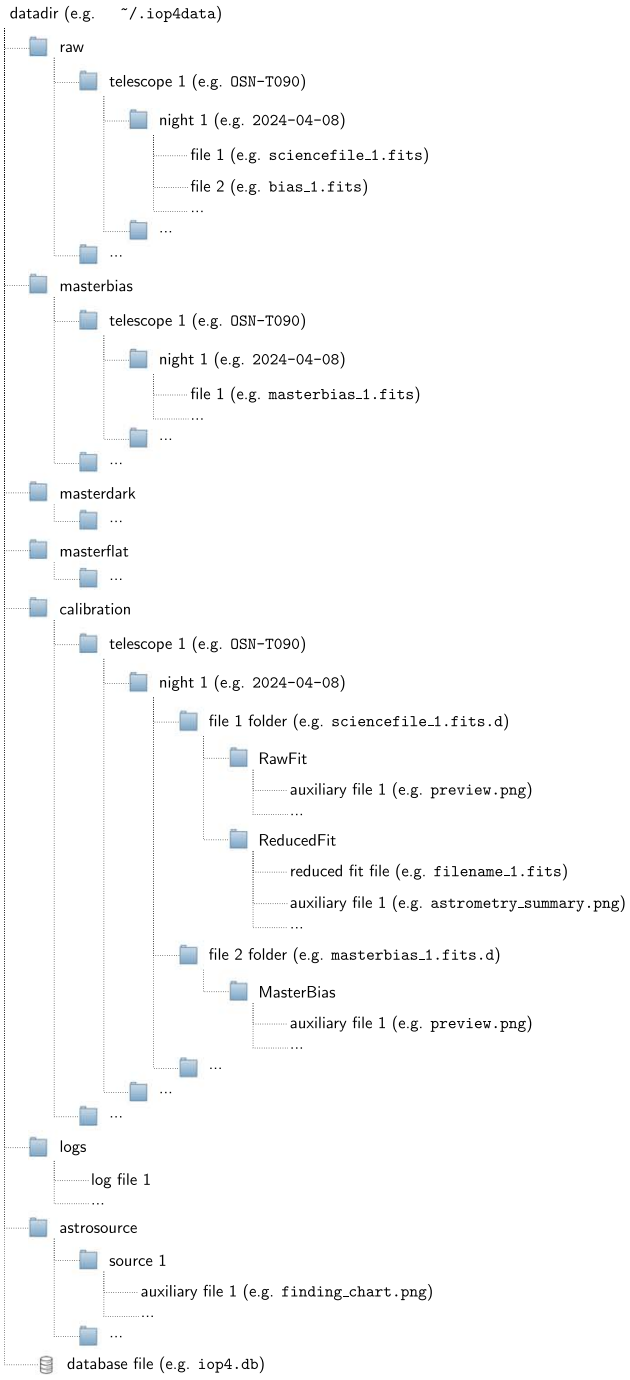

Figure 1. Directory structure of the IOP4 local archive.

3. Data Organization

IOP4 data directory structure follows the typical hierarchical schema shown in Figure 1. In this schema, all raw data is stored and isolated under a single folder (`raw/`), which allows to set up a local archive of the original data without any modifications for long-term conservation, and to set up the necessary permissions to protect and share it with other system users (e.g., creating a link) independently of the rest of IOP4-created files. Under the raw directory, data is organized first by telescope and then by night of observation. Other files such as built master calibration frames and

The Astronomical Journal, 168:84 (9pp), 2024 August

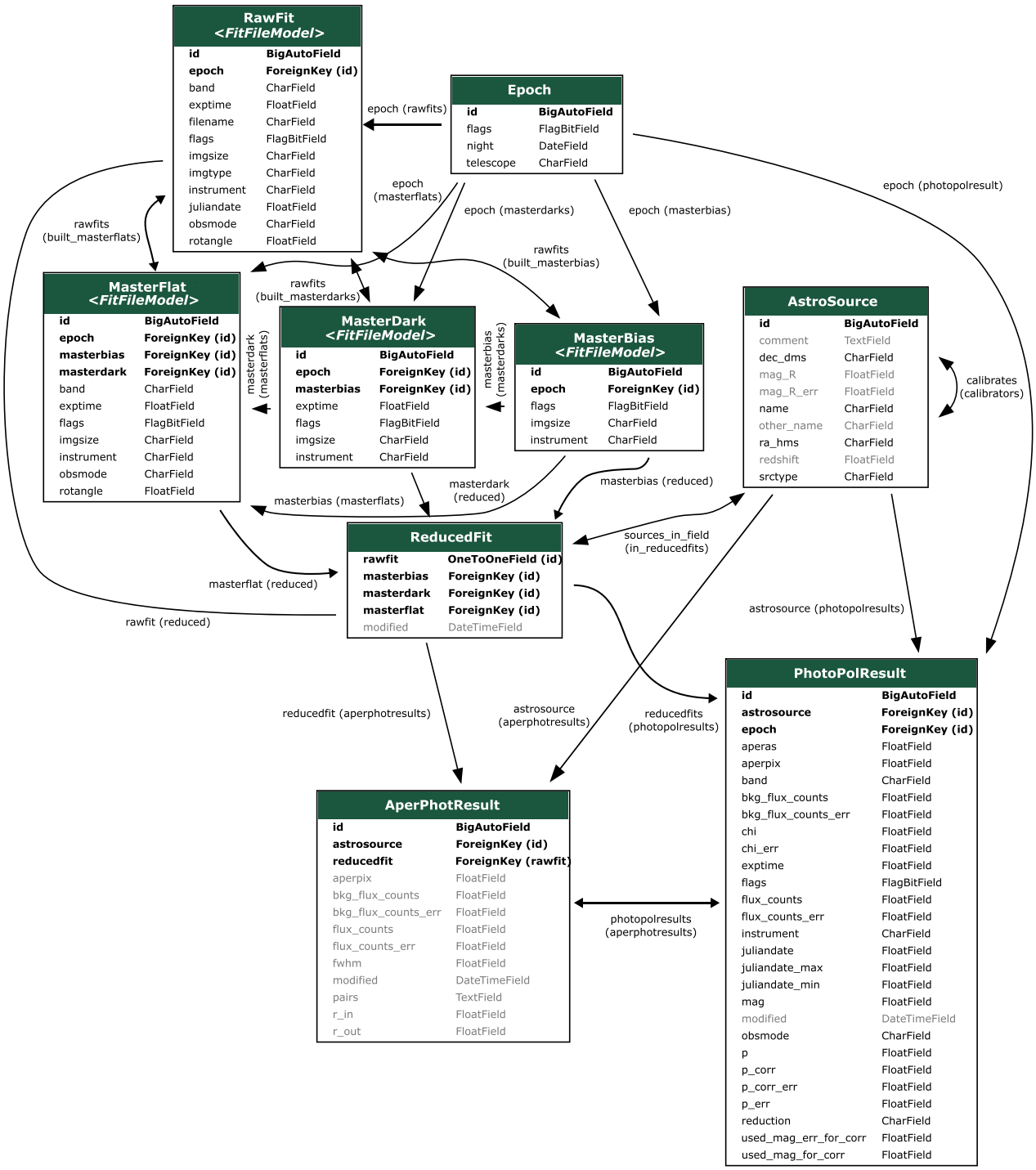

Figure 2. Database schema of IOP4. *ForeignKey* relationships relate one or several instances of model A to a single instance of model B. In *ManyToMany* relationships, multiple instances of model A and B are linked together. The latter does not show a field in the tables of this diagram, since the relationship is established through a hidden table omitted here. Some fields of the `AstroSource` model have been also omitted to save space (corresponding to literature magnitudes in other bands, e.g., `mag_B`, etc). An arrow in any direction signify multiple instances being linked to the origin (e.g., several RawFit(s) are linked to one Epoch).

reduced images are stored separately. Also, auxiliary images, such as automatically built previews, finding charts, summary plots, etc, which are too heavy to be stored in a database, are stored under different folders.

The database schema is shown in Figure 2. IOP4 implements object-relational mapping (ORM). In ORM, objects in a object-oriented programming language (Python classes) are mapped to tables in a relational database, while instances of these objects correspond to rows in each of the tables. This enormously simplifies the interaction with the database, removing the need for writing SQL queries and manipulating the database to keep its structure and content updated.

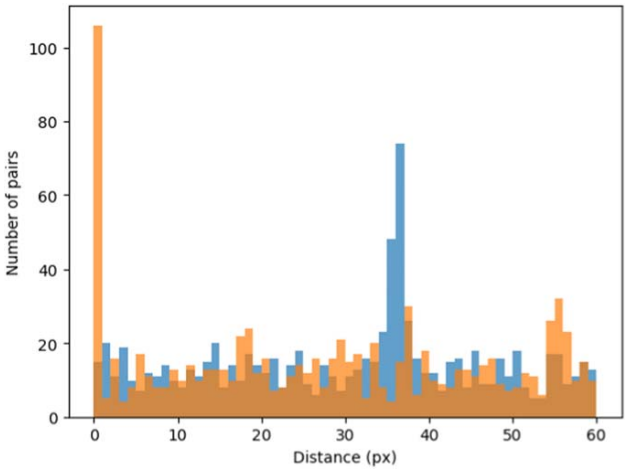

Figure 3. Distribution of the distances between all possible pairs in a imaging polarimetric frame. The two peaks correspond to the distance between the ordinary and extraordinary sources in the image. The image and the corresponding found pairs can be found in Figure 4. The orange and blue distributions correspond to the distances in the *X*- and *Y*-axis, respectively. The image corresponds to a CAFOS photo-polarimetric observation of the BL Lacertae field.

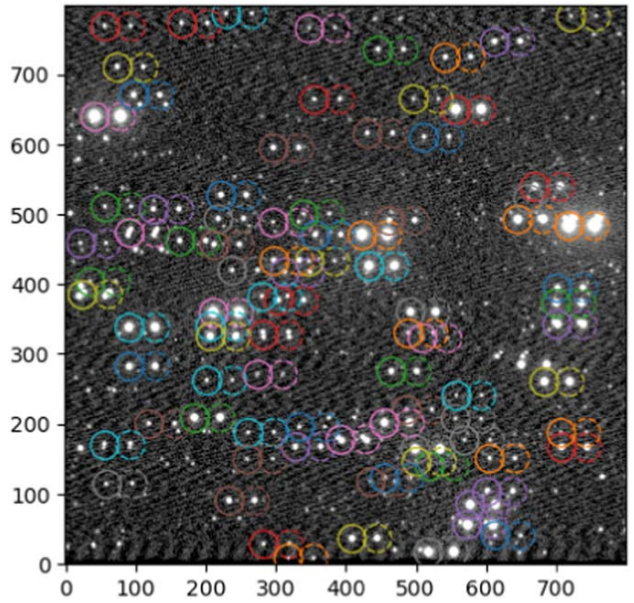

Figure 4. Paired sources in an example of CAFOS imaging polarimetric observation of the BL Lacertae field. The distance used for pairing was obtained from Figure 3. The resulting calibrated image can be found in Figure 5. Ordinary and Extraordinary sources are circled with the same color.

The default database backend is SQLite,[5] an in-process library that implements a self-contained, serverless, zero-configuration, and transactional SQL database; and uses the Django ORM[6] to interact with it. Customizations and changes to the DB schema can be written in the code (e.g., adding an attribute to the photo-polarimetric result model) and they will be automatically propagated to the DB schema by the Django migration system. IOP4 fine tunes SQLite configuration to improve its behavior and speed for high (write) concurrency, as it is needed for parallelization. This setup has been tested using up to 20 cores, although it is probable that a significantly higher number of cores is usable in the default configuration. For even higher workloads, such as those in cluster environments, a different DB backend can be specified (e.g., PostgreSQL).

4. Astrometric Calibration

Astronomical images are usually distributed in the FITS format (Pence et al. 2010). The format allows for a WCS (Greisen & Calabretta 2002) to be incorporated in the metadata or header section of the FITS file. However, most raw science images from telescopes do not include this precise information and need to be calibrated. For most images, which have a wide field of view ($>7'$) this is done by a local solver[7] based on the astrometry.net library solver.[8]

For observations with Ordinary (O) and Extraordinary (E) images (e.g., CAFOS and DIPOL imaging polarimetric observations), astrometric calibration involves a previous step of separating the detected sources in pairs. The source pairing is done by finding the most common distance between all pairs of sources in the image, which results in two distributions like those in Figure 3. Then, the separation can proceed by looking at which pairs are at the right shift (Figure 4). Without any constraint, this process is not completely error free, specially for images with few detected sources. However, since the distance between pairs is usually a stable property of the instrument, the known distance between pairs (obtained by the unconstrained pairing) for an instrument can be used as initial input, which improves the success rate up to 100%.

The detected sources in the image, or the ordinary set of pairs for images with pairs, can then be used as input for the local astrometry solver (Lang et al. 2010). The solver compares invariant hashes computed from the detected source positions to precomputed hashes from astronomical catalogs. Although it does not require an initial guess of the position nor the pixel size (blind solving), the speed and accuracy of the solution is greatly improved by providing the known pixel size for the instrument and a hint position, obtained from the header of the images. It returns a list of matches and their corresponding log-odds. Its success is dependent on the source detection step, and therefore several attempts are made with different detection parameters (such as signal threshold) until a good match is found. The resulting WCS is written to the header of the reduced FITS file. The WCS for the second or extraordinary set of pairs is directly built from the first one by translation, and written next to it in the same header. An example of the result can be found in Figure 5, which corresponds to the pairs in Figures 3 and 4.

4.1. A Quad Hash for DIPOL Polarimetry Images

To reduce the disk capacity requirements of DIPOL polarimetry images, only a subframe of the full field of DIPOL camera is saved (Section 6.3). The reduced field of view does not usually contain enough stars to perform the astrometric calibration using the default solver. In fact, in many cases, only the O and E images of the target source are visible in the image.

[5] https://www.sqlite.org/

[6] https://docs.djangoproject.com/

[7] The local solver is integrated as an external Python module dependency in the `pyproject.toml` file and is installed next to IOP4 automatically. The module is a wrapper around the native C functions of the astrometry.net library: https://github.com/neuromorphicsystems/astrometry.

[8] https://github.com/dstndstn/astrometry.net

The Astronomical Journal, 168:84 (9pp), 2024 August

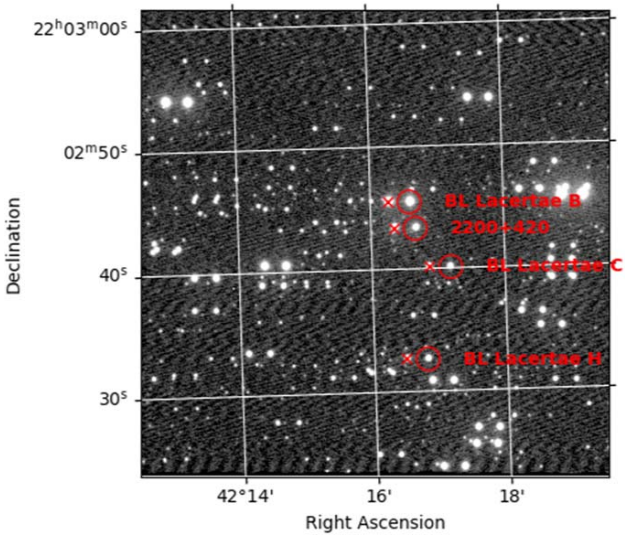

Figure 5. Calibrated CAFOS photo-polarimetric image of the BL Lacertae field. The positions of the ordinary image of BL Lacertae (labeled as 2200 +420) and its calibrators (B, C, H) are indicated with a circle. The position of the extraordinary images are represented with an "x."

For the case of images in which only one or two pairs of sources appear, the astrometric calibration can be as simple as using the central pair as a reference for the creation of the WCS with the known angle of the RA-DEC grid. However, this process is error-prone when more than two pairs of sources appear in the image, as the likelihood of choosing the wrong pair increases. Even for the case of high number of pairs, the size of the subframe ($2\farcm5 \times 2\farcm0$) is too small even for the smallest skymarks of the default astrometry.net index files.[9] The problem of choosing the right pair of sources as the reference can be solved by comparing the subframe of the polarimetry observation with the central part of a calibrated photometry (full frame) field. To this end, we have implemented a hash algorithm loosely based on Lang et al. (2010). The proposed hash is invariant under rotation and reflection, although not under scaling. An example of this algorithm at work can be found in Figure 6. It takes the ten brightest sources in each image (including E and O images) and compares all the quads between them. The best matching quads are used for identifying the target star.

5. High-level Web Interface

As one of its main goals, IOP4 also provides an API to interact with the data and a web interface to act as a client. Both are provided by the IOP4API Django application. It defines API end points to query results, produce interactive web-based plots, and flag data. It also integrates the IOP4ADMIN site, a customized Django-admin. The admin site allows us to inspect any models in the database (Figure 2).

The IOP4 catalog is part of the database. IOP4 uses a single, unified catalog that gathers all information about the sources of interest, including the target sources, calibrators, relationships between them, comments for observers, etc. Editing of the catalog can be done through IOP4 as with any other model, or through the web interface, and the changes take immediate effect on the reduction process of the pipeline.

[9] http://astrometry.net/doc/readme.html

The situation is illustrated in Figure 7. The exposed API end points are used by the single-page application (SPA) to authenticate the client, query, plot and flag data, and explore logs and catalog. The SPA provides a viewer for the colored logs and allows filtering by logging level (debug, info, warning, and error) and string searching. The interactive plot is built and serialized in the server using the Bokeh (Bokeh Development Team 2023) Python library, sent to the client and rendered by the BokehJS library. The interactive plot can be used to directly flag the data. TabulatorJS[10] is used to display the results, and allows filtering, selecting columns and exporting to several data formats such as CSV. The SPA itself is built in html, css and javascript using Vue.js framework as a standalone script to avoid the build step and allow IOP4 to be installed and used by the astrophysics community in a familiar way (through pip or conda).

The web application provides an auxiliary tool to facilitate the addition to the catalog of calibrators for sources with no known previously documented calibrators. A search for standard stars with constant brightness is performed within the PanSTARRS[11] catalog. For this, we filter stars within the FoV of all instruments that have a relatively large amount of observations available (typically $N \geqslant 10$), with a standard deviation of their aperture SDSS gri magnitudes <0.01. In order to use as calibrators stars that do not have the risk of saturating the images, we also restrict the search to targets with magnitudes between 13 and 18, typically. With these considerations, we retrieve the gri aperture magnitudes of nonvariable stars that will be used as calibrators. Due to the different photometric system filter used by the PanSTARRS database (based on *grizy* filters) and that from the instruments implemented in IOP4 (generally equipped with standard Johnson–Cousins filters) a conversion between photometric systems is needed. Three transformations are currently implemented in IOP4: Jester et al. (2005), Jordi et al. (2006), and Lupton (2005). As explained by these authors, these transformations are suitable for stars, with the caveat of Jester et al. (2005) being only suitable for stars with $R_C - I_C < 1.15$. All three transformations have been found to be compatible for the calibrators added following this procedure. IOP4 implements by default the transformations from Lupton (2005).

6. Current Instruments

Five instruments from three different telescopes are already implemented in IOP4: RoperT90, AndorT90 and DIPOL (at OSN 0.9 m telescope), AndorT150 (OSN 1.5 m telescope), and CAFOS (CAHA 2.2 m telescope). The modular design of IOP4 allows easily integrating new instruments and observatories. The `Telescope` base class provides the skeleton over which to implement new telescopes. It implements the necessary methods to query, download (e.g., through the `FTPArchiveMixin` class), and perform the initial classification of observing epochs.

Integrating a new instrument is as easy as subclassing the `Instrument` subclass. The new subclass must provide the necessary information to identify the instrument, and possibly implement methods to translate nonstandard keywords (if any), extract position and size hints for astrometry, and override existing reduction procedures or implement new ones.

[10] https://tabulator.info/
[11] https://catalogs.mast.stsci.edu/panstarrs/

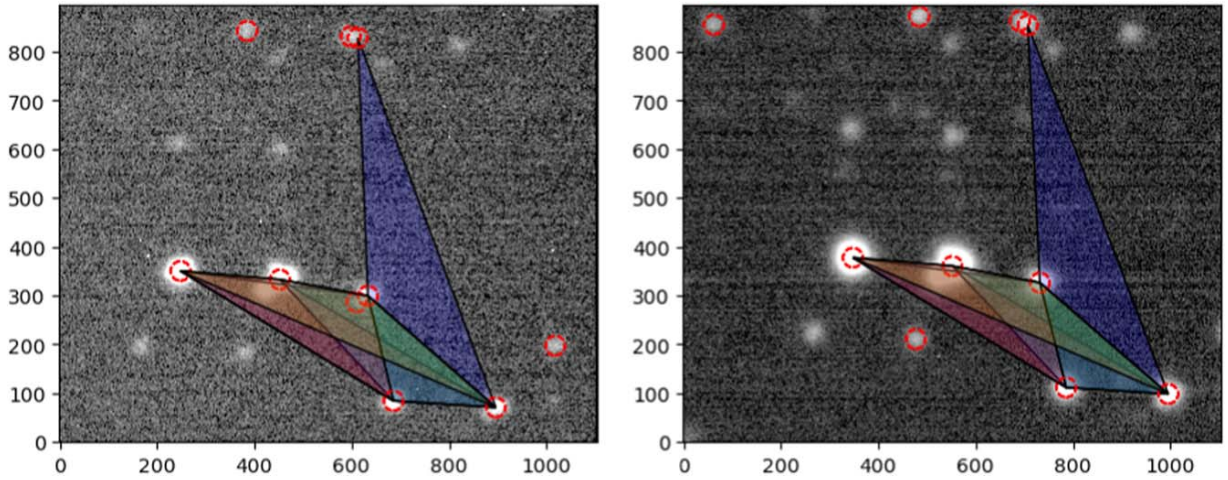

Figure 6. DIPOL polarimetry (left) and photometry (right) frames of BL Lacertae observations. Only the shown subframe ($2\farcm5 \times 2\farcm0$) is usually saved to disk during polarimetric observations with DIPOL, which prevents blind solving of the image. The full photometry field ($9\farcm2 \times 6\farcm3$) is saved, however, and the correspondence between both images can be found by comparing quads of sources through a hashing algorithm. This allows us to automatically distinguish the O and E images of our target source in the field.

6.1. RoperT90, AndorT90, AndorT150

IOP4 implements data reduction from the current CCD (Andor ikon-L) cameras at the 0.9 and 1.5 m telescopes in OSN. It also implements the old Roper (VersArray) cameras (which were installed until 2021 October and 2018 July, respectively). The AndorT90 instrument mounted at the Nasmyth east focus of the T090 telescope has a $13.2' \times 13.2'$ field of view and pixel size of $0\farcs387$ px^{-1}. The AndorT150 instrument at the Nasmyth west focus of the T150 has similar characteristics, with a $7\farcm92 \times 7\farcm92$ field of view and pixel size of $0\farcs232$ px^{-1}. They are cooled down down to -80 °C without need of liquid nitrogen, and can be further cooled down to -100 °C using liquid refrigerant. The low temperatures make the use of dark current calibration frames unnecessary. Apart from the usual band filter wheels, a polarized filter wheel is available at the T090 and the T150 that allows polarimetry measurements by taking series of four images at varying polarized angles in 45 deg steps. From these, the total flux and raw Stokes parameters are computed as

$$F = \langle f \rangle = \frac{1}{4}\sum_i f_i \tag{1}$$

and

$$q_{\rm raw} = \frac{f_0 - f_{90}}{f_0 + f_{90}} \tag{2}$$

$$u_{\rm raw} = \frac{f_{45} - f_{-45}}{f_{45} + f_{-45}}, \tag{3}$$

where f_i are the fluxes at each rotator angle. The instrumental polarization is corrected by applying an offset

$$q_c = q_{\rm raw} - q_{\rm inst} \tag{4}$$

$$u_c = u_{\rm raw} - u_{\rm inst} \tag{5}$$

and a rotation

$$q = q_c \cos(2\chi_{\rm inst}) - u_c \sin(2\chi_{\rm inst}) \tag{6}$$

$$u = u_c \sin(2\chi_{\rm inst}) + u_c \cos(2\chi_{\rm inst}), \tag{7}$$

from which the linear polarization degree and polarization angle are computed as

$$p = \sqrt{q^2 + u^2} \tag{8}$$

$$\chi = \frac{1}{2}\arctan(u, q). \tag{9}$$

6.2. CAFOS

The Calar Alto Faint Object Spectrograph (CAFOS) instrument, mounted on the 2.2 m telescope at Calar Alto Observatory, provides imaging polarimetry capabilities. It is equipped with a Wollaston prism and a rotable $\lambda/2$ retarder plate that provides two polarized images separated $18''$. Only a 800×800 subframe of the full 2048×2048 CCD chip is typically used, with a field of view of $34' \times 34'$ and a pixel size of $0\farcs530$ px^{-1}. The CCD chip is cooled to temperatures lower than -100 °C, making the dark current negligible. Several filters are available, while polarimetry observations are usually taken in Johnson R. The ordinary (O) and extraordinary (E) images at each angle are used to compute the total flux and the reduced Stokes parameters as (Zapatero Osorio et al. 2005)

$$F = \frac{1}{N}\sum_i \frac{f_{E,i} + f_{O,i}}{2} \tag{10}$$

and

$$R_Q = \sqrt{\frac{f_{O,0}/f_{E,0}}{f_{O,45}/f_{E,45}}} \tag{11}$$

$$R_U = \sqrt{\frac{f_{O,22}/f_{E,22}}{f_{O,67}/f_{E,67}}}, \tag{12}$$

where $f_{O,i}$ and $f_{E,i}$ are the fluxes of the ordinary and extraordinary images of the source at each angle i. From these, the Stokes parameters are reconstructed as

$$Q_I = \frac{R_Q - 1}{R_Q + 1} \tag{13}$$

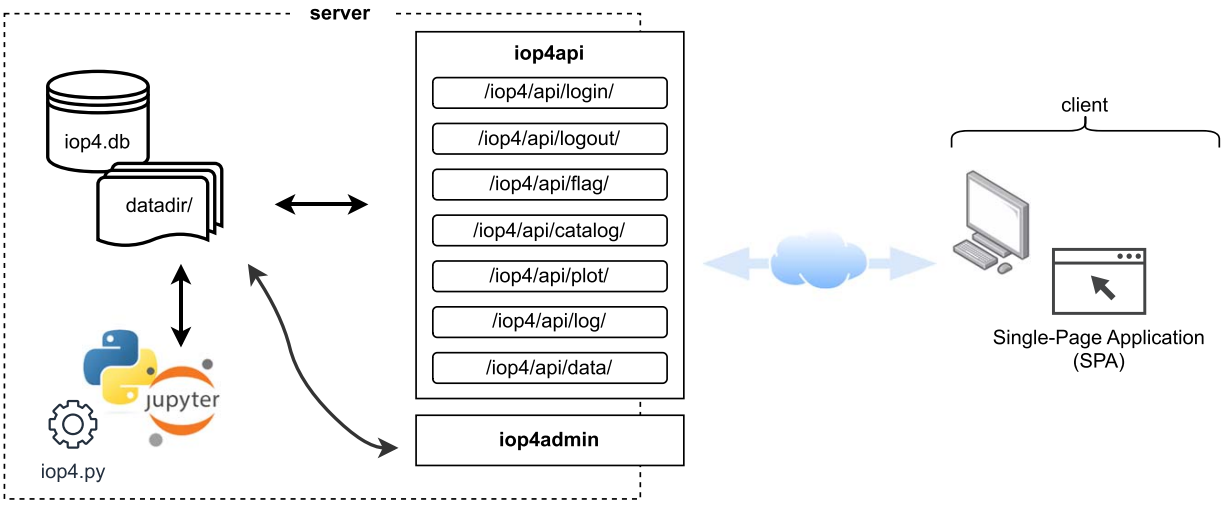

Figure 7. Different ways of interacting with IOP4. The pipeline (through the IOP4 command, Python script or Jupyter notebooks) can directly interact with the data aided by IOP4LIB. The IOP4API application exposes a series of API end points that allow the client to authenticate itself, query, plot and flag data, and explore catalog and logs from a web browser through a single-page application (SPA). The IOP4ADMIN site independently provides a way to interact and edit all models in the database.

$$U_I = \frac{R_U - 1}{R_U + 1}, \tag{14}$$

and the polarization degree and polarization angles from Equations (8) and (9). While instrumental polarization is negligible for CAFOS, the polarization angle still needs to be corrected according to

$$\chi = \chi - \mathrm{CPA}, \tag{15}$$

where CPA is the zero polarization angle.

6.3. DIPOL

The DIPOL-1 polarimeter is thoroughly described in Piirola et al. (2020) and Otero-Santos et al. (2024). It is based on a $\lambda/2$ retarder plate attached to a rotator and a high readout speed CMOS camera. Installed at the OSN-T090 the instrument has a field of view of $9\farcm2 \times 6\farcm3$ and a pixel scale of $0.134''$ px^{-1}. Cycles of 16 images are typically taken with varying rotator angles at $22\fdg5$ steps. For polarimetry observations, usually only a subframe of size $2\farcm5 \times 2\farcm0$ is saved, greatly reducing used disk space. Dark current calibration frames are necessary. High throughput sharp cutoff R, G, and B filters are available. The computation of the polarimetric results is done following Patat & Romaniello (2006). The Stokes parameters are computed as

$$Q_{\mathrm{raw}} = \frac{2}{N}\sum_i F_i \cos\left(\frac{\pi}{2}i\right) \tag{16}$$

$$U_{\mathrm{raw}} = \frac{2}{N}\sum_i F_i \sin\left(\frac{\pi}{2}i\right), \tag{17}$$

where the coefficients F_i are computed as

$$F_i = (F_{O,i} - F_{E,i})/(F_{O,i} + F_{E,i}), \tag{18}$$

$F_{O,i}$ and $F_{E,i}$ being the fluxes of the ordinary and extraordinary images of the source for each rotator angle i. The instrumental polarization is corrected with an offset

$$Q = Q_{\mathrm{raw}} - Q_{\mathrm{inst}} \tag{19}$$

$$U = U_{\mathrm{raw}} - U_{\mathrm{inst}}. \tag{20}$$

Then, p and χ are obtained per Equations (8), (9) and (15). Photometric (full frame) observations are also performed. The conversion of the magnitudes in the Baader RGB filters to standard Johnson–Cousins $UBVR_cI_c$ will be treated in a separate paper (in preparation).

7. Development and CI

IOP4 is open-source, its code hosted at https://github.com/juanep97/iop4. The repository contains all the necessary code to run IOP4 both as a program (`iop4` script) and as a library (IOP4LIB), plus the IOP4API Django application and the customized IOP4ADMIN site. Both can be readily used through the Django debug server and the provided IOP4SITE, or they can be integrated into another site and deployed for public use (see Serving IOP4 in production in IOP4 documentation). To ease the development process and the maintainability of the code, we implemented Continuous Integration and Continuous Deployment (CI/CD) workflows to perform automatic testing, build the documentation and facilitate the delivery of IOP4. The source code includes a test suit, the test data set is freely available at https://vhega.iaa.es/iop4/. The test procedure includes checking the reliability of the reduction and calibration procedures from raw data, and ensuring the quality of the photo-polarimetric results by comparison against tabulated values. The size of the astrometry.net solver index files makes inviable using GitHub-hosted ordinary runners for CI. Instead, a self-hosted runner provided by the VHEGA[12] group with self-provisioning capabilities using GARM[13] automatically runs tests on pull requests and merge commits to the main branch on isolated containers that already provide the test data set and astrometry index files. Anyone can run the test locally in their computers using PYTEST.[14] As of version `v1.2.0` (Escudero Pedrosa et al. 2024), test coverage for IOP4LIB is over 65%.

[12] https://vhega.iaa.es/
[13] https://github.com/cloudbase/garm
[14] https://docs.pytest.org/

The documentation can be built using SPHINX,[15] and contains several notebook examples. MYST-NB[16] and JUPYTEXT[17] allow using the percent format for the notebooks, an human-readable format easily integrable with version control software. The example notebooks are automatically run when building the documentation and use the test data set. The documentation is also automatically built and deployed to GitHub Pages as part of the CI. New releases of IOP4 are automatically deployed to the public PyPi software repository.[18]

8. Conclusions

IOP4 is an open-source, interactive photo-polarimetric pipeline written in Python. Its results have already featured in a number of refereed and high impact publications (e.g., Middei et al. 2023a, 2023b; Di Gesu et al. 2023; Ehlert et al. 2023; Marshall et al. 2023; Peirson et al. 2023; Kim et al. 2024; Otero-Santos et al. 2024; among others), following the footsteps of its predecessor IOP3[19] (e.g., Di Gesu et al. 2022; Liodakis et al. 2022, etc), and has provided data to many ongoing studies. Most of this data comes from the MAPCAT (Agudo et al. 2012) and TOP-MAPCAT programs, having reduced more than 600 GB of data from the these programs as of 2024 June. The former was running at Calar Alto from 2007 to 2018, the latter has been running from 2018 to the present day both at OSN and CAHA. Both programs are focused on the photo-polarimetric monitoring of blazars, combining regular observations with targets of opportunity. Aided by its parallel processing capabilities, it routinely downloads, reduces and serves results from a full night of observation of these programs in less than half an hour. Its speed makes it suitable to be used as a real-time analysis tool. Moreover, IOP4 has contributed to the publication of several Astronomer Telegrams (such as Otero-Santos et al. 2023a, 2023b) thanks to the promptness of its results and the ease of use.

Development of IOP4 is ongoing. Future releases of IOP4 might include several other instruments and reduction methods. As of version `v1.2.0`, IOP4 provides a prefabricated night summary script that sends the results of observations to subscribed users. Future versions might include a more advanced alert and trigger system. In any case, the IOP4LIB already allows the users to create their own scripts, for alerts or any other purpose.

The project welcomes any interested user to participate in IOP4 development and request or contribute to the implementation of new instruments and features.

Acknowledgments

The IAA-CSIC team acknowledges financial support from the Spanish "Ministerio de Ciencia e Innovación" (MCIN/AEI/ 10.13039/501100011033) through the Center of Excellence Severo Ochoa award for the Instituto de Astrofísica de Andalucía-CSIC (CEX2021-001131-S), and through grants PID2019-107847RB-C44 and PID2022-139117NB-C44. P.S-S. acknowledges financial support from the Spanish I+D+i project PID2022-139555NB-I00 (TNO-JWST) funded by MCIN/AEI/10.13039/501100011033. Based on observations made at the Sierra Nevada Observatory (OSN), operated by the Instituto de Astrofísica de Andalucía (IAA-CSIC), and at the Centro Astronómico Hispano-Alemán (CAHA), operated jointly by Junta de Andalucía and the IAA-CSIC. Development of this software would not have been possible without the invaluable and selfless contributions of the open-source community.

Facilities: Instituto de Astrofísica de Andalucía (IAA-CSIC), Observatorio de Sierra Nevada (OSN), Observatorio de Calar Alto (CAHA).

Software: Django (Django Software Foundation 2023), SQLite (SQLite Developers 2023), Vue.js (Vue Developers 2023), numpy (Harris et al. 2020), astropy (Astropy Collaboration et al. 2013, 2018, 2022), photutils (Bradley et al. 2023), astrometry.net (Lang et al. 2010).

ORCID iDs

Juan Escudero Pedrosa https://orcid.org/0000-0002-4131-655X
Iván Agudo https://orcid.org/0000-0002-3777-6182
Daniel Morcuende https://orcid.org/0000-0001-9400-0922
Jorge Otero-Santos https://orcid.org/0000-0002-4241-5875
Giacomo Bonnoli https://orcid.org/0000-0003-2464-9077
Vilppu Piirola https://orcid.org/0000-0003-0186-206X
César Husillos https://orcid.org/0000-0001-8286-5443
Rubén López-Coto https://orcid.org/0000-0002-3882-9477
Pablo Santos-Sanz https://orcid.org/0000-0002-1123-983X

References

Agudo, I., Molina, S. N., Gómez, J. L., et al. 2012, IJMPS, 8, 299
Astropy Collaboration, Price-Whelan, A. M., Lim, P. L., et al. 2022, ApJ, 935, 167
Astropy Collaboration, Price-Whelan, A. M., Sipőcz, B. M., et al. 2018, AJ, 156, 123
Astropy Collaboration, Robitaille, T. P., Tollerud, E. J., et al. 2013, A&A, 558, A33
Bokeh Development Team 2023, Bokeh: Python Library for Interactive Visualization, https://bokeh.org/
Bradley, L., Sipőcz, B., Robitaille, T., et al. 2023, astropy/photutils: v1.8.0, Zenodo, doi:10.5281/zenodo.7946442
Di Gesu, L., Donnarumma, I., Tavecchio, F., et al. 2022, ApJL, 938, L7
Di Gesu, L., Marshall, H. L., Ehlert, S. R., et al. 2023, NatAs, 7, 1245
Django Software Foundation 2023, Django, 4.2., https://www.djangoproject.com
Ehlert, S. R., Liodakis, I., Middei, R., et al. 2023, ApJ, 959, 61
Escudero Pedrosa, J., Morcuende Parrilla, D., & Otero-Santos, J. 2024, IOP4, v1.2.0, Zenodo, doi:10.5281/zenodo.11548299
Greisen, E. W., & Calabretta, M. R. 2002, A&A, 395, 1061
Harris, C. R., Millman, K. J., van der Walt, S. J., et al. 2020, Natur, 585, 357
Husillos, C., Bernardos, M., Agudo, I., Bonnoli, G., & Escudero Pedrosa, J. 2021, cesarhusrod/iop3: v1.0.0, Zenodo, doi:10.5281/zenodo.10995575
Jester, S., Schneider, D. P., Richards, G. T., et al. 2005, AJ, 130, 873
Jordi, K., Grebel, E. K., & Ammon, K. 2006, A&A, 460, 339
Kim, D. E., Di Gesu, L., Liodakis, I., et al. 2024, A&A, 681, A12
Lang, D., Hogg, D. W., Mierle, K., Blanton, M., & Roweis, S. 2010, AJ, 139, 1782
Liodakis, I., Marscher, A. P., Agudo, I., et al. 2022, Natur, 611, 677
Lupton, R. 2005, Transformations between SDSS magnitudes and other systems—SDSS-III, https://www.sdss3.org/dr8/algorithms/sdssUBVRITransform.php#Lupton2005
Marshall, H. L., Liodakis, I., Marscher, A. P., et al. 2023, arXiv:2310.11510
Middei, R., Liodakis, I., Perri, M., et al. 2023a, ApJL, 942, L10
Middei, R., Perri, M., Puccetti, S., et al. 2023b, ApJL, 953, L28
Nilsson, K., Pasanen, M., Takalo, L. O., et al. 2007, A&A, 475, 199
Otero-Santos, J., Piirola, V., Escudero, J., et al. 2023a, ATel, 16305, 1
Otero-Santos, J., Piirola, V., Escudero Pedrosa, J., et al. 2024, AJ, 167, 137
Otero-Santos, J., Piirola, V., Pacciani, L., et al. 2023b, ATel, 16360, 1
Patat, F., & Romaniello, M. 2006, PASP, 118, 146

[15] https://www.sphinx-doc.org/
[16] https://myst-nb.readthedocs.io/
[17] https://jupytext.readthedocs.io/
[18] https://pypi.org/project/iop4/
[19] Husillos et al. (2021).

Peirson, A. L., Negro, M., Liodakis, I., et al. 2023, ApJL, 948, L25
Pence, W. D., Chiappetti, L., Page, C. G., Shaw, R. A., & Stobie, E. 2010, A&A, 524, A42
Piirola, V., Berdyugin, A., Frisch, P. C., et al. 2020, A&A, 635, A46
SQLite Developers 2023, SQLitehttps://www.sqlite.org/
Vue Developers 2023, Vue, 3.4.9., https://vuejs.org/
Zapatero Osorio, M. R., Caballero, J. A., & Béjar, V. J. S. 2005, ApJ, 621, 445

Chapter 6

Conclusions

In this thesis we have introduced the blazar phenomenon and presented new work and results that will help shed some light over the the inner mechanisms of these objects. To this end, we chose the blazar AO 0235+164 as our main object of study in Chapters 3 and 4.

In Chapter 3, we presented spectral energy distribution models that show how the high-energy emission of AO 0235+164 can be explained as synchrotron self-Compton radiation. We also showed how only synchrotron self-Compton emission can explain the spectral energy distribution of AO 0235+164 in a consistent way with the results derived from correlations and the kinematic analysis of the jet in VLBI images. We also showed that the standard single zone models are not enough to describe the emission, requiring secondary regions that can explain the spectral shape in the X-ray range; in agreement with the results of the correlation analysis. The secondary emitting region is much smaller in size than the main region, and is situated closer to the central black hole.

In Chapter 4, we demonstrated how the observed changes in the direction of ejection of VLBI components suggest the existence of a period in the observed wobbling of the jet, that is compatible with what is expected from a precessing jet with a period of 6 years. This value is independently obtained, but compatible, with those found in the existing literature, that are usually obtained through statistical and auto-correlation analyses of historical light curves; methods that have been independently reproduced in this work too. Although we do not observe strict periodicity in the flux emission of AO 0235+164, the observed wobbling and its modeled period must indeed have an origin that could justify the repeating flaring activity and the timescale of variability of 6-8 years found in the light curves in previous works ([39, 40]) and in Sect. 4.3. The absence of a strict periodicity in the flux evolution of the

source is to be expected due to the fact that jet emission is a complex process that can be affected by many causes (jet angle, speed, magnetic field, matter accretion, available energy, to name only a few) and is inherently stochastic. Jet precession is expected in many astrophysical scenarios such as a binary system ([41]) or an off-axis accretion disk (Lense-Thirring effect), and this exact periodicity could be distortedly reflected in the light curves. A precessing jet with a periodicity around ~ 6 years could motivate the appearance of the pseudo-periodic timescale found in the light curves by previous works.

As evidenced in this thesis, a comprehensive study of blazars requires a significant observational effort that can support models, theories, and other astrophysical advancements on a solid experimental base. Therefore the work done regarding this thesis comprises not only direct studies of blazar, but the observations conducted and the subsequent reduction of data. During the work of this thesis, almost half a year of on-site observations with the MAGIC and LST-1 telescopes, and several weeks of on-site and remote observations at the IRAM 30m telescope and the Sierra Nevada and Calar Alto observatories, were carried out. The observations at the IRAM 30m telescope were performed as part of the POLAMI program ([19, 20, 21]); observations in CAHA and OSN were performed as part of the MAPCAT and TOP-MAPCAT programs ([24]). Data from these programs have been featured in many high-impact publications, and in particular in the articles presented in this thesis ([37], Chapter 3; [38], Chapter 4; [26], Chapter 5).

During August 2021 on-site observations with the LST-1 telescope in La Palma, the LST observed for the first time very-high-energy γ-ray variability in the timescale of minutes from BL Lacerteae. The discovery was performed during the brightest ever recorded flare of the source. The data and first analyses have been presented in several conferences (e.g. [28]), and are part of several articles in preparation. The detected VHE γ-ray variability constrain the possible emitting region sizes, hinting at the necessity of a multi-zone model that can reconcile these observations with the constraints from optical and VLBI data ([22]), and serves as a starting point for SED models of MWL emission. Such a model is presented in Figure 2.9 and will be part of future publications. These results exemplify how the analysis that was performed using AO 0235+164 is transferable to other blazar objects; and in fact suggests that SSC might dominate emission in objects of this class (BLLac-type blazars), and that secondary emitting regions might be necessary to explain their X-ray spectrum and VHE γ-ray variability during their high state.

For all these reasons, in Chapter 5, we introduced the IOP4 pipeline, which was developed to address the needs of large scale optical photo-polarimetric monitoring programs of blazars. Programs of this type are needed to build historical datasets,

provide good sampling rates of light curves (e.g. for correlations analyses, which are extremely sensible to it), build catalogs and datasets for population studies, provide alerts to the community (e.g. Astronomer Telegrams, [42, 43]), etc. These programs can regularly produce large quantities of data that can take considerable time and effort to be managed and reduced. The effort necessary to produce good quality results extends beyond the use of automatic tools and can include a human-supervised iterative process of debugging data and procedures. Furthermore, large observational programs are usually a team effort where the tasks of making observations, reducing the data, inspecting the results and sharing the data are divided among several people. IOP4 intends to be not only a pipeline for data reduction, but to provide a fully-equipped portal and web interface. It was written in Python, at the moment one of the most widely used languages in the astronomical community. It implements object relational mapping, which allows to abstract any interaction with the database. The modular design of IOP4 makes it easy to integrate new instruments and data reduction procedures. IOP4 was used to reduce more than 600 GB of data, produced in the last decades by the MAPCAT (2007 to 2018) and TOP-MAPCAT (2018 to present) programs.

In the near future, recent advancements in high-energy polarimetry might provide a decisive answer to some the open question about blazars, such as the origin of the seed photon field in leptonic scenarios ([44]), or questions about the hadronic content of the jet. The launch of the *Imaging X-ray Polarimetry Explorer* (*IXPE*) at the end of the year 2021, has enabled the possibility of measuring the polarization of X-rays, with recent works already establishing constraints in the nature of particle acceleration ([45]). The planned launch of the *Compton Spectrometer and Imager* (*COSI*) in 2027 will, for the first time, open the possibility of studying the polarization of -soft- γ-rays. The improved sensitivity of the future CTAO γ-ray observatory, which will outperform by an order of magnitude current instruments, will allow to further constrain emission models up to hundreds of TeV ([27]). As we extend our vision to increasingly higher energies, we position ourselves to answer some of the long-standing questions about our Universe.

Agradecimientos

Finalizar una tesis doctoral es la culminación de una carrera que comienza, en algunos casos, desde muy joven. Me he cruzado a muchas personas en este largo camino que me han ayudado y me han transmitido ánimos para seguir, conscientes o no de ello. Algunas todavía me acompañan, otras siguieron caminos distintos. A todas les doy las gracias.

En especial, quiero darle las gracias a mi familia, por todo el apoyo, que ha ido más allá de la responsabilidad y ha sido incondicional. A mi madre por ser una fuente de amor infinito, a mi padre, a mi hermano. Todo lo que tiene valor para mi lo tiene porque estáis vosotros.

Por las veces que ha hecho de amigo, de maestro y de hermano, gracias a Florín. Daremos ese paseo por la Carrera de la Virgen. Gracias a Hamzita, por ser como es.

Gracias a Iván, por ser un director y un amigo, y por haberme dado la oportunidad. A Rubén, también por su amistad, y por las veces que ha hecho de director, por su guía. A ambos por el ejemplo. A Pique, que aunque haya huido al E, no se ha llevado los recuerdos de las conversaciones por Pádova, de la infame subida al Mulhacén, ni muchos otros. A Giacomo, por ser el italiano más andaluz. A Dani y a Jorge, a Till, y a todos los que me han echado una mano cuando me ha hecho falta. A los trabajadores del Observatorio de Sierra Nevada, por su hospitalidad y su dedicación. Y al Instituto de Astrofísica de Andalucía y a sus gentes... sé que aquí hay algo distinto; espero poder encontrarlo donde vaya, pero sobre todo espero encontrarlo al volver.

Bibliography

[1] H. D. Curtis. "Descriptions of 762 Nebulae and Clusters Photographed with the Crossley Reflector". In: *Publications of Lick Observatory* 13 (Jan. 1918), pp. 9–42.

[2] Bradley W. Carroll and Dale A. Ostlie. *An introduction to modern astrophysics, Second Edition*. 2017.

[3] C. Megan Urry and Paolo Padovani. "Unified Schemes for Radio-Loud Active Galactic Nuclei". In: *PASP* 107 (Sept. 1995), p. 803. DOI: 10.1086/133630. arXiv: astro-ph/9506063 [astro-ph].

[4] A. Einstein. "Zur Elektrodynamik bewegter Körper". In: *Annalen der Physik* 322.10 (Jan. 1905), pp. 891–921. DOI: 10.1002/andp.19053221004.

[5] Charles D. Dermer and Govind Menon. *High Energy Radiation from Black Holes: Gamma Rays, Cosmic Rays, and Neutrinos*. 2009.

[6] A. G. Pacholczyk. *Radio astrophysics. Nonthermal processes in galactic and extragalactic sources*. 1970.

[7] O. Klein and T. Nishina. "Über die Streuung von Strahlung durch freie Elektronen nach der neuen relativistischen Quantendynamik von Dirac". In: *Zeitschrift fur Physik* 52.11-12 (Nov. 1929), pp. 853–868. DOI: 10.1007/BF01366453.

[8] Markus Böttcher, Daniel E. Harris, and Henric Krawczynski. *Relativistic Jets from Active Galactic Nuclei*. John Wiley & Sons, Ltd, 2012. ISBN: 9783527641741. DOI: https://doi.org/10.1002/9783527641741.ch1.

[9] D. J. Bird et al. "Detection of a Cosmic Ray with Measured Energy Well beyond the Expected Spectral Cutoff due to Cosmic Microwave Radiation". In: *ApJ* 441 (Mar. 1995), p. 144. DOI: 10.1086/175344. arXiv: astro-ph/9410067 [astro-ph].

[10] IceCube Collaboration et al. "Multimessenger observations of a flaring blazar coincident with high-energy neutrino IceCube-170922A". In: *Science* 361.6398, eaat1378 (July 2018), eaat1378. DOI: 10.1126/science.aat1378. arXiv: 1807.08816 [astro-ph.HE].

[11] Albert Einstein. "Zur allgemeinen Relativitätstheorie". In: *Sitzungsberichte der Königlich Preussischen Akademie der Wissenschaften* (Jan. 1915), pp. 778–786.

[12] Karl Schwarzschild. "Über das Gravitationsfeld eines Massenpunktes nach der Einsteinschen Theorie". In: *Sitzungsberichte der Königlich Preussischen Akademie der Wissenschaften* (Jan. 1916), pp. 189–196.

[13] Roy P. Kerr. "Gravitational Field of a Spinning Mass as an Example of Algebraically Special Metrics". In: *Phys. Rev. Lett.* 11.5 (Sept. 1963), pp. 237–238. DOI: 10.1103/PhysRevLett.11.237.

[14] E. T. Newman et al. "Metric of a Rotating, Charged Mass". In: *Journal of Mathematical Physics* 6.6 (June 1965), pp. 918–919. DOI: 10.1063/1.1704351.

[15] R. D. Blandford and R. L. Znajek. "Electromagnetic extraction of energy from Kerr black holes." In: *MNRAS* 179 (May 1977), pp. 433–456. DOI: 10.1093/mnras/179.3.433.

[16] The Event Horizon Telescope Collaboration et al. "First M87 Event Horizon Telescope Results. I. The Shadow of the Supermassive Black Hole". In: *The Astrophysical Journal Letters* 875.1 (Apr. 2019), p. L1. DOI: 10.3847/2041-8213/ab0ec7. URL: https://dx.doi.org/10.3847/2041-8213/ab0ec7.

[17] Ivana Batković et al. "Axion-Like Particle Searches with IACTs". In: *Universe* 7.6, 185 (June 2021), p. 185. DOI: 10.3390/universe7060185. arXiv: 2106.03424 [astro-ph.HE].

[18] G. Amelino-Camelia et al. "Tests of quantum gravity from observations of γ-ray bursts". In: *Nature* 393.6687 (June 1998), pp. 763–765. DOI: 10.1038/31647. arXiv: astro-ph/9712103 [astro-ph].

[19] Iván Agudo et al. "POLAMI: Polarimetric Monitoring of AGN at Millimetre Wavelengths – I. The programme, calibration and calibrator data products". In: *Monthly Notices of the Royal Astronomical Society* 474.2 (Sept. 2017), pp. 1427–1435. ISSN: 0035-8711. DOI: 10.1093/mnras/stx2435. eprint: https://academic.oup.com/mnras/article-pdf/474/2/1427/24011516/stx2435.pdf. URL: https://doi.org/10.1093/mnras/stx2435.

[20] Clemens Thum et al. "POLAMI: Polarimetric Monitoring of Active Galactic Nuclei at Millimetre Wavelengths – II. Widespread circular polarization". In: *Monthly Notices of the Royal Astronomical Society* 473.2 (Sept. 2017), pp. 2506–2520. ISSN: 0035-8711. DOI: 10.1093/mnras/stx2436. eprint: https://academic.oup.com/mnras/article-pdf/473/2/2506/24039409/stx2436.pdf. URL: https://doi.org/10.1093/mnras/stx2436.

[21] Iván Agudo et al. "POLAMI: Polarimetric Monitoring of Active Galactic Nuclei at Millimetre Wavelengths – III. Characterization of total flux density and polarization variability of relativistic jets". In: *Monthly Notices of the Royal Astronomical Society* 473.2 (Sept. 2017), pp. 1850–1867. ISSN: 0035-8711. DOI: 10.1093/mnras/stx2437. eprint: https://academic.oup.com/mnras/article-pdf/473/2/1850/24039421/stx2437.pdf. URL: https://doi.org/10.1093/mnras/stx2437.

[22] Zachary R. Weaver et al. "Kinematics of Parsec-scale Jets of Gamma-Ray Blazars at 43 GHz during 10 yr of the VLBA-BU-BLAZAR Program". In: *The Astrophysical Journal Supplement Series* 260.1 (May 2022), p. 12. DOI: 10.3847/1538-4365/ac589c. URL: https://dx.doi.org/10.3847/1538-4365/ac589c.

[23] Svetlana Jorstad and Alan Marscher. "The VLBA-BU-BLAZAR Multi-Wavelength Monitoring Program". In: *Galaxies* 4.4, 47 (Oct. 2016), p. 47. DOI: 10.3390/galaxies4040047.

[24] Iván Agudo et al. "Mapcat: Monitoring AGN with Polarimetry at the Calar Alto Telescopes". In: *International Journal of Modern Physics Conference Series*. Vol. 8. International Journal of Modern Physics Conference Series. Jan. 2012, pp. 299–302. DOI: 10.1142/S2010194512004746. arXiv: 1111.6784 [astro-ph.HE].

[25] J. Otero-Santos et al. "Characterization of High-polarization Stars and Blazars with DIPOL-1 at Sierra Nevada Observatory". In: *AJ* 167.3, 137 (Mar. 2024), p. 137. DOI: 10.3847/1538-3881/ad250d. arXiv: 2312.05312 [astro-ph.IM].

[26] Juan Escudero Pedrosa et al. "IOP4, the Interactive Optical Photo-Polarimetric Python Pipeline". In: *AJ* 168.2, 84 (Aug. 2024), p. 84. DOI: 10.3847/1538-3881/ad5a80. arXiv: 2405.20111 [astro-ph.IM].

[27] Cherenkov Telescope Array Consortium et al. *Science with the Cherenkov Telescope Array*. 2019. DOI: 10.1142/10986.

[28] Juan Escudero Pedrosa et al. *First VHE gamma-ray observations of BL Lacertae with the Large-Sized Telescope (LST-1)*. Aug. 2022. DOI: 10.5281/zenodo.7037569. URL: https://doi.org/10.5281/zenodo.7037569.

[29] Robert Marcus Wagner. "Measurement of very high energy gamma-ray emission from four blazars using the MAGIC telescope and a comparative blazar study". PhD thesis. Max-Planck-Institute for Physics, Munich, Jan. 2006.

[30] Ruben Lopez-Coto. "Very-high-energy gamma-ray observations of pulsar wind nebulae and cataclysmic variable stars with MAGIC and development of trigger systems for IACTs". PhD thesis. Autonomous University of Barcelona, Spain, July 2015.

[31] *Zooniverse - Muon hunter classic*. 2017. URL: https://www.zooniverse.org/projects/zooniverse/muon-hunter-classic/about/research.

[32] R. Bird et al. "Muon Hunter: a Zooniverse project". In: *Journal of Physics Conference Series*. Vol. 1342. Journal of Physics Conference Series. IOP, Jan. 2020, 012103, p. 012103. DOI: 10.1088/1742-6596/1342/1/012103.

[33] R. D. Blandford and C. F. McKee. "Reverberation mapping of the emission line regions of Seyfert galaxies and quasars." In: *ApJ* 255 (Apr. 1982), pp. 419–439. DOI: 10.1086/159843.

[34] R. A. Edelson and J. H. Krolik. "The Discrete Correlation Function: A New Method for Analyzing Unevenly Sampled Variability Data". In: *ApJ* 333 (Oct. 1988), p. 646. DOI: 10.1086/166773.

[35] W. F. Welsh. "On the Reliability of Cross-Correlation Function Lag Determinations in Active Galactic Nuclei". In: *PASP* 111.765 (Nov. 1999), pp. 1347–1366. DOI: 10.1086/316457. arXiv: astro-ph/9911112.

[36] F. Tavecchio, G. Bonnoli, and G. Galanti. "On the distribution of fluxes of gamma-ray blazars: hints for a stochastic process?" In: *Mon. Not. Roy. Astron. Soc.* 497.1 (2020), pp. 1294–1300. DOI: 10.1093/mnras/staa2055. arXiv: 2004.09149 [astro-ph.HE].

[37] J. Escudero Pedrosa et al. "Repeating flaring activity of the blazar AO 0235+164". In: *A&A* 682, A100 (Feb. 2024), A100. DOI: 10.1051/0004-6361/202346885. arXiv: 2311.01157 [astro-ph.HE].

[38] Juan Escudero Pedrosa et al. "The flaring activity of blazar AO 0235+164 in 2021". In: *A&A* 689, A56 (Sept. 2024), A56. DOI: 10.1051/0004-6361/202449726. arXiv: 2405.10141 [astro-ph.HE].

[39] C. M. Raiteri et al. "The WEBT campaign to observe AO 0235+16 in the 2003-2004 observing season - Results from radio-to-optical monitoring and XMM-Newton observations". In: *A&A* 438.1 (2005), pp. 39–53. DOI: 10.1051/0004-6361:20042567. URL: https://doi.org/10.1051/0004-6361:20042567.

[40] J. Otero-Santos et al. "Multiwavelength periodicity search in a sample of γ-ray bright blazars". In: *MNRAS* 518.4 (Feb. 2023), pp. 5788–5807. DOI: 10.1093/mnras/stac3142. arXiv: 2210.16327 [astro-ph.HE].

[41] Zulema Abraham. "Jet precession in binary black holes". In: *Nature Astronomy* 2 (May 2018), pp. 443–444. DOI: 10.1038/s41550-018-0484-2.

[42] J. Otero-Santos et al. "Optical follow-up of the gamma-ray flare of the blazar OP 313 reveals a bright state with high polarization degree". In: *The Astronomer's Telegram* 16360 (Dec. 2023), p. 1.

[43] J. Otero-Santos et al. "Optical outburst of the blazar 3C 345 with an exceptionally high polarization degree". In: *The Astronomer's Telegram* 16305 (Oct. 2023), p. 1.

[44] A. L. Peirson and Roger W. Romani. "The Polarization Behavior of Relativistic Synchrotron Self-Compton Jets". In: *ApJ* 885.1, 76 (Nov. 2019), p. 76. DOI: 10.3847/1538-4357/ab46b1. arXiv: 1909.10563 [astro-ph.HE].

[45] Ioannis Liodakis et al. "Polarized blazar X-rays imply particle acceleration in shocks". In: *Nature* 611.7937 (Nov. 2022), pp. 677–681. DOI: 10.1038/s41586-022-05338-0. arXiv: 2209.06227 [astro-ph.HE].

[46] K. I. Kellermann. "The discovery of quasars and its aftermath". In: *Journal of Astronomical History and Heritage* 17.3 (Nov. 2014), pp. 267–282.

[47] I.S. Shklovsky. In: *Proc. Acad. Sci. URSS* 91 (1953), p. 475.

[48] H. Alfvén and N. Herlofson. "Phys. Rev." In: 78 (1950), p. 616.

[49] F. Aharonian et al. "A low level of extragalactic background light as revealed by γ-rays from blazars". In: *Nature* 440.7087 (Apr. 2006), pp. 1018–1021. DOI: 10.1038/nature04680. arXiv: astro-ph/0508073 [astro-ph].

[50] P. D. Welch. "The Use of Fast Fourier Transform for the Estimation of Power Spectra: A Method Based on Time Averaging Over Short, Modified Periodograms". In: *IEEE Trans. Audio & Electroacoust* 15 (Jan. 1967), pp. 70–73.

[51] Piirola, V. et al. "High-precision polarimetry of nearby stars (d < 50 pc) - Mapping the interstellar dust and magnetic field inside the Local Bubble". In: *A&A* 635 (2020), A46. DOI: 10.1051/0004-6361/201937324. URL: https://doi.org/10.1051/0004-6361/201937324.

[52] Ivan Agudo et al. "On the Location of the Gamma-ray Emission in the 2008 Outburst in the BL Lacertae Object AO 0235+164 through Observations across the Electromagnetic Spectrum". In: *Astrophys. J. Lett.* 735 (2011), p. L10. DOI: 10.1088/2041-8205/735/1/L10. arXiv: 1105.0549 [astro-ph.HE].

[53] M. Ackermann et al. "Multi-wavelength observations of blazar AO 0235+164 in the 2008-2009 flaring state". In: *Astrophys. J.* 751 (2012), p. 159. DOI: 10.1088/0004-637X/751/2/159. arXiv: 1207.2932 [astro-ph.HE].

[54] Alan P. Marscher. "Turbulent, Extreme Multi-Zone Model for Simulating Flux and Polarization Variability in Blazars". In: *Astrophys. J.* 780 (2014), p. 87. DOI: 10.1088/0004-637X/780/1/87. arXiv: 1311.7665 [astro-ph.HE].

[55] Svetlana G. Jorstad et al. "Multiepoch Very Long Baseline Array Observations of EGRET-detected Quasars and BL Lacertae Objects: Superluminal Motion of Gamma-Ray Bright Blazars". In: *The Astrophysical Journal Supplement Series* 134.2 (June 2001), pp. 181–240. DOI: 10.1086/320858. URL: https://doi.org/10.1086/320858.

[56] C. M. Raiteri et al. "Radio-to-UV monitoring of AO 0235+164 by the WEBT and Swift during the 2006-2007 outburst". In: *Astronomy and Astrophysics* 480.2 (Mar. 2008), pp. 339–347. DOI: 10.1051/0004-6361:20079044. arXiv: 0801.1236 [astro-ph].

[57] V. T. Junkkarinen et al. "Dust and Diffuse Interstellar Bands in the z_a = 0.524 Absorption System toward AO 0235+164". In: *ApJ* 614.2 (Oct. 2004), pp. 658–670. DOI: 10.1086/423777. arXiv: astro-ph/0407281 [astro-ph].

[58] Yi-Fan Wang and Yun-Guo Jiang. "A Comprehensive Study on the Variation Phenomena of AO 0235+164". In: *ApJ* 902.1, 41 (Oct. 2020), p. 41. DOI: 10.3847/1538-4357/abb36c. arXiv: 2009.00879 [astro-ph.HE].

[59] A. M. Kutkin et al. "The extreme blazar AO 0235+164 as seen by extensive ground and space radio observations". In: *MNRAS* 475.4 (Apr. 2018), pp. 4994–5009. DOI: 10.1093/mnras/sty144. arXiv: 1801.04892 [astro-ph.GA].

[60] Kouichi Hirotani. "Kinetic Luminosity and Composition of Active Galactic Nuclei Jets". In: *The Astrophysical Journal* 619.1 (Jan. 2005), pp. 73–85. DOI: 10.1086/426497. URL: https://doi.org/10.1086/426497.

[61] A. E. Volvach et al. "Flare Activity of Blazar AO 0235+164". In: *Cosmic Research* 57.2 (Mar. 2019), pp. 85–90. DOI: 10.1134/S0010952519020096.

[62] Cosimo Nigro et al. *agnpy*. Version 0.1.8. Jan. 2022. DOI: 10.5281/zenodo.5932850. URL: https://doi.org/10.5281/zenodo.5932850.

[63] C. Deil et al. "Gammapy - A prototype for the CTA science tools". In: *35th International Cosmic Ray Conference (ICRC2017)*. Vol. 301. International Cosmic Ray Conference. Jan. 2017, 766, p. 766. arXiv: 1709.01751 [astro-ph.IM].

[64] Iván Agudo et al. "Erratic Jet Wobbling in the BL Lacertae Object OJ287 Revealed by Sixteen Years of 7 mm VLBA Observations". In: *ApJ* 747.1, 63 (Mar. 2012), p. 63. DOI: 10.1088/0004-637X/747/1/63. arXiv: 1112.4747 [astro-ph.CO].

[65] Carolina Casadio et al. "A Multi-Wavelength Polarimetric Study of the Blazar CTA 102 During a Gamma-Ray Flare in 2012". In: *The Astrophysical Journal* 813.1 (Oct. 2015), p. 51. DOI: 10.1088/0004-637x/813/1/51. URL: https://doi.org/10.1088/0004-637x/813/1/51.

[66] Iván Agudo et al. "Jet Stability and the Generation of Superluminal and Stationary Components". In: *ApJ* 549.2 (Mar. 2001), pp. L183–L186. DOI: 10.1086/319158. arXiv: astro-ph/0101188 [astro-ph].

[67] A. Celotti, G. Ghisellini, and A. C. Fabian. "Bulk Comptonization spectra in blazars". In: *Monthly Notices of the Royal Astronomical Society* 375.2 (Jan. 2007), pp. 417–424. ISSN: 0035-8711. DOI: 10.1111/j.1365-2966.2006.11289.x. eprint: https://academic.oup.com/mnras/article-pdf/375/2/417/4242744/mnras0375-0417.pdf. URL: https://doi.org/10.1111/j.1365-2966.2006.11289.x.

[68] Jeffrey D. Scargle et al. "Studies in Astronomical Time Series Analysis. VI. Bayesian Block Representations". In: *ApJ* 764.2, 167 (Feb. 2013), p. 167. DOI: 10.1088/0004-637X/764/2/167. arXiv: 1207.5578 [astro-ph.IM].

[69] Lenté Dreyer and Markus Böttcher. "Monte Carlo Applications for Partially Polarized Inverse External-Compton Scattering (MAPPIES). II. Application to the UV/Soft X-Ray Excess in Blazar Spectra". In: *The Astrophysical Journal* 910.1 (Mar. 2021), p. 2. DOI: 10.3847/1538-4357/abe133. URL: https://dx.doi.org/10.3847/1538-4357/abe133.

[70] M. Böttcher and C. D. Dermer. "Timing Signatures of the Internal-Shock Model for Blazars". In: *The Astrophysical Journal* 711.1 (Feb. 2010), p. 445. DOI: 10.1088/0004-637X/711/1/445. URL: https://dx.doi.org/10.1088/0004-637X/711/1/445.

[71] Andrei Sokolov, Alan P. Marscher, and Ian M. McHardy. "Synchrotron Self-Compton Model for Rapid Nonthermal Flares in Blazars with Frequency-dependent Time Lags". In: *The Astrophysical Journal* 613.2 (Oct. 2004), p. 725. DOI: 10.1086/423165. URL: https://dx.doi.org/10.1086/423165.

[72] Alan P. Marscher et al. "Probing the Inner Jet of the Quasar PKS 1510-089 with Multi-Waveband Monitoring During Strong Gamma-Ray Activity". In: *ApJ* 710.2 (Feb. 2010), pp. L126–L131. DOI: 10.1088/2041-8205/710/2/L126. arXiv: 1001.2574 [astro-ph.CO].

[73] Matthew G. Baring, Markus Böttcher, and Errol J. Summerlin. "Probing acceleration and turbulence at relativistic shocks in blazar jets". In: *MNRAS* 464.4 (Feb. 2017), pp. 4875–4894. DOI: 10.1093/mnras/stw2344. arXiv: 1609.03899 [astro-ph.HE].

[74] Planck Collaboration et al. "Planck 2018 results. VI. Cosmological parameters". In: *A&A* 641, A6 (Sept. 2020), A6. DOI: 10.1051/0004-6361/201833910. arXiv: 1807.06209 [astro-ph.CO].

[75] Andrea Tramacere. *JetSeT: Numerical modeling and SED fitting tool for relativistic jets*. Astrophysics Source Code Library, record ascl:2009.001. Sept. 2020. ascl: 2009.001.

[76] A. Tramacere, E. Massaro, and A. M. Taylor. "Stochastic Acceleration and the Evolution of Spectral Distributions in Synchro-Self-Compton Sources: A Self-consistent Modeling of Blazars' Flares". In: *ApJ* 739.2, 66 (Oct. 2011), p. 66. DOI: 10.1088/0004-637X/739/2/66. arXiv: 1107.1879 [astro-ph.HE].

[77] A. Tramacere et al. "Swift observations of the very intense flaring activity of Mrk 421 during 2006. I. Phenomenological picture of electron acceleration and predictions for MeV/GeV emission". In: *A&A* 501.3 (July 2009), pp. 879–898. DOI: 10.1051/0004-6361/200810865. arXiv: 0901.4124 [astro-ph.HE].

[78] E. Massaro et al. "Log-parabolic spectra and particle acceleration in blazars. III. SSC emission in the TeV band from Mkn501". In: *A&A* 448.3 (Mar. 2006), pp. 861–871. DOI: 10.1051/0004-6361:20053644. arXiv: astro-ph/0511673 [astro-ph].

[79] Hans Dembinski and Piti Ongmongkolkul et al. "scikit-hep/iminuit". In: (Dec. 2020). DOI: 10.5281/zenodo.3949207. URL: https://doi.org/10.5281/zenodo.3949207.

[80] Dmitry Blinov and Vasiliki Pavlidou. "The RoboPol Program: Optical Polarimetric Monitoring of Blazars". In: *Galaxies* 7.2 (2019). ISSN: 2075-4434. DOI: 10.3390/galaxies7020046. URL: https://www.mdpi.com/2075-4434/7/2/46.

[81] Juhan Frank, Andrew King, and Derek J. Raine. *Accretion Power in Astrophysics: Third Edition*. Cambridge University Press, 2002.

[82] K. Cleary et al. "Spitzer Observations of 3C Quasars and Radio Galaxies: Mid-Infrared Properties of Powerful Radio Sources". In: *ApJ* 660.1 (May 2007), pp. 117–145. DOI: 10.1086/511969. arXiv: astro-ph/0612702 [astro-ph].

[83] Shai Kaspi et al. "Reverberation Mapping of High-Luminosity Quasars: First Results". In: *ApJ* 659.2 (Apr. 2007), pp. 997–1007. DOI: 10.1086/512094. arXiv: astro-ph/0612722 [astro-ph].

[84] Greg Madejski et al. "Simultaneous Soft X-Ray and GeV Gamma-Ray Observations of BL Lacertae Object AO 0235+164". In: *ApJ* 459 (Mar. 1996), p. 156. DOI: 10.1086/176877.

[85] Alan P. Marscher et al. "The inner jet of an active galactic nucleus as revealed by a radio-to-γ-ray outburst". In: *Nature* 452.7190 (Apr. 2008), pp. 966–969. DOI: 10.1038/nature06895.

[86] Svetlana G. Jorstad et al. "Polarimetric Observations of 15 Active Galactic Nuclei at High Frequencies: Jet Kinematics from Bimonthly Monitoring with the Very Long Baseline Array". In: *AJ* 130.4 (Oct. 2005), pp. 1418–1465. DOI: 10.1086/444593. arXiv: astro-ph/0502501 [astro-ph].

[87] Roger Blandford, David Meier, and Anthony Readhead. "Relativistic Jets from Active Galactic Nuclei". In: *Ann. Rev. Astron. Astrophys.* 57 (2019), pp. 467–509. DOI: 10.1146/annurev-astro-081817-051948. arXiv: 1812.06025 [astro-ph.HE].

[88] K. A. Arnaud. "XSPEC: The First Ten Years". In: *Astronomical Data Analysis Software and Systems V*. Ed. by George H. Jacoby and Jeannette Barnes. Vol. 101. Astronomical Society of the Pacific Conference Series. Jan. 1996, p. 17.

[89] Scott D. Barthelmy et al. "The Burst Alert Telescope (BAT) on the SWIFT Midex Mission". In: *Space Sci. Rev.* 120.3-4 (Oct. 2005), pp. 143–164. DOI: 10.1007/s11214-005-5096-3. arXiv: astro-ph/0507410 [astro-ph].

[90] A. A. Breeveld et al. "Further calibration of the Swift ultraviolet/optical telescope". In: *MNRAS* 406.3 (Aug. 2010), pp. 1687–1700. DOI: 10.1111/j.1365-2966.2010.16832.x. arXiv: 1004.2448 [astro-ph.IM].

[91] David N. Burrows et al. "The Swift X-Ray Telescope". In: *Space Sci. Rev.* 120.3-4 (Oct. 2005), pp. 165–195. DOI: 10.1007/s11214-005-5097-2. arXiv: astro-ph/0508071 [astro-ph].

[92] P. A. Evans et al. "Methods and results of an automatic analysis of a complete sample of Swift-XRT observations of GRBs". In: *MNRAS* 397.3 (Aug. 2009), pp. 1177–1201. DOI: 10.1111/j.1365-2966.2009.14913.x. arXiv: 0812.3662 [astro-ph].

[93] N. Gehrels et al. "The Swift Gamma-Ray Burst Mission". In: *ApJ* 611.2 (Aug. 2004), pp. 1005–1020. DOI: 10.1086/422091. arXiv: astro-ph/0405233 [astro-ph].

[94] Joanne E. Hill et al. "Readout modes and automated operation of the Swift X-ray Telescope". In: *X-Ray and Gamma-Ray Instrumentation for Astronomy XIII*. Ed. by Kathryn A. Flanagan and Oswald H. W. Siegmund. Vol. 5165. Society of Photo-Optical Instrumentation Engineers (SPIE) Conference Series. Feb. 2004, pp. 217–231. DOI: 10.1117/12.505728.

[95] Alberto Moretti et al. "In-flight calibration of the Swift XRT Point Spread Function". In: *UV, X-Ray, and Gamma-Ray Space Instrumentation for Astronomy XIV*. Ed. by Oswald H. W. Siegmund. Vol. 5898. Society of Photo-Optical Instrumentation Engineers (SPIE) Conference Series. Aug. 2005, pp. 360–368. DOI: 10.1117/12.617164.

[96] T. S. Poole et al. "Photometric calibration of the Swift ultraviolet/optical telescope". In: *MNRAS* 383.2 (Jan. 2008), pp. 627–645. DOI: 10.1111/j.1365-2966.2007.12563.x. arXiv: 0708.2259 [astro-ph].

[97] Peter W. A. Roming et al. "The Swift Ultra-Violet/Optical Telescope". In: *Space Sci. Rev.* 120.3-4 (Oct. 2005), pp. 95–142. DOI: 10.1007/s11214-005-5095-4. arXiv: astro-ph/0507413 [astro-ph].

[98] Ross D. Cohen et al. "The Nature of the BL Lacertae Object AO 0235+164". In: *ApJ* 318 (July 1987), p. 577. DOI: 10.1086/165393.

[99] A. A. Abdo et al. "Gamma-ray Light Curves and Variability of Bright Fermi-detected Blazars". In: *ApJ* 722.1 (Oct. 2010), pp. 520–542. DOI: 10.1088/0004-637X/722/1/520. arXiv: 1004.0348 [astro-ph.HE].

[100] A. Tramacere et al. "Radio-γ-ray response in blazars as a signature of adiabatic blob expansion". In: *A&A* 658, A173 (Feb. 2022), A173. DOI: 10.1051/0004-6361/202142003. arXiv: 2112.03941 [astro-ph.HE].

[101] N. R. Lomb. "Least-Squares Frequency Analysis of Unequally Spaced Data". In: *Ap&SS* 39.2 (Feb. 1976), pp. 447–462. DOI: 10.1007/BF00648343.

[102] J. D. Scargle. "Studies in astronomical time series analysis. II. Statistical aspects of spectral analysis of unevenly spaced data." In: *ApJ* 263 (Dec. 1982), pp. 835–853. DOI: 10.1086/160554.

[103] Jacob T. VanderPlas. "Understanding the Lomb-Scargle Periodogram". In: *ApJS* 236.1, 16 (May 2018), p. 16. DOI: 10.3847/1538-4365/aab766. arXiv: 1703.09824 [astro-ph.IM].

[104] L. Ostorero, M. Villata, and C. M. Raiteri. "Helical jets in blazars. Interpretation of the multifrequency long-term variability of AO 0235+16". In: *A&A* 419 (June 2004), pp. 913–925. DOI: 10.1051/0004-6361:20035813. arXiv: astro-ph/0402551 [astro-ph].

[105] J. L. Gómez et al. "Hydrodynamical Models of Superluminal Sources". In: *The Astrophysical Journal* 482.1 (June 1997), p. L33. DOI: 10.1086/310671. URL: https://dx.doi.org/10.1086/310671.

[106] Paul T. P. Ho, James M. Moran, and Kwok Yung Lo. "The Submillimeter Array". In: *ApJ* 616.1 (Nov. 2004), pp. L1–L6. DOI: 10.1086/423245. arXiv: astro-ph/0406352 [astro-ph].

[107] Rurik A. Primiani et al. "SWARM: A 32 GHz Correlator and VLBI Beamformer for the Submillimeter Array". In: *Journal of Astronomical Instrumentation* 5.4, 1641006-810 (Dec. 2016), pp. 1641006–810. DOI: 10.1142/S2251171716410063. arXiv: 1611.02596 [astro-ph.IM].

[108] R. A. Shaw, H. E. Payne, and J. J. E. Hayes, eds. *Astronomical Data Analysis Software and Systems IV*. Vol. 77. Astronomical Society of the Pacific Conference Series. San Francisco: Astronomical Society of the Pacific, Oct. 1995, p. 433.

[109] Juan Escudero Pedrosa, Daniel Morcuende Parrilla, and Jorge Otero-Santos. *IOP4*. Version v1.2.0. June 2024. DOI: 10.5281/zenodo.11548299. URL: https://doi.org/10.5281/zenodo.11548299.

[110] M. R. Zapatero Osorio, J. A. Caballero, and V. J. S. Béjar. "Optical Linear Polarization of Late M and L Type Dwarfs". In: *ApJ* 621.1 (Mar. 2005), pp. 445–460. DOI: 10.1086/427433. arXiv: astro-ph/0411531 [astro-ph].

[111] Ferdinando Patat and Martino Romaniello. "Error Analysis for Dual-Beam Optical Linear Polarimetry". In: *PASP* 118.839 (Jan. 2006), pp. 146–161. DOI: 10.1086/497581. arXiv: astro-ph/0509153 [astro-ph].

[112] Matt Craig et al. *CCD Data Reduction Guide*. 2022. URL: https://www.astropy.org/ccd-reduction-and-photometry-guide/.

[113] K. Nilsson et al. "Host galaxy subtraction of TeV candidate BL Lacertae objects". In: *A&A* 475.1 (Nov. 2007), pp. 199–207. DOI: 10.1051/0004-6361:20077624. arXiv: 0709.2533 [astro-ph].

[114] Larry Bradley et al. *astropy/photutils: 1.8.0*. Version 1.8.0. May 2023. DOI: 10.5281/zenodo.7946442. URL: https://doi.org/10.5281/zenodo.7946442.

[115] Dustin Lang et al. "Astrometry.net: Blind Astrometric Calibration of Arbitrary Astronomical Images". In: *AJ* 139.5 (May 2010), pp. 1782–1800. DOI: 10.1088/0004-6256/139/5/1782. arXiv: 0910.2233 [astro-ph.IM].

[116] W. D. Pence et al. "Definition of the Flexible Image Transport System (FITS), version 3.0". In: *A&A* 524, A42 (Dec. 2010), A42. DOI: 10.1051/0004-6361/201015362.

[117] E. W. Greisen and M. R. Calabretta. "Representations of world coordinates in FITS". In: *A&A* 395 (Dec. 2002), pp. 1061–1075. DOI: 10.1051/0004-6361:20021326. arXiv: astro-ph/0207407 [astro-ph].

[118] Astropy Collaboration et al. "Astropy: A community Python package for astronomy". In: *A&A* 558, A33 (Oct. 2013), A33. DOI: 10.1051/0004-6361/201322068. arXiv: 1307.6212 [astro-ph.IM].

[119] Astropy Collaboration et al. "The Astropy Project: Building an Open-science Project and Status of the v2.0 Core Package". In: *AJ* 156.3, 123 (Sept. 2018), p. 123. DOI: 10.3847/1538-3881/aabc4f. arXiv: 1801.02634 [astro-ph.IM].

[120] Astropy Collaboration et al. "The Astropy Project: Sustaining and Growing a Community-oriented Open-source Project and the Latest Major Release (v5.0) of the Core Package". In: *ApJ* 935.2, 167 (Aug. 2022), p. 167. DOI: 10.3847/1538-4357/ac7c74. arXiv: 2206.14220 [astro-ph.IM].

[121] Bokeh Development Team. *Bokeh: Python library for interactive visualization*. 2023. URL: https://bokeh.org/.

[122] Charles R. Harris et al. "Array programming with NumPy". In: *Nature* 585.7825 (Sept. 2020), pp. 357–362. DOI: 10.1038/s41586-020-2649-2. URL: https://doi.org/10.1038/s41586-020-2649-2.

[123] Django Software Foundation. *Django*. Version 4.2. 2023. URL: https://www.djangoproject.com.

[124] SQLite Developers. *SQLite*. Version 3. 2023. URL: https://www.sqlite.org/.

[125] Vue Developers. *Vue*. Version 3.4.9. 2023. URL: https://vuejs.org/.

[126] Sebastian Jester et al. "The Sloan Digital Sky Survey View of the Palomar-Green Bright Quasar Survey". In: *AJ* 130.3 (Sept. 2005), pp. 873–895. DOI: 10.1086/432466. arXiv: astro-ph/0506022 [astro-ph].

[127] Robert Lupton. *Transformations between SDSS magnitudes and other systems - SDSS-III*. 2005. URL: https://www.sdss3.org/dr8/algorithms/sdssUBVRITransform.php#Lupton2005 (visited on 04/07/2024).

[128] K. Jordi, E. K. Grebel, and K. Ammon. "Empirical color transformations between SDSS photometry and other photometric systems". In: *A&A* 460.1 (Dec. 2006), pp. 339–347. DOI: 10.1051/0004-6361:20066082. arXiv: astro-ph/0609121 [astro-ph].

[129] C. Husillos et al. *cesarhusrod/iop3: v1.0.0*. Version v1.0.0. 2021. DOI: 10.5281/zenodo.10995575. URL: https://doi.org/10.5281/zenodo.10995575.

[130] Dawoon E. Kim et al. "Magnetic field properties inside the jet of Mrk 421. Multiwavelength polarimetry, including the Imaging X-ray Polarimetry Explorer". In: *A&A* 681, A12 (Jan. 2024), A12. DOI: 10.1051/0004-6361/202347408. arXiv: 2310.06097 [astro-ph.HE].

[131] Steven R. Ehlert et al. "X-Ray Polarization of the BL Lacertae Type Blazar 1ES 0229+200". In: *ApJ* 959.1, 61 (Dec. 2023), p. 61. DOI: 10.3847/1538-4357/ad05c4. arXiv: 2310.01635 [astro-ph.HE].

[132] Herman L. Marshall et al. "Observations of Low and Intermediate Spectral Peak Blazars with the Imaging X-ray Polarimetry Explorer". In: *arXiv e-prints*, arXiv:2310.11510 (Oct. 2023), arXiv:2310.11510. DOI: 10.48550/arXiv.2310.11510. arXiv: 2310.11510 [astro-ph.HE].

[133] Laura Di Gesu et al. "Discovery of X-ray polarization angle rotation in the jet from blazar Mrk 421." In: *Nature Astronomy* 7 (Oct. 2023), pp. 1245–1258. DOI: 10.1038/s41550-023-02032-7. arXiv: 2305.13497 [astro-ph.HE].

[134] Riccardo Middei et al. "IXPE and Multiwavelength Observations of Blazar PG 1553+113 Reveal an Orphan Optical Polarization Swing". In: *ApJ* 953.2, L28 (Aug. 2023), p. L28. DOI: 10.3847/2041-8213/acec3e. arXiv: 2308.00039 [astro-ph.HE].

[135] Abel L. Peirson et al. "X-Ray Polarization of BL Lacertae in Outburst". In: *ApJ* 948.2, L25 (May 2023), p. L25. DOI: 10.3847/2041-8213/acd242. arXiv: 2305.13898 [astro-ph.HE].

[136] Riccardo Middei et al. "X-Ray Polarization Observations of BL Lacertae". In: *ApJ* 942.1, L10 (Jan. 2023), p. L10. DOI: 10.3847/2041-8213/aca281. arXiv: 2211.13764 [astro-ph.HE].

[137] Ioannis Liodakis et al. "Polarized blazar X-rays imply particle acceleration in shocks". In: *Nature* 611.7937 (Nov. 2022), pp. 677–681. DOI: 10.1038/s41586-022-05338-0. arXiv: 2209.06227 [astro-ph.HE].

[138] Manel Errando et al. "Detection of X-Ray Polarization from the Blazar 1ES 1959+650 with the Imaging X-Ray Polarimetry Explorer". In: *ApJ* 963.1, 5 (Mar. 2024), p. 5. DOI: 10.3847/1538-4357/ad1ce4. arXiv: 2401.04420 [astro-ph.HE].

[139] Laura Di Gesu et al. "The X-Ray Polarization View of Mrk 421 in an Average Flux State as Observed by the Imaging X-Ray Polarimetry Explorer". In: *ApJ* 938.1, L7 (Oct. 2022), p. L7. DOI: 10.3847/2041-8213/ac913a. arXiv: 2209.07184 [astro-ph.HE].

IAA INSTITUTO DE ASTROFÍSICA DE ANDALUCÍA

EXCELENCIA SEVERO OCHOA

CSIC

UNIVERSIDAD DE GRANADA

Image credit: Jet emerging from the core of M87, NASA and the Hubble Heritage Team (STScI/AURA)